UNIVERSIDAD DE CONCEPCIÓN
FACULTAD DE CIENCIAS FÍSICAS Y MATEMÁTICAS

ELECTRODINÁMICA CUÁNTICA DE CAVIDADES INFRAROJAS CON OSCILADORES ANARMÓNICOS EN NANOFOTÓNICA

Infrared cavity quantum electrodynamics with anharmonic oscillators in nanophotonics

Por: Mauricio Andrés Arias Contreras

Tesis presentada a la Facultad de Ciencias Físicas y Matemáticas de la Universidad de Concepción para optar al grado académico de Doctor en Ciencias Físicas

November 30, 2023
Concepción, Chile

Supervisor: Prof. Aldo Delgado Hidalgo
Co-Supervisor: Prof. Felipe Herrera

Acknowledgements

This document that you are now reading is the vestige of a work that has taken years, not only in the productive field, but also in training, and in areas that transcend the scientific, not only in the academic sense but mainly in my integral human development. This entire process would not have been possible without the people who have been in one way or another providing me with their support and encouraging me, both in my triumphs and in confronting my several shortcomings.

I would like to start by giving thanks to all my family, and in particular to my beloved parents, Juana and Luis, and my brother Ronald and his family, who have shown me about the power of love and resilience, even in the darkest moments of life. Nothing makes sense without the love that lives in me, thanks to you.

I also want to acknowledge the fundamental role of my thesis guides, Professor Aldo Delgado and Professor Felipe Herrera, who trusted and encouraged me, mainly in my moments of greatest weakness. You saw something I never knew how to see in myself. I hope to one day give back, even a little, and live up to that trust. The best thing I can do is give back to those who are just beginning the path that I am now completing.

I was lucky to meet many people, but I never expected the love and friendship that I have received in all this time, both from the members of the “Legion” group led by Aldo in Concepción and in the group “Herrera Lab” in Santiago de Chile. Thank you to all of you, those who have already left and those who are still close. They don’t know how fundamental it was to have met them.

To all my friends, to those who welcomed me into their home and gave me the little they had, to the “Peru–Bolivia team" who infected me with their passion and funny sense of humor, even to those who were more or less explicit in their displeasure with me, thank you, and sorry for my outbursts and inconsiderations.

I am someone better and less bitter, I have learned from all of you, you all have a piece of my heart.

Finally, I want to acknowledge to the financial support of ANID through the scholarship program Doctorado Becas Chile/2018—21181591 and also the financial

and sponsorship from MIRO and the people from the department of physics of Universidad de Santiago.

Abstract

The characterization and manipulation of complex microscopic systems for applications in science and technology demands to have robust theoretical tools that guide the extraction of relevant information or complement such processes. In particular, condensed phase physics, which is in a blurry boundary between chemistry and quantum physics, requires several approximations due the high number of degrees of freedom present. Thereupon, achieving a satisfactory balance between a model with just the right amount of features and, hopefully, requiring low computational requirements represents a significant challenge. This is the reason why having minimal models to understand the fundamental physics of complex condensed phases, in organic or inorganic materials, particularly when subject to confined electromagnetic fields, is a valuable contribution, specially appreciated in chemical physics and quantum optics protocols.

In this thesis we show an intensive exploration of the capabilities of a nonlinear mid-infrared semi empirical model for describing the coherent and incoherent dynamics of anharmonic dipoles coupled to a single harmonic mode of a cavity QED. We find that the intrinsic anharmonicity in the material spectrum is heralded to the near electric field of a nanoresonator. Depending on the classical driving intensity ratio with respect to losses, this mechanism allows for the control and modulation of the complex phase of an incident finite pulse to the resonator with respect to the scattered cavity field, which translates into a delay in the stationary temporal domain, even after the pump pulse has ended.

This mechanism promises interesting applications in molecular infrared nanophotonics, where the intrinsic anharmonicities of the vibrational modes are well documented in the literature, and also because the light-matter system requires to be in weak coupling regime, increasing the prospects for its experimental realization using current nanophotonic technology.

Moreover, we show that our approach is applicable to other non organic devices as intersubbands in multi-quantum wells (MQW's), where the *state–of–the–art* in both material and optical parameters engineering, as well as the capability of having smaller N compared to molecular systems, promises stronger effects on the nonlinear phase modulation, which can be modified and even increased by adapted heterogeneities among the dipoles that introduce contributions from

the dark manifold. We expect our model will help in the development of new infrared nanophotonic hardware for applications ranging from quantum control of materials to quantum information processing.

Resumen

La caracterización y manipulación de sistemas microscópicos complejos para aplicaciones en ciencia y tecnología exige contar con herramientas teóricas robustas que orienten la extracción de información relevante sobre ellos, o bien que complementen dicho proceso. En particular, la física de materia condensada, que se encuentra en una frontera borrosa entre la química y la física cuántica, requiere varias aproximaciones debido al alto número de grados de libertad presentes. Luego, el tener un equilibrio satisfactorio entre un modelo con la justa cantidad de características, y, con suerte, precisando bajos requisitos computacionales, en un gran desafío. Ésta es la razón por la que contar con modelos minimales para comprender la física fundamental de fases condensadas complejas, en materiales orgánicos o inorgánicos, particularmente cuando están sujetos a campos electromagnéticos confinados, es una contribución valiosa, especialmente apreciada en protocolos de física química y óptica cuántica.

En esta tesis mostramos una exploración intensiva de las capacidades de un modelo semiempírico en el infrarrojo medio y no lineal para describir la dinámica coherente e incoherente de dipolos anarmónicos acoplados a un modo único armónico de cavidad QED. Encontramos que la anarmonicidad intrínseca en el espectro material se traspasada al campo eléctrico cercano de un nanoresonador. Dependiendo de la relación de intensidad de bombeo clásico con respecto a las pérdidas, este mecanismo permite el control y la modulación de la fase compleja de un pulso finito incidente al resonador con respecto al campo dispersado, que se traduce en un retraso en el dominio temporal estacionario, incluso después que el pulso de bombeo ha terminado.

Este mecanismo promete interesantes aplicaciones en nanofotónica infrarroja molecular, donde las anarmonicidades intrínsecas de los modos vibratorios están bien documentadas en la literatura, y también porque el sistema luz–materia necesita estar en el régimen de acoplamiento débil, lo que aumenta las perspectivas de su realización experimental utilizando tecnologías de nanofotónica actual.

Además, mostramos que nuestro enfoque es aplicable a otros dispositivos no orgánicos como intersubbandas en multi–pozos cuánticos (MQW), donde el *estado del arte* en ingeniería de parámetros ópticos y de materiales, como así como la capacidad de tener N más pequeños en comparación con sistemas moleculares,

promete efectos más fuertes en la modulación de fase no lineal, que pueden ser modificados e incluso aumentados por inhomogeneidad adaptadas entre los dipolos que introducen contribuciones de la variedad oscura. Esperamos que nuestro modelo ayude en el desarrollo de nuevo hardware nanofotónico infrarrojo para aplicaciones que van desde el control cuántico de materiales al procesamiento de información cuántica.

Contents

List of Tables

List of Figures

Chapter 1

Introduction

The property of linear superposition of the Electromagnetic (EM) field *in vacuum* is a fundamental principle, stated in both Classical and Quantum Electrodynamics (QED). This implies that 1) photons, the quanta of light, do not interact to each other and 2) polarizable matter is the fundamental source of Nonlinear Optical phenomena [12]. Basically, it is a consequence of the anharmonic motion of charge carriers induced by sufficiently intense optical fields when they are transmitted trough the media [6].

About this last requirement, the birth of laser technology marked a milestone as it leveraged the exploration of novel optical and material phenomena. In particular, its application as a source of coherence in nanophotonics allowed us to observe the exotic ways matter behaves when it is dressed with just one photon or the electromagnetic vacuum [73, 27]. This regime is highly desired as the control of the fast coherence times in which light-matter interactions occur is the basis of modern Quantum Computing technologies [54].
The development of the field owes a significant amount to the use of semiconductor materials, not only for the emergence of semiconductor lasers but also by the sophisticated state of the art in growth and doping techniques and their tunability and integrability in miniaturized optoelectronic circuits. Good examples are engineered dipoles like quantum dots [5] and quantum wells [19] that present themselves as semiconductor-based heterostructures with the ability to simulate complex quantum systems while preserving their fundamental features in a simplified fashion.

In this context, the inquiry into how the degree of anharmonicity within the spectrum of a material system impacts its optical response arises naturally. For atoms modeled using the two-level approximation within a resonator, nonlinearity is intricately linked to the anharmonicity of the coupled spectrum. This anharmonicity becomes more intricate as the strength of the light-matter interaction intensifies, directly correlating with regimes of strong or ultrastrong coupling [39]. Conversely, in this Thesis we show that for molecular vibrations within infrared cavities, anharmonicity constitutes an inherent characteristic that can be coherently transferred, even within a weak coupling regime. This transfer facilitates the modulation of the nonlinear phase within a transmitted wave signal, an effect that scalates with the square of the effective photon flux rate but diminishes inversely with the number of molecules. This inverse relationship poses a challenge in realizing the higher shifts predicted by the model, primarily due to the complexity of confining only a small number of molecules within modern cavity QED.

This thesis presents a theoretical prediction that connects the anharmonicity of intramolecular vibrations in molecules and also with the intersubbands of a multiquantum well (MQW) embedded in a mid-infrared nanoantenna, with intensity-dependent phase rotations due to incoming femtosecond pulses that weakly excite the near field of the resonator from the coupled vacuum. In particular, we use MQW empirical parameters because they allow the experimental observation of higher nonlinearities due to the small number of coupled oscillators. Specifically, we predict that the shifts are enhanced when non-identical anharmonic dipoles are used due to the coherent and incoherent interaction with the dark manifold in the dipole approximation. To estimate the phase shift values that can be achieved in near-future experimental implementations, we use a mean-field approach to gain phenomenological insight. Our methodology can be applied to other types of systems and expanded to include additional quantum wells and multiple laser fields.

Chapter 2

Cavity Electrodynamics

2.1 Motivation

The process of quantization of the EM field relies in its decomposition into normal modes, by Fourier analysis, promoting the canonical coordinates and momenta associated with each oscillator to operators acting in a Hilbert space. In order to make this decomposition, it is necessary to study how the electromagnetic waves are constrained by the geometric properties of the propagation media, and in particular, to its boundaries with respect to "free space" [36]. The purpose of this chapter is to show *how can we emerge a single quantized electromagnetic mode of oscillation inside an idealized optical resonator*. This theoretical example is a simplification in the sense that realistic cavities generally manifests a multi-mode spectrum. However, the idea of single out just one of them makes sense from the superposition principle; the analysis of one is physically representative of the general frequency dependence, but not all the frequencies will be of the same importance, allowing us to have a selection criteria.

For our work, we are interested in infrared cavities, where the single mode cavity QED approach is frequently used to describe the THz resonance of the empty cavity and the way it couples with the material dipoles within the optical device, which also exhibit resonances in the same frequency range. Then, the single mode analysis is quite sufficient. To enforce this idea, we will end the chapter by reviewing some milestones in the literature in nanophotonics, highlighting the use of single cavity QED expected properties.

2.2 Cavity mode quantization

2.2.1 Classical wave equation

According to classical Electrodynamics in free space, the electric and magnetic fields behave as a unified wave-like phenomenon. Moreover, the speed of this wave, surprisingly identified as light, is obtained from the vacuum constants as $c = 1/\sqrt{\epsilon_0 \mu_0}$. This is derived from the Maxwell equations

$$\nabla \times \mathbf{E} = -\frac{\partial}{\partial t}\mathbf{B}, \tag{2.2.1}$$

$$\nabla \times \mathbf{H} = \frac{\partial}{\partial t}\mathbf{D}, \tag{2.2.2}$$

$$\nabla \cdot \mathbf{D} = 0, \tag{2.2.3}$$

$$\nabla \cdot \mathbf{B} = 0, \tag{2.2.4}$$

where $\mathbf{D} = \epsilon_\mathbf{0}\mathbf{E}$ and $\mathbf{B} = \mu_\mathbf{0}\mathbf{H}$ are the constitutive relations between the electric and displacement field, and the induction and magnetic field. From this coupled equations, we know that the Cartesian components of both electric and magnetic field obeys a wave equation as reads

$$\nabla^2 u - \frac{1}{v^2}\frac{\partial^2}{\partial t^2}u = 0. \tag{2.2.5}$$

This result can be obtained by taking the curl of Eq. (2.2.1) and introducing Eq. (2.2.2) with the correspondent use of the constitutive relations

$$\nabla \times \nabla \times \mathbf{E} = -\mu_0 \frac{\partial}{\partial t}(\nabla \times \mathbf{H}), \tag{2.2.6}$$

$$= -\mu_0 \epsilon_0 \frac{\partial}{\partial t}\left(\frac{\partial}{\partial t}\mathbf{E}\right), \tag{2.2.7}$$

and using the Gauss Law Eq. (2.2.3) and the following identity

$$\nabla \times \nabla \times \mathbf{E} = \nabla(\nabla \cdot \mathbf{E}) - \nabla^\mathbf{2}\mathbf{E}. \tag{2.2.8}$$

to have a wave equation for the electric field $\mathbf{E}$

$$\nabla^2 \mathbf{E} - \mu_0 \epsilon_0 \frac{\partial^2}{\partial t^2}\mathbf{E} = 0. \tag{2.2.9}$$

It can be found a similar route to find the wave equation for the field of magnetic induction **B**.

Equation (2.2.5) has the typical *plane wave solutions*. An electric field composed of just one of them its expressed like

$$\mathbf{E}(\mathbf{r},t) = \mathbf{n}E_0 e^{i\mathbf{k}\cdot\mathbf{r}-i\omega t} + \text{c.c.}, \tag{2.2.10}$$

where we added the c.c. symbol for the complex conjugate, ensuring the reality of the field observable. The requirement of zero charge distribution implicit in Eq. (2.2.3) imposes the restriction

$$\mathbf{n}\cdot\mathbf{k} = 0, \tag{2.2.11}$$

stating the transversal nature of the electric field with respect to the propagation of the wave indicated by **k**. This particular result is not exactly fulfilled in real cavities, as the multi–mode field can have a component parallel to the propagation. Besides, the transversal component of the electric field can always be decomposed in two unit vector for the plane as

$$\mathbf{E}(\mathbf{r},t) = (\mathbf{n_1}E_1 + \mathbf{n_2}E_2)\, e^{i\mathbf{k}\cdot\mathbf{r}-i\omega t} + \text{c.c.}, \tag{2.2.12}$$

where E_1 and E_2 can be complex, allowing for different types of polarization [1] , due the phase difference between these two amplitudes.

2.2.2 Single mode in a cavity

We will consider an empty region of the space with volume $V = SL$ confined by ideal mirrors of transversal area S, separated by a length L. The wave axis is z, and then the electric and magnetic field rely on the $x-y$ plane. These mirrors are assumed to be perfect conductors, and set the boundary conditions for the electric field to be zero in the frontiers. We can select one of the possible stationary modes inside the cavity, that reads

$$E_x(z,t) = Aq(t)\sin(kz), \tag{2.2.13}$$

[1] If both have the same phase, then the light is called *linearly polarized*. The opposite cases give raise to the well known *circular* or *elliptically* polarized light typical in Optics setups.

where $k = \omega/c$ [2], A is an amplitude with dimensions of electric field over length, and $q(t)$ is a dynamic variable with length dimensions, that can be treated as the canonical coordinate, in analogy with mechanical harmonic oscillators [61].

This expression can be used to derive the magnetic field $H_y(z,t)$ together with eq. (2.2.2) to be

$$H_y(z,t) = \frac{\epsilon_0 A}{k}\dot{q}(t)\cos(kz). \tag{2.2.14}$$

Then, the Hamiltonian of the system is expressed as

$$\mathcal{H} = \frac{1}{2}\int_V \left\{\epsilon_0 E_x^2 + \mu_0 H_y^2\right\} \mathrm{d}\beta \tag{2.2.15}$$

$$= \frac{1}{2}\{p^2 + \omega^2 q^2\}, \tag{2.2.16}$$

where $p = \dot{q}$ is the conjugated momentum considering $m = 1$. Notice that we arrived to the Hamiltonian for a single *Harmonic Oscillator* relying in the relationship $A = \sqrt{2\omega^2/(\epsilon_0 V)}$.

2.2.3 Correspondence rule

What we call *correspondence rule* is the promotion of the canonical variables in the Hamiltonian for the classical harmonic oscillator to *operators* acting in a Hilbert space

$$q \to \hat{q}, \text{ and } p \to \hat{p}, \tag{2.2.17}$$

together with the commutation rule for this operators

$$[\hat{q}, \hat{p}] = i\hbar\mathbf{1}, \tag{2.2.18}$$

where $\mathbf{1}$ is the identity operator, that in general is assumed to be hidden. The Hamiltonian, Electric and Magnetic field now are also operators. These two last fields play the role of canonical operators, like the position and momentum of a

[2] In principle, as the boundary conditions set $k = n\pi/L$, there are infinite but countable number of modes. To simplify the analysis, let's consider just one of those modes as this will not modify the subsequent argument.

mechanical oscillator. Their explicit forms are

$$\hat{H} = \frac{1}{2}\{\hat{p}^2 + \omega^2\hat{q}^2\}, \tag{2.2.19}$$

$$\hat{E}_x(z,t) = \sqrt{\frac{2\omega^2}{\epsilon_0 V}}\hat{q}\sin(kz), \tag{2.2.20}$$

$$\hat{B}_y(z,t) = \frac{\mu_0\epsilon_0}{k}\sqrt{\frac{2\omega^2}{\epsilon_0 V}}\hat{p}\cos(kz). \tag{2.2.21}$$

This results are exact, however the regular way to use this formalism of a quantized harmonic oscillator is by using a canonical transformation to the operators of *annihilation* $\hat{a} = (1/\sqrt{2\hbar\omega})(\omega\hat{q} + i\hat{p})$ and its hermitian conjugate version, the *creation* operator $\hat{a}^\dagger = (1/\sqrt{2\hbar\omega})(\omega\hat{q} - i\hat{p})$ [3]. Under this transformation, the observables of our interest look like

$$\hat{H} = \hbar\omega\left\{\hat{a}^\dagger\hat{a} + \frac{1}{2}\right\}, \tag{2.2.22}$$

$$\hat{E}_x(z,t) = \sqrt{\frac{\hbar\omega}{\epsilon_0 V}}(\hat{a} + \hat{a}^\dagger)\sin(kz), \tag{2.2.23}$$

$$\hat{B}_y(z,t) = \frac{1}{i}\sqrt{\frac{\hbar\omega}{V/\mu_0}}(\hat{a} - \hat{a}^\dagger)\cos(kz). \tag{2.2.24}$$

The amplitudes $\mathcal{E}_0 = \sqrt{\hbar\omega/\epsilon_0 V}$ and $\mathcal{B}_0 = \sqrt{\hbar\omega/(V/\mu_0)}$ are the fields *per photon* [21]. Finally, it will be useful to have at hand the reverse relationships connecting the annihilation and creation operator with respect to the canonical coordinates operators

$$\hat{q} = \sqrt{\frac{\hbar}{2\omega}}(\hat{a} + \hat{a}^\dagger), \quad \text{and} \quad \hat{p} = \sqrt{\frac{\hbar\omega}{2}}(\hat{a} - \hat{a}^\dagger) \tag{2.2.25}$$

implying that

$$\langle\hat{q}\rangle = \sqrt{\frac{2\hbar}{\omega}}\mathrm{Re}[\langle\hat{a}\rangle], \quad \text{and} \quad \langle\hat{p}\rangle = \sqrt{2\hbar\omega}\mathrm{Im}[\langle\hat{a}\rangle] \tag{2.2.26}$$

[3] Remember that in linear systems, operators eigenvalues are real for hermitian operators obeying $\hat{A}^\dagger = \hat{A}$, and then the hermicitity of the $\hat{q}$ and $\hat{p}$ is required. This also implies that $\hat{a}$ and $\hat{a}^\dagger$ are non hermitian, a fact that can be seen from the eigenvalues α of $\hat{a}$, that are c-numbers encoding the information of a coherent state $\hat{a}|\alpha\rangle = \alpha|\alpha\rangle$.

2.2.4 Eigenstates of the single mode quantum Hamiltonian

An important property of the previous representations in terms of $\hat{a}$ and $\hat{a}^\dagger$ is that they allow the direct diagonalization of the Hamiltonian by using the *number states* $|n\rangle$; a special type of vector in an infinite dimensional Hilbert space called *Fock Space*. They are eigenstates of the Hamiltonian, and the related eingenvalues constitute the energy spectrum of the single mode harmonic oscillator:

$$\hat{H}|n\rangle = \hbar\omega\left(\hat{a}^\dagger\hat{a} + \frac{1}{2}\right)|n\rangle = \hbar\omega(n+1/2)|n\rangle. \tag{2.2.27}$$

These energy values, $E_n = \hbar\omega(n+1/2)$ are equidistant between them with energetic transition $\Delta E = \hbar\omega$, and presents a minimal, ground energy, or *vacuum energy*, that is nonzero and equal to $E_0 = \hbar\omega/2$. This last statement is presented frequently to introduce the Casimir effect, due to the zero point fluctuations of the EM field [4] . Also, it is a signature of a quantum harmonic oscillator in general, not just for the quantization of the EM field: any other non harmonic potential will produce, under quantization, a non equidistant energy spectrum.

It can probed that these states forms a complete set, obeying the following decomposition

$$\sum_{n=0}^{\infty} |n\rangle\langle n| = \mathbf{1}, \tag{2.2.28}$$

The annihilation and creation operators act on the number states in the following way [5]

$$\hat{a}|n\rangle = \sqrt{n}|n-1\rangle, \quad \hat{a}^\dagger|n\rangle = \sqrt{n+1}|n+1\rangle. \tag{2.2.29}$$

and then they are not diagonal in the $\{|n\rangle\}_{n=0}^{\infty}$ basis. It is my intention to show explicitly these operators in the number state representation, as it is usual to take

[4] In any of the following chapter, we are going to hidden this vacuum energy, as our discussions relying always in the physics derived from energy transitions.

[5] This is the reason why these operators are called *ladder* operators, as they allow to move between the subsequent number states, up or downward.

just a portion of these expansions for numerical (and finite) purposes:

$$\hat{H} = \hbar\omega \sum_{n=0}^{\infty} (n + 1/2)|n\rangle\langle n|, \tag{2.2.30}$$

$$\hat{a} = \sum_{n=1}^{\infty} \sqrt{n}|n-1\rangle\langle n|, \tag{2.2.31}$$

$$\hat{a}^\dagger = \sum_{n=0}^{\infty} \sqrt{n+1}|n+1\rangle\langle n|. \tag{2.2.32}$$

2.2.5 Examples of field dynamics

Assumed the single mode QED to be a closed system, the system evolution is unitary, and then we can derive the evolution of the system state as $|\psi(t)\rangle = \hat{U}|\psi(0)\rangle$, where the unitary operator can be written in the form $\hat{U}(t) = C(t)\exp[\mathrm{a}(t)\hat{a}^\dagger\hat{a}]$ [41] following the quantum harmonic oscillator Hamiltonian $\hat{H} = \omega\hat{a}^\dagger\hat{a}$, where $\hbar = 1$. By applying the Schrödinger equation for the time-evolution operator we obtain

$$i\frac{\mathrm{d}}{\mathrm{dt}}\hat{U} = \hat{H}\hat{U}, \tag{2.2.33}$$

$$\Rightarrow i\left(\frac{\dot{C}}{C} + \dot{\mathrm{a}}\hat{a}^\dagger\hat{a}\right)\hat{U} = \omega\hat{a}^\dagger\hat{a}\hat{U}, \tag{2.2.34}$$

$$\Rightarrow \hat{U}(t) = \exp[-i\omega t\hat{a}^\dagger\hat{a}]. \tag{2.2.35}$$

This means, for example, that if the field initial state is some combination of number states $|\psi(0)\rangle = \sum_n c_n|n\rangle$, the evolution at time t will be

$$|\psi(t)\rangle = \sum_n c_n e^{-i\omega n t}|n\rangle \tag{2.2.36}$$

If the field state under consideration is initially in a *coherent state*, this is, a eigenstate of the annihilation operator $\hat{a}|\alpha\rangle = \alpha|\alpha\rangle$, with

$$|\psi(0)\rangle = |\alpha\rangle = e^{-|\alpha|^2/2}\sum_{n=0}^{\infty}\frac{\alpha^n}{\sqrt{n!}}|n\rangle, \tag{2.2.37}$$

then the dynamics will translate to rotations at frequency ω of the coherent parameter

$$\alpha(t) = \langle \hat{a}(t) \rangle = \langle \alpha(t) | \hat{a} | \alpha(t) \rangle = \alpha e^{-i\omega t} \tag{2.2.38}$$

keeping the mean number of photons $\mathrm{Tr}[\hat{a}^\dagger \hat{a} |\alpha\rangle\langle\alpha|] = |\alpha|^2$. The system predicts no transition to higher or lower energy steps.

Let's visit a more interesting example.

2.2.5.1 Harmonic oscillator with a classical driving

The general form for a classically driven Harmonic quantum oscillator is expressed as reads [42]

$$\hat{H} = \omega \hat{a}^\dagger \hat{a} + F_\mathrm{d}(t)\hat{a} + F_\mathrm{d}^*(t)\hat{a}^\dagger. \tag{2.2.39}$$

where $F_\mathrm{d}(t)$ represent the (classical) pumping field. We use the later argument to write the evolution operator as follows

$$\hat{U}(t) = C(t) e^{\mathrm{a}(t)\hat{a}^\dagger \hat{a}} e^{\mathrm{b}(t)\hat{a}^\dagger} e^{\mathrm{c}(t)\hat{a}}, \tag{2.2.40}$$

$$\begin{aligned} \Rightarrow \frac{\mathrm{d}}{\mathrm{dt}}\hat{U} &= \left(\frac{\dot{C}}{C} + \dot{\mathrm{a}}\hat{a}^\dagger \hat{a} + \dot{\mathrm{b}} e^{\mathrm{a}\hat{a}^\dagger \hat{a}} \hat{a}^\dagger e^{-\mathrm{a}\hat{a}^\dagger \hat{a}} + \dot{c} e^{\mathrm{a}\hat{a}^\dagger \hat{a}} e^{\mathrm{b}\hat{a}^\dagger} \hat{a} e^{-\mathrm{b}\hat{a}^\dagger} e^{-\mathrm{a}\hat{a}^\dagger \hat{a}} \right) \hat{U} \\ &= \left(\frac{\dot{C}}{C} + \dot{\mathrm{a}}\hat{a}^\dagger \hat{a} + \dot{\mathrm{b}} e^{\mathrm{a}} \hat{a}^\dagger + \dot{\mathrm{c}}(e^{-\mathrm{a}}\hat{a} - \mathrm{b}) \right) \hat{U} \end{aligned} \tag{2.2.41}$$

In this derivation it was used the Baker–Campbell–Hausdorff formula to derive the formulae $e^{\alpha \hat{a}^\dagger \hat{a}} \hat{a}^\dagger e^{-\alpha \hat{a}^\dagger \hat{a}} = e^{\alpha} \hat{a}^\dagger$ or $e^{\beta \hat{a}^\dagger} \hat{a} e^{-\beta \hat{a}^\dagger} = \hat{a} - \beta$. By comparing with the Heisenberg equation for the evolution operator, we have

$$i \left(\frac{\dot{C}}{C} - \mathrm{b}\dot{\mathrm{c}} \right) + i\dot{\mathrm{a}}\hat{a}^\dagger \hat{a} + i\dot{\mathrm{c}} e^{-\mathrm{a}} \hat{a} + i\dot{\mathrm{b}} e^{\mathrm{a}} \hat{a}^\dagger = \omega \hat{a}^\dagger \hat{a} + F_\mathrm{d}(t)\hat{a} + F_\mathrm{d}^*(t)\hat{a}^\dagger. \tag{2.2.42}$$

The system of equations implied, that we obtain by comparing the operator coefficients in both sides of the equation above, is easy to solve; the solution for arbitrary driving function considers $\mathrm{a}(t) = -i\omega t$, $\mathrm{b}(t) = -\mathrm{c}^*(t)$ and

$$\mathrm{c}(t) = -i \int_0^t \mathrm{d}\tau e^{-i\omega\tau} F_\mathrm{d}(\tau), \tag{2.2.43}$$

$$C(t) = \exp\left[- \int_0^t \mathrm{d}\tau e^{i\omega\tau} F_\mathrm{d}(\tau) \int_0^\tau \mathrm{d}\tilde{\tau} e^{-i\omega\tilde{\tau}} F_\mathrm{d}^*(\tilde{\tau}) \right]. \tag{2.2.44}$$

Let's see what is the evolution of an interesting initial state as the *vacuum* by applying $|\psi(t)\rangle = \hat{U}(t)|0\rangle$ for driving functions obeying $\mathrm{Im}[F_\mathrm{d}(t)e^{-i\omega t}] = 0$:

$$|\psi(t)\rangle = C(t)\sum_{n=0}^{\infty}\frac{(\mathrm{b}(t)e^{-i\omega t})^n}{\sqrt{n!}}|n\rangle, \tag{2.2.45}$$

$$= |\mathrm{b}(t)e^{-i\omega t}\rangle \tag{2.2.46}$$

where we use the definition of the displacement operator

$$\hat{D}(\alpha) = e^{\alpha\hat{a}^\dagger - \alpha^*\hat{a}} = e^{-|\alpha|^2/2}e^{\alpha\hat{a}^\dagger}e^{-\alpha^*\hat{a}}, \tag{2.2.47}$$

and its action on the vacuum

$$\hat{D}(\alpha)|0\rangle = e^{-|\alpha|^2/2}\sum_{n=0}^{\infty}\frac{\alpha^n}{\sqrt{n!}}|n\rangle. \tag{2.2.48}$$

I want to emphasize this result: what we obtain from an initial vacuum state is always a *coherent state*. Its evolution is dictated by the shape of the driving pulse, codified in $\mathrm{b}(t)$. The mean number of photons bouncing in the cavity, that is just the square of the absolute value of α, corresponds to $\langle\hat{a}^\dagger\hat{a}(t)\rangle = |\mathrm{b}(t)|^2$.

Finally, the "classical" energy that is transferred from the driving field to the cavity can be calculated with the help of Equations (2.2.26):

$$E_\mathrm{cl}(t) = \frac{1}{2}\left\{\langle\hat{p}(t)\rangle^2 + \omega^2\langle\hat{q}(t)\rangle^2\right\}, \tag{2.2.49}$$

$$= \omega|\langle\hat{a}(t)\rangle|^2 = \omega|\mathrm{b}(t)|^2, \tag{2.2.50}$$

In particular, if the driving function obeys $F_\mathrm{d}(t) = F_0\varphi(t)e^{i\omega t}$ with $\varphi(t)$ a real function, then we have that

$$E_\mathrm{cl}(t) = \omega|F_0|^2\left(\int_0^t\varphi(\tau)\mathrm{d}\tau\right)^2 \tag{2.2.51}$$

It is interesting, also, that the time-dependent probability $P_{|0\rangle}(t)$ to find the state of the system in the vacuum state is expressed in terms of this classical energy:

$$P_{|0\rangle}(t) = |\langle 0|\mathrm{b}(t)e^{-i\omega t}\rangle|^2 = e^{-|\mathrm{b}(t)|^2} = e^{-E_\mathrm{cl}(t)/\omega}. \tag{2.2.52}$$

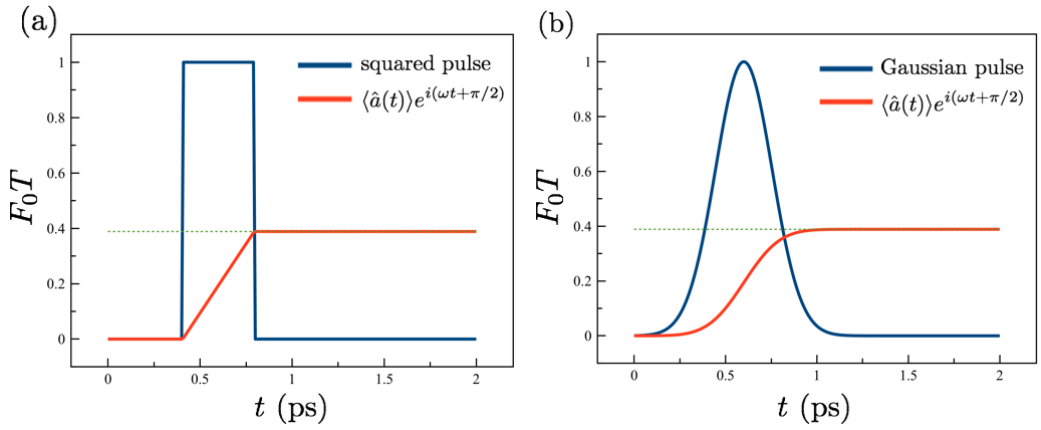

Figure 2.2.1: Coherent state evolution (orange lines) for two different pulse shapes (blue lines). The temporal widths have been chosen in order to have both functions with equal normalization condition. Green dashed lines indicate the steady value for the cavity coherences to be $F_0T_1 \approx 0.389$, in both cases. (a) Coherence evolution for the cavity mode driven by a squared pulse with center $t_0 = 0.6$ (ps), width $T_1 = \sqrt{2\pi} \times 0.155$ (ps) and $F_0 = 1$ (THz). (b) Cavity driven by a Gaussian pulse with center $t_0 = 0.6$ (ps), width $T_2 = 0.155$ (ps) and $F_0 = 1$ (THz).

The conclusion is direct: for high enough energy driven in the cavity, it is less probable to find the cavity in the vacuum state.

2.2.5.2 Resonant driving pulse with an step envelope

We start the examples with a squared pulse (an "step" function) with frequency carrier resonant to the cavity mode $\omega_{\rm d} = \omega$, like the one plotted in Figure (2.2.1-a). Then,

$$F_{\rm d}(t) = F_0\Pi\left(\frac{t-t_0}{T}\right)e^{i\omega t} = \begin{cases} F_0e^{i\omega t} & , \text{ if } t_0 - \frac{T}{2} < t < t_0 + \frac{T}{2} \\ 0 & , \text{ elsewhere} \end{cases} \tag{2.2.53}$$

where t_0 is the center and T is the temporal width of the pulse, respectively. This case can represent a continuous laser with an ultra-fast switching in the instants $t = t_0 \pm T/2$. The state at time t is $|{\rm b}(t)e^{-i\omega t}\rangle$ with

$$\mathrm{b}(t) = -iF_0\int_0^t {\rm d}\tau\Pi\left(\frac{\tau-t_0}{T}\right) = \begin{cases} 0 & , \ t \le t_0 - T/2 \\ -iF_0(t - t_0 + T/2)) & , \ t_0 - \frac{T}{2} < t < t_0 + \frac{T}{2} \\ -iF_0T & , \ t \ge t_0 - T/2 \end{cases} \tag{2.2.54}$$

The field coherence $\langle\hat{a}(t)\rangle = {\rm b}(t)e^{-i\omega t}$ represent an amplitude growing from zero in a ramp up to a stationary value, always with a constant phase of -90^o, and

rotating at angular frequency ω. The stationary classical energy transferred to the cavity field is

$$E_{\text{cl,ss}} = \omega(F_0 T)^2. \tag{2.2.55}$$

2.2.5.3 Resonant driving pulse with a Gaussian envelope

In this case we have that

$$F_{\text{d}}(t) = F_0 e^{-\frac{(t-t_0)^2}{2T^2}} e^{-i\omega t}, \tag{2.2.56}$$

where it is straightforward to derive the dynamical coherent parameter to be

$$\text{b}(t) = \langle \hat{a}(t) \rangle e^{i\omega t} = -iF_0 T \sqrt{\frac{\pi}{2}} \left(\text{erf}\left[\frac{t_0}{\sqrt{2}T} \right] + \text{erf}\left[\frac{t-t_0}{\sqrt{2}T} \right] \right) \tag{2.2.57}$$

As you can see from Figure (2.2.1-b), the smooth Gaussian will generate a smooth evolution of the cavity coherence up to its steady value $\sim -i\sqrt{2\pi}F_0 T$. The stationary classical energy transferred to the cavity field is

$$E_{\text{cl,ss}} = \omega 2\pi (F_0 T)^2. \tag{2.2.58}$$

2.3 Single cavity mode in the scientific literature

The use of a single cavity QED mode in Nanophotonics is widespread in the scientific literature, even when it is just an approximation that works, apparently pretty good. One might ask however, how much we trust in the validity of this model. As any experimental realization, and any "cavity" or "resonator", surely will present a complex and well structured spectrum for a lot of possible reasons ¿How can we be calm about choosing only one mode, discarding everything else?[6].

In the following section we will see how we *include* all of the infinite remaining modes with the label of *environment*. This means that we treat the whole

[6]This concern is related, just in part, to the way we truncate a structured spectrum of a nanocavity and how we single out just one of them from which we obtain the electric and magnetic induction fields. From the covariant formulation of Electrodynamics we know that there is some freedom in the way we choose the potentials $\{\phi(t), \vec{A}(t)\}$. This, added to the quantization method applied, in some cases, would generate different values from observables depending on the gauge choice. This ambiguity is obviously a non physical artefact that must be analyzed carefully, at least in the relativistic regime. Although these aspects goes beyond the scope of this work I strongly suggest to read a recent article tackling this problem [67].

electromagnetic spectrum by parts, giving to each one a different level of "physical influence".

Here we will not address these aspects in deep detail. Instead, suffice it to say that the current literature contains successful examples of the application of this minimal model that we proceed to review in the next lines. In turn, there are other approaches available, if the complexity of the problem under study requires a higher level of detail. Some interesting examples are documented in [60, 29].

2.3.1 Seminal experiments

The publication "Cavity Quantum Electrodynamics" [27] is of paramount importance as gives a detailed account on early quantum experiments aiming for the strong coupling of matter excitations, using Rydberg atoms in microwave and optical cavities.

These experiments demonstrates that spontaneous radiation from excited atoms can be greatly suppressed or enhanced by placing the atoms between mirrors or in cavities. Some experimental realizations mentioned are:

- About the inhibition of spontaneous emission from Rydberg states of cesium atoms in a beam as they passed between two 20-cm-long aluminum mirrors (the *cavity*) separated by approximately $L = 0.2$ mm, by monitoring their atomic radiation at $\lambda = 0.45$ mm [34][7].
- The enhanced spontaneous (by a factor of ~ 500) emission in the millimeter wave regime for Rydberg atoms of sodium coupled to a Fabry-Perot cavity [23], where the cavity was resonant to the dipole transition, at around 340 GHz[8].
- Rabi oscillations induced by a small thermal field in the superconducting microwave cavity at 21.6 GHz and 2.5 K [58]. This is one of the first experiments showing clearly the collapse and revival predicted by the *Jaynes-Cummings model* [37], which is again, a model of one atom modeled as a two level system, and a single cavity mode.

[7] The gap between mirrors was built for optical frequencies. The idea is that by increasing the ratio $\lambda/(2d) > 1$, the signal coming from excited atoms detected at the cavity exit increase, confirming the inhibition of spontaneous emission rate.

[8] We are going to develop a theory for this phenomenon called *Purcell effect* [57] in Chapter 5.

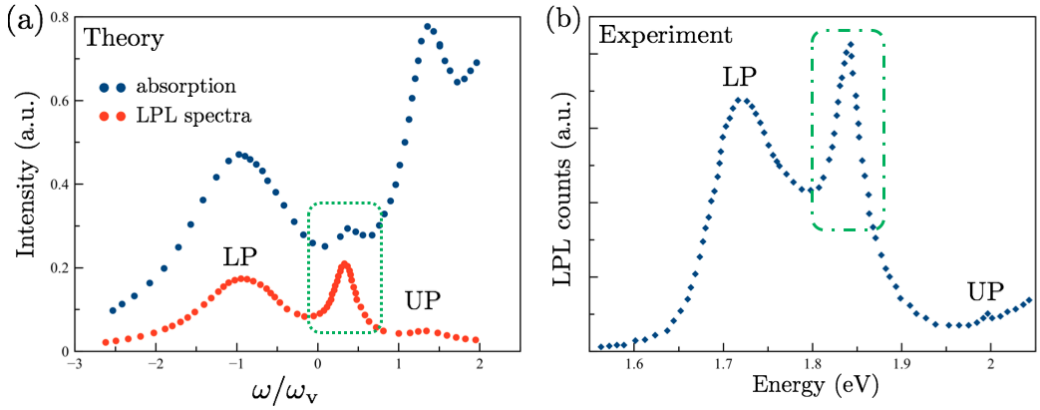

Figure 2.3.1: (a) Absorption and photoluminiscence simulation data for an organic microcavity with N = 20 emitters from [31]. (b) Experimental LPL spectrum obtained by [33] for the organic cavity simulated in (a) .

The rate of spontaneous emission of the atom, e.g. the probability Γ_0 of photon emission per unit time, depends on the coupling rate Ω_{eff} of matter with respect to the electromagnetic vacuum, which can be dramatically changed if the electric field is confined to an small volume instead of free space[9]. This coupling of the individual atom to the cavity field at frequency ω is calculated with the *Rabi* frequency

$$\Omega_{\text{eff}} = d_{\text{eff}}\mathcal{E}_0/\hbar \tag{2.3.1}$$

where $\mathcal{E}_0 = \sqrt{\hbar\omega/(\epsilon_0 V)}$ is the electric field amplitude per photon in the quantization volume V and d_{eff} is the matrix element of the electric dipole of the two-level atom. As you can see, all these equations consider the case of an atom and the field exchanging energy if there were only a single mode of the field. The underlying theory showed great prediction power in relation to the experimental results obtained and, historically, it greatly encouraged the development of this area of research.

2.3.2 Simulations of molecular spectroscopy observables

Most of the experiments commented in the previous subsection consider microwave Fabry-Perot cavities to couple, resonantly or not, to specific transitions in Rydberg atoms. One associates, in general, atoms with applications in quantum computing, to give an example. Alternatively, it is known that molecules in quantum cavities

[9]This coupling rate also affects the probability $P_e(t)$ of finding the atom in its excited state at time t, assuming it was prepared in this state at time 0, that in the single mode approach shows the well now Rabi oscillations.

promise applications in control of chemical reactions [35].

The prediction power of hybrid light-matter Hamiltonians containing just a single cavity mode have an impressive example in the Holstein-Tavis-Cummings (HTC) Hamiltonian [30], where the cavity mode, electronical potentials and vibrational degrees of freedom are treated in the same footing. Roughly speaking, the HTC model consists of one single cavity QED mode with frequency ω_c, N intramolecular vibrations with frequency ω_v, modeled as quantum harmonic oscillators, and N two-level systems modeling the electronic excitations with transitions ω_e, where the only missing coupling in the interaction term is between the cavity mode and the vibrations.

We show in Figure (2.3.1-a) the simulations carried using this Hamiltonian[10] to reproduce some experimental observables reported in [33], for cyanine dye J aggregates in a low-Q microcavity, whose experimental photoluminiscence spectrum is shown in Fig. (2.3.1-b).

The model predicts the emergence of several types of dark states, this is, hybrid resonances poorly or completely invisible from absorption although they can radiate. This is confirmed by the simulations plotted in Figure (2.3.1-a) where it appears a weak peak lower, but close, to the vibrational frequency $\omega/\omega_v \approx 0.4$ (green dashed rounded rectangles) in the absorption curve (blue points), that becomes much larger in the LPL curve[11] (orange points), and is even larger than the Lower Polariton (LP) and Upper Polariton (UP) side-bands, that are the bright states we expect in a strong coupling regime, forming a frequency splitting around the vibrational resonance $\omega/\omega_v = 1$. This is just what we see from the experimental LPL spectrum, where we enclose the dark resonance between a less stronger LP peak and a vanished UP resonance, as it is shown from the simulations.

2.4 Final comments

The examples shown previously does not demonstrate that it is enough to take just one cavity mode, always. However, in most of the cases reported, the single

[10] Joined to a formal treatment of the dissipative dynamics that we will discuss in Chapter 2.
[11] This means Leak PhotoLuminiscence (LPL), or just the photoluminescence spectra through the mirrors of the cavity.

cavity QED approach captures the most fundamental features of the problems under study, although there are some complexities not mentioned that are going to be the central theme of the next sections.

Anyway, the intention was to give a *flavour* of the formalism and to show that we can "do interesting physics" when we treat the electromagnetic field in its quantum version.

Chapter 3

Open Quantum Systems

3.1 Introduction

The usual way to interpret spectroscopic data is by recognizing frequency peaks or dips [1]; broad up to the point to be considered frequency bands, or isolated resonances if they look narrow enough. We assume that a resonance dip in the absorption of a certain sample evidences a driven energy transition of two internal levels, physically expressed with the equation $\Delta E = E_{\nu'} - E_{\nu} = \hbar\omega_{\text{dip}}$, where the frequency $\omega_{\text{dip}} = \Delta E/\hbar$ is taken from the center of the dip.

But, if the theory seems to talk about precise transitions between quantized energy states, then, how we explain the *peak and dip widths* measured? Why there are narrower or broader bands in a spectrum, instead of perfectly sharp resonances?

This is because in Nature, broadly speaking, nothing is "closed", as we assume in the previous chapter for our single mode cavity QED. Instead, there is always a complex combination of coherent or incoherent random processes among several degrees of freedom *overlapped with the system of interest*, causing broadening, sharpening and/or frequency shifts, among others, that prevent us to observe ideal sharp peaks [2].

The idea of this chapter is to introduce consistently a way to "open" our small quantum harmonic system to treat, approximately but as correct as possible, the lossy effect of the surrounding universe, that in the quantum jargon is

[1] Or *energy peaks and dips* depending on technical jargon.
[2] In a mathematical language, we do not see isolated *Dirac Deltas* in the spectrum.

called "decoherence" and/or "dephasing". In this formalism, the environment (the *reservoir* or *bath*) is modeled as an infinite collection of harmonic oscillators in internal thermal equilibrium, with a spectral density that encapsulates the characteristic time of its internal fluctuations (the bath correlation time t_{R}), which we are going to assume it is much faster than the oscillator lifetime, and then allows us to do perturbative assumptions. What we finally obtain is the influence of the environment reduced to parameters in a Quantum Master Equation for the reduced density operator of interest, in Lindblad form [47], that we can write as $(\mathrm{d}\hat{\rho}_{\mathrm{S}}/\mathrm{dt}) = \mathcal{L}\hat{\rho}_{\mathrm{S}}$.

One of the main conclusions derived by this formalism and applied to the near field of a cavity QED mode, is that the bandwidth of the resonances observed in cavity reflection or transmission setups encodes the influence the free electromagnetic field (the *big reservoir*) in thermal equilibrium onto the cavity density of modes.

3.2 System plus reservoir approach

In the previous chapter, the cavity quantum harmonic oscillator shown was considered a closed system by default: there is no energy flux by its boundaries because there is nothing more in space than the cavity and its mirrors with infinite conductance. In reality, an optical cavity has non perfect mirrors, with frequency and intensity dependent finite transmission, and then can interact with the environment. We say that the cavity is an open system and then the evolution of any of the parts have not necessarily an unitary evolution. These reasons, together with the fact that the environment usually has much more degrees of freedom an complexity than the main system, forces us to seek for Quantum Master Equations that allow us to calculate the evolution of our subsystems of interest in a systematic and simplified way [3].

We can model the interaction of a single cavity mode with an ensemble of harmonic

[3] "*In general, for all but the most basic of Hamiltonians, an analytical description of the system dynamics is not possible, and one must resort to numerical simulations of the equations of motion. In absence of a quantum computer, these simulations must be carried out using classical computing techniques, where the exponentially increasing dimensionality of the underlying Hilbert space severely limits the size of system that can be efficiently simulated. However, in many fields such as quantum optics, trapped ions, superconducting circuit devices, and most recently nanomechanical systems, it is possible to design systems using a small number of effective oscillator and spin components, excited by a limited number of quanta, that are amenable to classical simulation in a truncated Hilbert space.*" Quote from the *QuTiP* documentation.

oscillators, that we are going to think as the thermal bath of free EM modes [4]. The Hamiltonian of such closed system is expressed as reads

$$\hat{\mathcal{H}} = \hat{\mathcal{H}}_0 + \hat{\mathcal{H}}_{\text{int}}, \tag{3.2.1}$$

$$\hat{\mathcal{H}}_0 = \hat{\mathcal{H}}_{0,\text{c}} + \hat{\mathcal{H}}_{0,\mathcal{R}}, \tag{3.2.2}$$

$$= \hbar\omega_{\text{c}}\hat{a}^\dagger\hat{a} + \sum_{\{j\}} \hbar\omega_j \hat{c}_j^\dagger \hat{c}_j, \tag{3.2.3}$$

$$\hat{\mathcal{H}}_{\text{int}} = \sum_{\{j\}} \hbar\kappa_j(\hat{a}^\dagger\hat{c}_j + \hat{c}_j^\dagger\hat{a}), \tag{3.2.4}$$

$$= \hat{a}^\dagger\hat{K} + \hat{K}^\dagger\hat{a} \tag{3.2.5}$$

where the interaction Hamiltonian is written in a form that conserves the number of excitations of the system [5]. We have implicitly defined $\hat{K} = \sum_{\{j\}} \hbar\kappa_j\hat{c}_j$, where the sum runs arbitrarily in discrete and probably infinite $j-$modes. If the single cavity mode plus reservoir is a closed system, then the evolution of the full density operator $\hat{\rho}_{\text{Full}}$ obeys the Schrodinger equation. To solve this equation, it is usual to use the *interaction picture*, where

$$\tilde{\mathcal{H}}_{\text{int}}(t) = e^{i\hat{\mathcal{H}}_0 t/\hbar}\hat{\mathcal{H}}_{\text{int}}e^{-i\hat{\mathcal{H}}_0 t/\hbar}, \tag{3.2.6}$$

$$= \sum_{\{j\}} \hbar\kappa_j(e^{i(\omega_{\text{c}}-\omega_j)t}\hat{a}^\dagger\hat{c}_j + e^{-i(\omega_{\text{c}}-\omega_j)t}\hat{c}_j^\dagger\hat{a}), \tag{3.2.7}$$

and $\tilde{\rho}_{\text{Full}} = e^{-i\hat{\mathcal{H}}_0 t/\hbar}\hat{\rho}_{\text{Full}}e^{i\hat{\mathcal{H}}_0 t/\hbar}$. This representation is best suited for approximations involving time scales comparisons, as we can see: we separate the dynamics related with the free Hamiltonian from the interaction part, that we are going to assume is slower than the former. It can be derived a convenient, but exact, shape of the Schrodinger equation for the full density operator as reads

$$\frac{\text{d}}{\text{d}t}\tilde{\rho}_{\text{Full}} = \frac{1}{i\hbar}[\tilde{\mathcal{H}}_{\text{int}}(t), \tilde{\rho}_{\text{Full}}(0)] - \frac{1}{\hbar^2}\int_0^t [\tilde{\mathcal{H}}_{\text{int}}(t), [\tilde{\mathcal{H}}_{\text{int}}(t'), \tilde{\rho}_{\text{Full}}(t')]]\text{d}t' \tag{3.2.8}$$

This equation shows, in the second term, that we have a second order contribution of the interaction Hamiltonian to the dynamics of the coupled system. It seems

[4] As is stated in [10], the formalism treated has some arbitrariness, as the coupled ensemble of harmonic oscillators can represent other dissipative mechanisms, as vibrations in a crystal, to give an example.

[5] This is the typical *Rotating Wave Approximation* RWA assumed in certain light-matter system approaches. It is also the simplest way to address coherent coupling between oscillators.

that we are in the right route for our first approximation. But before, we are interested in finding an equation for the reduced density operator of the cavity $\tilde{\rho} = \mathrm{tr}_{\mathcal{R}}[\tilde{\rho}_{\mathrm{Full}}]$. After tracing over the reservoir space in Equation (3.2.8), and some algebra, we have that

$$\frac{\mathrm{d}}{\mathrm{dt}}\tilde{\rho} = -\frac{1}{\hbar^2}\int_0^t \mathrm{tr}_{\mathcal{R}}\left\{[\tilde{\mathcal{H}}_{\mathrm{int}}(t), [\tilde{\mathcal{H}}_{\mathrm{int}}(t'), \tilde{\rho}_{\mathrm{Full}}(t')]]\right\}\mathrm{d}t' \tag{3.2.9}$$

What happens with the non integral term in eq. (3.2.8)? This $c-$number term can always be arranged in the Hamiltonian to vanish at this stage of the calculation.

In Equation (3.2.9), there are some issues that I want to highlight:

- The integral contains the full density operator evaluated in the primed time $0 \leq t' < t$. We notice that the shape of this equation is self-referential as both $\tilde{\rho}(t)$ and $\tilde{\rho}_{\mathrm{Full}}(t)$ are unknown.
- The interaction Hamiltonian appears twice in a product. Then, we will have terms proportional to $\kappa_j\kappa_{j'}$. If we make sure that, in general, $\omega_{\mathrm{c}}^2 \gg \kappa_j\kappa_{j'}$, then the coupling with the bath is weak and we expect that the *small* cavity system will not change the reservoir dynamics in an important manner.

3.2.1 Born approximation

Obviously, the cavity system will be affected by the reservoir in some manner and then $\tilde{\rho}_{\mathrm{Full}}(t)$ will not be separable always. Is there a well founded way to express that the density operator is almost separable at all times, as the reservoir will not change considerable from the initial state? Let's think that the initial state of the coupled system is separable and the reservoir is in thermal equilibrium at temperature T [6]:

$$\hat{\rho}_{\mathrm{Full}}(0) = \hat{\rho}(0)\hat{\mathcal{R}}, \tag{3.2.10}$$

$$\hat{\mathcal{R}} = \prod_j \exp(-\hbar\omega_j\hat{c}_j^\dagger\hat{c}_j/(k_{\mathrm{B}}T))(1-\exp(\hbar\omega_j/(k_{\mathrm{B}}T))). \tag{3.2.11}$$

The formal way to express this idea is called *Born approximation*. It reads

$$\tilde{\rho}_{\mathrm{Full}}(t) = \hat{\rho}(t)\hat{\mathcal{R}} + \mathcal{O}(\tilde{\mathcal{H}}_{\mathrm{int}}), \tag{3.2.12}$$

[6] Taking closely a verbatim quote [10], *the reservoir can represent the vacuum radiation field into which an optical cavity mode decays through partially transmitting mirrors.*

where the $\mathcal{O}(\tilde{\mathcal{H}}_{\text{int}})$ term is a perturbation of the order of the interaction, that we are assuming weak. In practice, we take just $\tilde{\rho}_{\text{Full}}(t) = \hat{\rho}(t)\hat{\mathcal{R}}$ in Equation (3.2.9) as every product containing the perturbation $\mathcal{O}(\tilde{\mathcal{H}}_{\text{int}})$ will be a cubic power, allowing us to neglect them and keep only the second order factors.

After tracing the reservoir operators with respect to $\hat{\mathcal{R}}$, the remaining nonzero terms of the Master Equation read:

$$\frac{\mathrm{d}}{\mathrm{dt}}\tilde{\rho} = -\int_0^t \Big\{[\hat{a}\hat{a}^\dagger\tilde{\rho}(t-\tau) - \hat{a}^\dagger\tilde{\rho}(t-\tau)\hat{a}]e^{-i\omega_c\tau}\langle\tilde{K}^\dagger(t)\tilde{K}(t-\tau)\rangle_{\mathcal{R}} + \text{h.c.} \\ +[\hat{a}^\dagger\hat{a}\tilde{\rho}(t-\tau) - \hat{a}\tilde{\rho}(t-\tau)\hat{a}^\dagger]e^{i\omega_c\tau}\langle\tilde{K}(t)\tilde{K}^\dagger(t-\tau)\rangle_{\mathcal{R}} + \text{h.c.}\Big\}\,\mathrm{d}t', \quad (3.2.13)$$

where $\tau = t - t'$

$$\langle\tilde{K}^\dagger(t)\tilde{K}(t-\tau)\rangle_{\mathcal{R}} = \int_0^\infty \mathrm{d}\omega e^{i\omega\tau}g(\omega)|\kappa(\omega)|^2\langle\hat{c}_\omega^\dagger\hat{c}_\omega\rangle_{\mathcal{R}}, \quad (3.2.14)$$

$$\langle\tilde{K}(t)\tilde{K}^\dagger(t-\tau)\rangle_{\mathcal{R}} = \int_0^\infty \mathrm{d}\omega e^{-i\omega\tau}g(\omega)|\kappa(\omega)|^2(\langle\hat{c}_\omega^\dagger\hat{c}_\omega\rangle_{\mathcal{R}} + 1), \quad (3.2.15)$$

and $\langle\hat{O}\rangle_{\mathcal{R}} = \text{tr}_{\mathcal{R}}[\hat{O}\hat{\mathcal{R}}]$. Notice also that we transformed the summation in the $j-$oscillators in an integral in frequency. Explicitly

$$\langle\tilde{K}^\dagger(t)\tilde{K}(t-\tau)\rangle_{\mathcal{R}} = \sum_j |\kappa_j|^2 e^{i\omega_j\tau}\text{tr}_{\mathcal{R}}[\hat{c}_j^\dagger\hat{c}_j\hat{\mathcal{R}}] \to \int_0^\infty \mathrm{d}\omega e^{i\omega\tau}g(\omega)|\kappa(\omega)|^2\langle\hat{c}_\omega^\dagger\hat{c}_\omega\rangle_{\mathcal{R}}. \quad (3.2.16)$$

Formally, $g(\omega) = \sum_j \delta(\omega - \omega_j)$ is the spectral density of the reservoir. Also,

$$\langle\hat{c}_\omega^\dagger\hat{c}_\omega\rangle_{\mathcal{R}} = \frac{e^{-\hbar\omega/(k_{\text{B}}T)}}{1 - e^{-\hbar\omega/(k_{\text{B}}T)}} \quad (3.2.17)$$

is the mean photon number at frequency ω and temperature T. To understand the meaning of this mean value, imagine that this reservoir is at room temperature. Then $k_{\text{B}}T \approx 0.0261234$ eV. We summarize some important numbers in Table 3.2.1. At room temperature, the reservoir has an average of one photon of frequency 4.38 THz, and is less probable to find thermal photons with higher frequencies.

3.2.2 Markov approximation

In Equation (3.2.13), we have the τ dependence on the reduced density operator and then it is necessary to integrate it together with the other factors. However,

Temp. (° C)	Energy (meV)	Freq. (THz)	$\langle \hat{c}^\dagger_\omega \hat{c}_\omega \rangle_{\mathcal{R}}$
30	18.1074	4.38	1
30	26.1234	6.32	0.582
30	49.628	12	0.175926
30	165.427	40	0.00178

Table 3.2.1: Excitation mean number as a function of the temperature, energy and frequency.

we know that the time scale t of the dynamics of this operator is restricted to the decay time of the cavity coherence, that we can call as $t > t_{\mathrm{c}}$. As you can see, the dynamics of the reservoir is encapsulated in the correlation functions. If those correlations functions are limited by a time $t_{\mathcal{R}} \ll t_{\mathrm{c}}$, then we can neglect the effects on the cavity density operator by doing $\tilde{\rho}(t-\tau) \approx \tilde{\rho}(t)$. This is part of the *Markov approximation*: by doing this replacement, it looks that the evolution of the density operator in Equation (3.2.13) only depends on itself at actual time t. In this sense, we say that this approach is only valid for Markovian (or memory-less) systems. After the Markov approximation, we arrive to

$$\frac{\mathrm{d}}{\mathrm{dt}}\tilde{\rho} = (\hat{a}\tilde{\rho}\hat{a}^\dagger - \hat{a}^\dagger\hat{a}\tilde{\rho}) \int_0^t \mathrm{d}\tau \int_0^\infty \mathrm{d}\omega e^{-(\omega-\omega_{\mathrm{c}})\tau} g(\omega)|\kappa(\omega)|^2 + \mathrm{h.c.} \tag{3.2.18}$$

where we neglect the terms proportional to $\langle \hat{c}^\dagger_\omega \hat{c}_\omega \rangle$ as we know that, in the case of interest for this thesis, $\omega_c = 40$ THz and then $\langle \hat{c}^\dagger_{\omega_{\mathrm{c}}} \hat{c}_{\omega_{\mathrm{c}}} \rangle \sim 10^{-3}$ (See Table 3.2.1). We know that the integration in τ goes up to a time t_{c} higher than the correlation time of the reservoir $t_{\mathcal{R}} = \hbar/(k_{\mathrm{B}}T)$. It seems harmless then to extend the time integration in (3.2.18) to infinity. This is useful as the complex exponential inside becomes a Dirac Delta plus a principal value term like it reads

$$\int_0^\infty \mathrm{d}\tau e^{-(\omega-\omega_{\mathrm{c}})\tau} = \pi\delta(\omega-\omega_{\mathrm{c}}) + i\frac{\mathrm{P.V.}}{\omega-\omega_{\mathrm{c}}}. \tag{3.2.19}$$

This Dirac Delta will collapse the frequency integration, and the principal value will modify the resonance frequency in a manner that, in general, is neglected for being a small correction [7]. Then, keeping just the terms evaluated at ω_{c} by the Dirac Delta, we arrive to the following expression we are interested in, in the

[7] As it is mentioned in [10], this is a first contribution of the *frequency Lamb shift* that does not consider relativistic effects.

Schrodinger picture

$$\frac{\mathrm{d}}{\mathrm{dt}}\hat{\rho} = -i\omega_{\mathrm{c}}[\hat{\mathcal{H}}_{0,\mathrm{c}}, \hat{\rho}] + \frac{\tilde{\kappa}}{2}(2\hat{a}\tilde{\rho}\hat{a}^{\dagger} - \hat{a}^{\dagger}\hat{a}\tilde{\rho} - \tilde{\rho}\hat{a}^{\dagger}\hat{a}), \tag{3.2.20}$$

where we have defined

$$\tilde{\kappa} = 2\pi g(\omega_{\mathrm{c}})|\kappa(\omega_{\mathrm{c}})|^2. \tag{3.2.21}$$

3.3 Relaxation and dephasing processes

In order to "ground" the last result about the parameter $\tilde{\kappa}$ (just κ from here), let's think in our cavity, modeled as a quantum harmonic oscillator. In this context, κ is called as the *cavity decay rate*, and it will appear in the derivation of the equations of motion for the field observables, in particular for the mean or *expectation* values in time, controlling their rate of damping, like any classical oscillator theory.

This decay rate affects differently onto the diagonal or off-diagonal elements of the reduced density operator:

- The populations (diagonal terms) decay with the full rate κ.
- The coherences instead (off-diagonal terms) decay with half this rate $\kappa/2$.

This is clear by checking the following equations of motion and their respective solutions

$$\frac{\mathrm{d}}{\mathrm{dt}}\langle\hat{a}\rangle = -\left(\frac{\kappa}{2} + i\omega_{\mathrm{c}}\right)\langle\hat{a}\rangle, \quad \frac{\mathrm{d}}{\mathrm{dt}}\langle\hat{a}^{\dagger}\hat{a}\rangle = -\kappa\langle\hat{a}^{\dagger}\hat{a}\rangle, \tag{3.3.1}$$

$$\Rightarrow \langle\hat{a}(t)\rangle = -\langle\hat{a}(0)\rangle e^{-\frac{\kappa}{2}t}e^{-i\omega_{\mathrm{c}}t}, \quad \langle\hat{a}^{\dagger}\hat{a}(t)\rangle = \langle\hat{a}^{\dagger}\hat{a}(0)\rangle e^{-\kappa t}, \tag{3.3.2}$$

where we derive $\mathrm{d}\langle\hat{O}\rangle/\mathrm{dt} = \mathrm{tr}_{\mathrm{c}}[\hat{O}(\mathrm{d}\hat{\rho}/\mathrm{dt})]$ in the Schrodinger picture. The equation of motion for $\langle\hat{a}\rangle$ clearly represents a damped oscillation; its Fourier transform has the shape of a Lorentzian with frequency center at $\omega = \omega_{\mathrm{c}}$ and full width at half maximum (FWHM) $\delta\omega = \kappa$.

3.3.1 Dephasing time

The modelling of resonances as Lorentzians curves is ubiquitous in Spectroscopy, as it is directly connected with the lifetime of the excitations observed. In optical

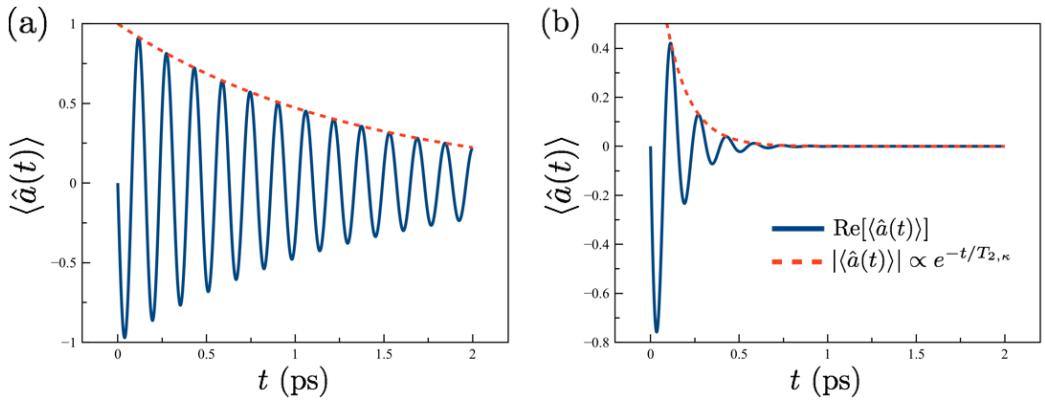

Figure 3.3.1: Simulations of two slow and fast decaying cavity coherences oscillating at frequency $\omega_c = 40$ THz, where the initial condition is fixed as a coherent state with $\langle \hat{a}(0) \rangle = -i$. (a) Slow decaying coherence at decay rate $\kappa = 1.5$ THz. (b) Fast decaying coherence at decay rate $\kappa = 15$ THz.

.

protocols able to measure the electric field $\hat{E} \propto (\hat{a}+\hat{a}^\dagger)$ with enough time resolution, it is important to have a characteristic time of the amplitude loss. The *dephasing time* is defined as $T_{2,\kappa} = 2/\kappa$, where if it is not explicitly mentioned, we will always assume that the numerical value of κ is written in absolute frequency units, instead of angular frequency[8]. For example, for $\kappa = 1$ THz, the dephasing time is nothing more than $T_{2,\kappa} = 2/\kappa = 2$ ps. In case contrary, if the notation used is $\kappa/2\pi = 1$ THz, then the dephasing time must to be calculated as $T_{2,\kappa} = 2/\kappa = 0.318$ ps. Obviously, this is an important *methodology issue* as everything else, and it must to be done with careful.

In Figure (3.3.1a-b) are shown two oscillating coherences with two different decay rates, the first one lower in one order of magnitude than the second one ($\kappa_1 = 0.1$ THz, $\kappa_2 = 1.5$ THz). It is clear that if the experimental time resolution is able to solve and fit the decay tale of this coherence, related with the near electric field of the cavity, then it can be deduced the dephasing time with the rule $|\langle \hat{a}(t) \rangle|/|\langle \hat{a}(0) \rangle| = \exp(-t/T_{2,\kappa})$.

[8] If the decay rate is obtained from the angular frequency width $\delta\omega$ of a Lorentzian, it must to be multiplied by 2π to compensate the units. This is the reason why one often encounters the notation $\kappa/2\pi$ in the scientific literature.

Chapter 4

Anharmonic Oscillators

4.1 Anharmonic oscillators in Nanophotonics

Nanophotonic devices are a class of miniaturized optical devices that are engineered to have dimensions on the order of nanometers. They are designed to manipulate and control light in different regions of the EM and matter spectrum, in very small confinement volumes V, as it is expressed in the electric and magnetic field amplitudes per photon, $\mathcal{E}_0$ and $\mathcal{B}_0$ respectively, derived in section 1.

The concept of anharmonicity arises from the non-equidistant energy levels structure present in those hybrid devices, allowing for nonlinear responses to the incoming electromagnetic fields, but also in the isolated interaction with the vacuum. For our particular interest, these intrinsic anharmonicities (for example, in molecular vibrations) or engineered ones (heterostructures, meta-materials, etc.) are important as they play a significant role in the nonlinear modulation of the phase of the electric near field we report in [3].

Our interest in the anharmonicity of quantum oscillators is the connection we show with nonlinear behaviour. This relationship has been reported in [2], where it is shown that anharmonicity and nonlinearity can be seen as nonclassical resources.

Generally speaking, the interaction between the cavity field and the material oscillators in a nonlinear media can lead to phenomena such as:

Self-Phase Modulation In cavity QED setups, where the cavity field intensity is relatively high, the nonlinearity in the energy levels of the emitters can

lead to interaction of a propagating wave with itself, in the form of self-phase modulation (SPM) of the cavity field [62].

Cross-Kerr Nonlinearity If we use the nonlinear media as a waveguide, the phase of a signal or pulse propagating in can be affected by other pulses propagating at the same time. As they will mutually influence each other, this phenomenon is called cross-phase modulation (XPM) [13]. This effect can be utilized for quantum information processing, such as quantum gate operations in quantum computing.

Nonlinear Dispersion The energy anharmonicity can also result in nonlinear dispersion, where the phase velocity of the cavity field is dependent on its intensity. This effect is relevant when considering the propagation of light pulses through cavity QED systems [15].

4.2 Sources of the anharmonicity

As it is pointed out in [45], the development of the experimental nonlinear optics field has an early referent in the works of John Kerr [38]. Surprisingly, one of their discoveries was the measurement of the refractive index change of collimated and spectrally filtered sunlight in response to a voltage applied to organic glass plates made of amber resin. Of course, in that time there were no notion of such thing as "discrete energy levels", and then the connection between nonlinearity and anharmonic spectra were not discovered yet. The development of Quantum Theory together with the fabrication of the first lasers allowed the use of higher optical intensities, required to address observable nonlinear effects, and obviously opened the way to the exploration and characterization of the nonlinear behaviour of matter when it is driven by electromagnetic fields, in particular connected to the anharmonicity present.

4.2.1 Organic materials

As a curiosity fact, despite the discovery of John Kerr with organic compounds, the use of organic matter to reach different regimes of light-matter coupling in cavity QED, taking advantage of its non-linear properties, is relatively recent [46]. When the organic media is used as a semiconductor crystal, the spectral properties of interest are related to charge carrier transitions of an specific molecular orbital

[7]. In these devices, nonlinear effects arises from the conjugation of self-localized exciton states, particularly when they are dressed with *polarons*, in conjugation with the delocalized molecular orbital in the meta-molecular structure (if it is a chain, for example, in dye J-aggregates [25]). Here, there is not a direct connection between the anharmonicity of an non-hybrid and separable degree of freedom, and nonlinear collective responses.

The scenario is different when we drive excitations related with intramolecular vibrational motion. The fact that vibrational potentials are highly nonlinear can be understood for two reasons:

- The bond strength between atoms in a molecule changes considerably in every stage of the oscillation movement. The restorative and repulsive "forces", with respect to the common nuclear coordinate, deviates from the harmonic behaviour, in the sense that are "weaker" for larger atomic separations, and are "stronger" for shorter distances, respectively.
- Any vibrational potential must to account for dissociation, strongly conditioning the energetic structure.

There are both experimental and theoretical works to characterize the complex anharmonic behaviour of diverse types of molecules, or directly using these data for semi-empirical works [20, 69, 24, 68, 3].

We have a prototypical example in the Morse potential for diatomic molecules [52]. The analytically derived energy levels, that scales as

$$E_\nu = -D_\mathrm{e} + a\hbar\sqrt{\frac{2D_\mathrm{e}}{\mu}}(\nu + 1/2) - \frac{a^2\hbar^2}{2D_\mathrm{e}\mu}(\nu + 1/2)^2,$$

where D_e is the dissociation energy, a is a calibration parameter of the Morse potential, and μ is a dimensionless reduced mass of the diatomic molecule, show decreasing steps in the energy climbing [29], correlating with the red-shifted progression we expect in any spectroscopic observable.

4.2.2 Inorganic semiconductor dipoles

In tailored semiconductor devices as quantum wells (QW's) or noninteracting arrange of quantum wells or Multi-quantum wells (MQW's), the confinement of

charge carriers, or *excitons* generate a finite division in the valence and conduction bands, called *subbands* (and *inter-subbands* in the case of MQW's), that are anharmonic in general, as it can be seen from the pedagogical example of an infinite quantum well (the "particle in a box") where

$$E_n = \frac{n^2\pi^2\hbar^2}{8mL^2}, \quad n = 1, 2, \dots$$

shows increased energy transitions in the ladder climbing and a blue-shifted progression with respect to the fundamental transition $\Delta_{21} = 3\pi^2\hbar^2/(2mL^2)$. As L is a "manufactured" parameter (the length of the well) and any real quantum well will not be "infinite", the specific shape of the subband structure can be *engineered*, depending on these geometrical specifications, as well as the type and proportions of semiconductors used in their design. The *fine-tuning* of all these parameters allows, in principle, for decreasing, increasing, or a mixture of both kind of energy steps, making them good candidates for anharmonic dipoles in cavity QED applications.

At this respect, the *state-of-the-art* in the design of these structures has reached an impressive degree of sophistication, as it is well exemplified in, for example, [22]. It is noteworthy to mention, also, that quantum wells has been used as nonlinear wave-guides and source of second or third harmonic generation due to their large high order susceptibilities [32, 65, 26, 43, 19, 75].

4.3 Quantum Model for anharmonic dipoles

We are in turn to introduce the model Hamiltonian that will be the center of all the theoretical predictions of this thesis.

The correspondence rule allows to connect the classical harmonic oscillator Hamiltonian with its quantum version, as reads

$$\mathcal{H}_{\text{harm}} = \frac{1}{2}\left(\frac{p^2}{2m} + m\omega_0^2 x^2\right) \longrightarrow \hat{\mathcal{H}}_{\text{harm}} = \hbar\omega_0\left(\hat{b}^\dagger\hat{b} + \frac{1}{2}\right). \tag{4.3.1}$$

where $x = q - q_{\text{e}}$ is the deviation with respect to the equilibrium coordinate q_{e}. In general, the quadratic potential $V(q - q_{\text{e}}) \propto (q - q_{\text{e}})^2$ is seen as the quadratic truncation of a Taylor series for a more general potential, and the consideration

of higher powers in the approximation is, for example, a regular approach in the study of the vibrational dynamics of molecules [69]. For an individual oscillator, it is generally expressed as

$$V(q-q_e)=\sum_k \alpha_k (q-q_e)^k. \tag{4.3.2}$$

It is expected that the inclusion of higher powers in the approximation for the Hamiltonian will break the harmonicity of the energy spectrum, as the only perfectly equidistant (and infinite) energy ladder comes from the harmonic potential. This fact expresses the intimate connection between anharmonicity and nonlinear behaviour in classical and also in quantum mechanics.

To give an example, the Morse potential [52], a well known model for studying diatomic molecules, expresses the idea that if the oscillation has enough energy, called dissociation energy D_e, the molecule will break (or "dissociate") into two separated atoms. It can be expanded in a Taylor series around $x=0$:

$$V_\mathrm{Morse}(x) = D_e\left(1-e^{-\sqrt{k_\mathrm{e}/2D_\mathrm{e}}x}\right)^2 \tag{4.3.3}$$

$$= \frac{k_\mathrm{e}}{2}x^2 - \frac{k_\mathrm{e}^{3/2}}{2\sqrt{2D_\mathrm{e}}}x^3 + \frac{7k_\mathrm{e}^2}{48D_\mathrm{e}}x^4 - \ldots, \tag{4.3.4}$$

where k_e the strength constant of the oscillator. Clearly, the quadratic truncation is not enough to derive the point when the molecule breaks. However, if we decide to explore small deviations from the harmonic regime, it is natural to characterization of cubic or quartic-related Hamiltonians[1]. From this analysis we know that the third power is only included if the nonlinear media is noncentrosymmetric, as they are the only ones that breaks parity symmetry in the coordinates of the oscillator.

For the present analysis and forward, we will focus only on excitations in a hypothetical centrosymmetric material although the model is able to include higher order truncations, as is already documented in the literature [56].

[1]This is explained in a nice analysis connecting cubic or quartic perturbations of a quadratic potential with second and third order susceptibilities in nonlinear media [6].

4.3.1 Quartic Kerr Hamiltonian

We will review the implications of including a quantized nonlinear potential to the harmonic Hamiltonian for a linear dipole of the form

$$\hat{V}_{\mathrm{NL}}(\hat{x}) = \tilde{U} : \hat{x}^4 : \; = \frac{\hbar^2 \tilde{U}}{4m^2\omega_0^2} : (\hat{b} + \hat{b}^\dagger)^4 : . \tag{4.3.5}$$

We express the potential in normal ordering as it is documented in [16]. We do not include the cubic contribution $\hat{x}^3$, that is included for materials that break the parity symmetry of their potential [2].

Trespassing the normal ordering to each of the elements of the previous expression, we have the following relationship

$$: (\hat{b} + \hat{b}^\dagger)^4 : \; \longrightarrow 6\hat{b}^\dagger\hat{b}^\dagger\hat{b}\hat{b} + 4\hat{b}^\dagger\hat{b}\hat{b}\hat{b} + 4\hat{b}^\dagger\hat{b}^\dagger\hat{b}^\dagger\hat{b} + \hat{b}\hat{b}\hat{b}\hat{b} + \hat{b}^\dagger\hat{b}^\dagger\hat{b}^\dagger\hat{b}^\dagger. \tag{4.3.6}$$

In the rotating frame of the fundamental frequency ω_0, the second and the following terms give rise to rapid oscillations that can be neglected if the dynamics is restricted to frequencies close to the fundamental one, as in the typical *rotating wave approximation* for composite quantum systems. Discarding all the terms except the first, the normally ordered anharmonic Hamiltonian can be expressed now as reads

$$\hat{H} = \hbar\omega_0\hat{b}^\dagger\hat{b} + \hbar U\hat{b}^\dagger\hat{b}^\dagger\hat{b}\hat{b}, \tag{4.3.7}$$

where $U = 3\hbar\tilde{U}/(2m^2\omega_0^2)$. This equation has an spectrum that is expressed as follows (setting $\hbar = 1$)

$$E_\nu = \langle\nu|\hat{H}|\nu\rangle = \nu\omega_0 + \nu(\nu-1)U, \tag{4.3.8}$$

$$\Rightarrow \Delta_{\nu,\nu-1} = \omega_0 + 2(\nu-1)U, \tag{4.3.9}$$

where $\Delta_{\nu,\nu-1} = E_\nu - E_{\nu-1}$ and the $|\nu\rangle$ are dipolar number states, which are eigenstates of this Hamiltonian. There are two cases we want to differentiate:

- When $\tilde{U}$ is positive, the spectrum has increasing energy transition steps. The fundamental frequency is $\Delta_{1,0} = \omega_0$ and the ground state is well defined

[2] Which is a typical choice for centrosymmetric molecular ensambles, for example. Besides, there are interesting effects related to this dependence, as for example the generation of second harmonics [75].

as $E_0 = 0$.

- If $\tilde{U}$ is negative, we have decreasing energy transitions. In particular, we noticed that this Hamiltonian is not bounded below, *e.g.* there is no ground state as

$$\lim_{\nu\to\infty} E_\nu \to -\infty. \tag{4.3.10}$$

To sort out this issue, we rewrite the Hamiltonian in a truncated form

$$\hat{H}' = \sum_{\nu=0}^{\nu_{\max}} E_\nu |\nu\rangle\langle\nu|, \quad \nu_{\max} = \left\lfloor \frac{\omega_0 + |U|}{2|U|} \right\rfloor. \tag{4.3.11}$$

where we use the floor function $\lfloor x \rfloor$ to specify that ν can only take integer values. We conclude that in order to describe quantum anharmonic oscillators with decreasing energy transitions, the Hamiltonian in Kerr form just allows a finite number of states $\nu_{\max} + 1$ in a consistent way.

4.3.2 Collective representation for N anharmonic dipoles

The generalization for N anharmonic dipoles from equation (4.3.7) is straightforward, assuming that they are not interacting between each other:

$$\hat{H}_N = \sum_{n=1}^{N} \left(\omega_n \hat{b}_n^\dagger \hat{b}_n - U_n \hat{b}_n^\dagger \hat{b}_n^\dagger \hat{b}_n \hat{b}_n \right). \tag{4.3.12}$$

Let's assume that all oscillators have the same frequency transition $\omega_n = \omega_0$ and anharmonicity parameter $U_n = U$. By using the following basis representation

$$\hat{B}_\alpha = \frac{1}{\sqrt{N}} \sum_{n=1}^{N} e^{\frac{i2\pi}{N}\alpha n} \hat{b}_n, \quad \hat{b}_m = \frac{1}{\sqrt{N}} \sum_{\beta=0}^{N-1} e^{-\frac{i2\pi}{N} m\beta} \hat{B}_\beta, \tag{4.3.13}$$

the Hamiltonian in Eq. (4.3.12) can be rewritten in the following form:

$$\hat{H}_N = \omega_0 \sum_{\alpha=0}^{N-1} \hat{B}_\alpha^\dagger \hat{B}_\alpha - \frac{U}{N} \sum_{\alpha,\beta,\eta=0}^{N-1} \hat{B}_\alpha^\dagger \hat{B}_\beta^\dagger \hat{B}_\eta \hat{B}_{\epsilon(\alpha,\beta,\eta)}. \tag{4.3.14}$$

where the index $\epsilon(\alpha,\beta,\eta)=\alpha+\beta-\eta(\mathrm{mod}N)$ of the last operator must to be calculated using *modular arithmetic* [3], modulo N.

This representation using indexes $0\leq\alpha\leq N-1$ distinguish between degrees of permutation invariance, from the most symmetric one ($\alpha=0$) to the less symmetric ($\alpha=N-1$). The eigenstates of the $\alpha=0$ operator, that we are going to call as the *bright* operator, are

$$|k_0\rangle=\frac{1}{\sqrt{N^k}}\sum_{\nu_1+\ldots+\nu_N=k}\sqrt{\frac{k!}{\nu_1!\cdot\ldots\cdot\nu_N!}}|\nu_1,\ldots,\nu_N\rangle, \tag{4.3.15}$$

and then $\hat{B}_0^\dagger\hat{B}_0|k_0\rangle=k|k_0\rangle$. In this notation, every $|\nu_n\rangle$ is an eigenstate of the $n-$number operator $\hat{b}_n^\dagger\hat{b}_n$. These states contains all the ways to put k excitations in the N oscillators, including the cases of having more than one per site, arranged in a permutation invariant form. From now on, Greek indexes will be used to distinguish *permutation* indexes like α from *site* indexes like n.

There is a best suited form of the Hamiltonian Eq. (4.3.14) that reads

$$\hat{H}_N=\left(\omega_0+U-\frac{U}{N}\sum_{\beta=0}^{N-1}\hat{B}_\beta^\dagger\hat{B}_\beta\right)\sum_{\alpha=0}^{N-1}\hat{B}_\alpha^\dagger\hat{B}_\alpha-\frac{U}{N}\sum_{\alpha,\beta\neq\eta=0}^{N-1}\hat{B}_\alpha^\dagger\hat{B}_{\epsilon(\alpha,\beta\eta)}\hat{B}_\beta^\dagger\hat{B}_\eta. \tag{4.3.16}$$

It shows explicitly that there is a frequency shift generated by the way that the bright and *dark* operators [4] are related to the population of the respective $\alpha-$ collective modes. Moreover, this shift does not depend on α so it is equal for all modes.

4.4 Equation of motion for a single anharmonic dipole

We are going to use an open quantum system approach in the Born-Markov approximation to study the dynamics of a single anharmonic dipole when the interaction with the environment, as for example the *vibrations* of the media

[3] https://en.wikipedia.org/w/index.php?title=Modular_arithmetic&oldid=1175659453. This also ensures that the result obeys $0\leq\epsilon\leq N-1$. To give examples, $\epsilon(0,0,1)=-1(\mathrm{mod}N)=N-1$ or $\epsilon(N-1,5,4)=N(\mathrm{mod}N)=0$.

[4] Let's call *dark* operators to those related with the remaining $N-1$ $\hat{B}_\alpha^\dagger\hat{B}_\alpha$ *number* operators.

structure due to thermal fluctuations, is weak and memory-less. In general, we expect that any effective dipole will dissipate energy in a similar way a cavity with confined modes is coupled to the free EM field. The Master equation for an anharmonic dipole ($N = 1$) in Kerr form is

$$\frac{\mathrm{d}}{\mathrm{dt}}\hat{\rho} = -i[\hat{\mathcal{H}}, \hat{\rho}] + \frac{\gamma}{2}(2\hat{b}\hat{\rho}\hat{b}^{\dagger} - \{\hat{b}^{\dagger}\hat{b}, \hat{\rho}\}). \tag{4.4.1}$$

where $\mathcal{L}_{\gamma}[\hat{\rho}] = (\gamma/2)(2\hat{b}\hat{\rho}\hat{b}^{\dagger} - \{\hat{b}^{\dagger}\hat{b}, \hat{\rho}\})$ is the dissipator term in Lindblad form for the dipole [5]. The equation for the dipole coherence expectation value $\langle\hat{b}\rangle$, using the Hamiltonian in Equation (4.3.14), is

$$\frac{\mathrm{d}}{\mathrm{dt}}\langle\hat{b}\rangle = -\left(\frac{\gamma}{2} + i\omega_0\right)\langle\hat{b}\rangle + i2U\langle\hat{b}^{\dagger}\hat{b}\hat{b}\rangle. \tag{4.4.2}$$

where we use the identity $\mathrm{d}\langle\hat{O}\rangle/\mathrm{dt} = \mathrm{tr}[\hat{O}\mathrm{d}\hat{\rho}/\mathrm{dt}]$. In this equation, the cubic term obtained present us two directions in order to solve the equation of motion:

- This equation will remain "linear" in the sense that we can calculate $\mathrm{d}\langle\hat{b}^{\dagger}\hat{b}\hat{b}\rangle/\mathrm{dt}$ for closing the system. However, as you can check, we are going to find higher order correlations, and finally an infinite system of equations. Then, this direction is non practical.
- The other way is to approximate higher order contributions like, for example, by separating degrees of correlations. A simple statement of this approach is, for example, to write $\langle\hat{b}^{\dagger}\hat{b}\hat{b}\rangle = \langle\hat{b}^{\dagger}\rangle\langle\hat{b}\rangle\langle\hat{b}\rangle +$ *correlations* avoided in the preceding product version.

We will see how to do this second option in the next subsection.

4.4.1 Truncation schemes

The *Cumulant expansion* give us a tool to handle this problem [66]. For up to quartic products of operators, that is the limit for our interest, it consists on using the following identities, (although it can be expanded to arbitrary number

[5] Remember that if this reservoir is in thermal equilibrium, in principle we expect not only dissipation but also incoherent pumping, the last depending on the thermal mean number with respect to the fundamental frequency of the system. However, at the frequencies of our interest, the mean number of excitations at room temperature is negligible (See Table 3.2.1).

of operators):

$$\langle \hat{A}\hat{B}\rangle = \langle \hat{A}\rangle\langle \hat{B}\rangle + \langle \hat{A}\hat{B}\rangle_{\mathrm{c}}, \tag{4.4.3}$$

$$\begin{aligned}\langle \hat{A}\hat{B}\hat{C}\rangle = &\langle \hat{A}\rangle\langle \hat{B}\rangle\langle \hat{C}\rangle + \langle \hat{A}\rangle\langle \hat{B}\hat{C}\rangle_{\mathrm{c}} + \langle \hat{B}\rangle\langle \hat{A}\hat{C}\rangle_{\mathrm{c}},\\ &+ \langle \hat{C}\rangle\langle \hat{A}\hat{B}\rangle_{\mathrm{c}} + \langle \hat{A}\hat{B}\hat{C}\rangle_{\mathrm{c}},\end{aligned} \tag{4.4.4}$$

$$\begin{aligned}\langle \hat{A}\hat{B}\hat{C}\hat{D}\rangle = &\langle \hat{A}\rangle\langle \hat{B}\rangle\langle \hat{C}\rangle\langle \hat{D}\rangle + \langle \hat{A}\rangle\langle \hat{B}\rangle\langle \hat{C}\hat{D}\rangle_{\mathrm{c}} + \langle \hat{A}\hat{B}\rangle_{\mathrm{c}}\langle \hat{C}\rangle\langle \hat{D}\rangle + \langle \hat{A}\hat{B}\rangle_{\mathrm{c}}\langle \hat{C}\hat{D}\rangle_{\mathrm{c}}\\ &+ \langle \hat{A}\rangle\langle \hat{C}\rangle\langle \hat{B}\hat{D}\rangle_{\mathrm{c}} + \langle \hat{B}\rangle\langle \hat{D}\rangle\langle \hat{A}\hat{C}\rangle_{\mathrm{c}} + \langle \hat{B}\hat{D}\rangle_{\mathrm{c}}\langle \hat{A}\hat{C}\rangle_{\mathrm{c}} + \langle \hat{A}\rangle\langle \hat{D}\rangle\langle \hat{B}\hat{C}\rangle_{\mathrm{c}}\\ &+ \langle \hat{B}\rangle\langle \hat{C}\rangle\langle \hat{A}\hat{D}\rangle_{\mathrm{c}} + \langle \hat{B}\hat{C}\rangle_{\mathrm{c}}\langle \hat{A}\hat{D}\rangle_{\mathrm{c}} + \langle \hat{A}\rangle\langle \hat{B}\hat{C}\hat{D}\rangle_{\mathrm{c}} + \langle \hat{B}\rangle\langle \hat{A}\hat{C}\hat{D}\rangle_{\mathrm{c}}\\ &\langle \hat{C}\rangle\langle \hat{A}\hat{B}\hat{D}\rangle_{\mathrm{c}} + \langle \hat{D}\rangle\langle \hat{A}\hat{B}\hat{C}\rangle_{\mathrm{c}}.\end{aligned} \tag{4.4.5}$$

where the expectation values $\langle \hat{A}\ldots\rangle_{\mathrm{c}}$ are the *cumulant terms*, encoding the correlations neglected in the approximations.

When all the quadratic or higher expectation values are truncated to first order, this is, by setting $\langle \hat{A}\hat{B}\rangle_{\mathrm{c}} \simeq 0$ and $\langle \hat{A}\hat{B}\hat{C}\rangle_{\mathrm{c}} \simeq 0$, we say that we are working with a *mean field model*.

The main results of this thesis are obtained from this mean field perspective, aiming to show that this first approximation captures the key features of the nonlinear problem, as we only need that the anharmonic of matter could be transferred coherently between oscillators. The second order approach goes beyond the scope of this work, however we include the explicit expressions for the second order equations in Appendix A1.

4.4.1.1 Mean Field approach

In this case, Equation (4.4.2) is approximated to

$$\frac{\mathrm{d}}{\mathrm{dt}}\langle \hat{b}\rangle = -\left(\frac{\gamma}{2} + i\omega_0\right)\langle \hat{b}\rangle + i2U\langle \hat{b}\rangle^*\langle \hat{b}\rangle\langle \hat{b}\rangle, \tag{4.4.6}$$

$$= -\left(\frac{\gamma}{2} + i\omega_0\right)\langle \hat{b}\rangle + i2U|\langle \hat{b}\rangle|^2\langle \hat{b}\rangle, \tag{4.4.7}$$

This result is known as the Stuart-Landau equation [64, 55]. As this oscillator is decoupled from the other ones, this equation is closed and it has analytical solution. To derive it, we use the polar representation $\langle \hat{b}\rangle = b(t)e^{i\phi(t)}$ with $b(t) = |\langle \hat{b}(t)\rangle|$.

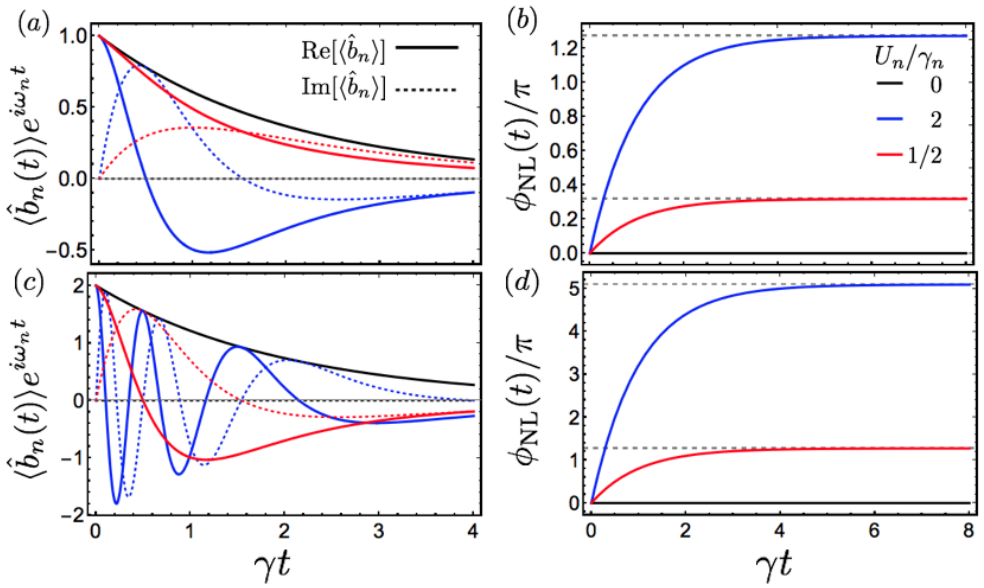

Figure 4.4.1: Mean field solutions for the real and imaginary parts of the complex anharmonic coherence in the rotating frame of the dipole $\langle\hat{b}\rangle e^{i\omega_0 t}$ and their respective phases in time for two initial cases: (a) and (b) correspond to set $\langle\hat{b}(0)\rangle = 1$, (c) and (d) correspond to set $\langle\hat{b}(0)\rangle = 2$. The colors in the four plots represents the harmonic case ($U/\gamma = 0$, black lines) and two anharmonic cases (high anharmonic ratio $U/\gamma = 2$, blue lines, and low anharmonic ratio $U/\gamma = 1/2$, red lines). Dashed lines in plots (b) and (d) indicates the steady phases $\phi_{\rm ss}$, in each case.

We have that

$$\frac{\mathrm{d}}{\mathrm{dt}}b(t) = -\frac{\gamma}{2}b(t) \Rightarrow b(t) = b_0 e^{-\frac{\gamma}{2}t}, \tag{4.4.8}$$

$$\frac{\mathrm{d}}{\mathrm{dt}}\phi(t) = -\omega_0 + 2U(b(t))^2 = -\omega_0 + 2Ub_0^2 e^{-\gamma t}. \tag{4.4.9}$$

where $b_0 = b(t=0) > 0$. The exact solution is

$$\langle\hat{b}(t)\rangle = b_0 \exp\left\{-\left(\frac{\gamma}{2} + i\omega_0\right)t + i\frac{2Ub_0^2}{\gamma}(1 - \exp(-\gamma t))\right\}. \tag{4.4.10}$$

The exponential times the imaginary number $i = \sqrt{-1}$ inside the expression above is a nonlinear time-dependent phase term of the complex coherence, that we label as reads

$$\phi_{\rm NL}(t) = \phi_{\rm ss}(1 - \exp(-\gamma t)), \tag{4.4.11}$$

stating a steady value that we call $\phi_{\rm ss} = 2Ub_0^2/\gamma$ that converges with twice the decay rate of the coherence amplitude $\propto \exp(-\gamma t/2)$. Notice also that the behaviour of this amplitude does not depend on U, only relying on its initial

condition.

In Figure (4.4.1) we show the evolution of this coherence with respect to three anharmonic cases ($U = 0$, $U = 2\gamma$ and $U = \gamma/2$) and two initial conditions considering, two different coherent states with $\alpha = 1$ or $\alpha = 2$.(and then $b_0 = 1$ or $b_0 = 2$). We plot the linear case ($U = 0$) with black lines, showing that the linear coherence does not change its initial complex phase, and then the dynamical phase for $U > 0$ is an exclusive result of the anharmonicity and nonlinearity present. Summarizing, the mean field approach contains the basic mechanism to generate nonlinear phase modulation when the anharmonic dipole is initialized at some quantum excited state, that increases with the amount of anharmonicity encoded with the anharmonic ratio U/γ.

Chapter 5

Results

5.1 Preliminary words

We already have the minimal theoretical background, presented in the previous chapters, to introduce the main results of this thesis. These results are divided in three parts:

- First, we derive an analytical theory of the Purcell effect [57] for a cavity QED filled with material dipoles, modeled as identical harmonic oscillators, in weak coupling regime. This *linear* quantum model proposal reproduces an experimental demonstration of the former [50], by using parameters obtained from independent experiments, which is already reported and validated in [68].

- Second (and the core of our work), we show that our model predicts important nonlinear effects when we consider the anharmonicity of the material infrared dipoles inside the cavity/resonator, in terms of a Kerr contribution, only in the material Hamiltonian [3]. Depending on the driving conditions, this system manifests a crossover from linear response – when it is driven by weakly enough sub-picosecond THz pulses– to an emerging nonlinear response when the dipoles reach higher excitation levels that are detuned from the fundamental transition.

- Finally, we show that the inclusion of dark states to the global dynamics, generate, in general, an enhancement or diminution of the nonlinear phase

modulation, compared with the analogous or reference homogeneous case.

These dark modes are completely decoupled under the mean field approach, *if* all dipoles share the same set of parameters. Then, the way to make them part of the dynamics is by introducing local inhomogeneities that break the perfect permutation symmetry of the collective system.

Our semi-empirical model considers realistic values for all the frequencies (and energies) involved, and the fundamental dissipation channels for both cavity and material dipoles are inserted as parameters in a Master equation in Lindblad form, that are extracted from the empty cavity and bulk spectroscopic measurements. The material dipoles considered in the first stage of validation are specific vibrations of a *carbonyl bond* present in an organic polymer of *Poly(methyl methacrylate)*, or *PMMA* for short [63, 44]. Those vibrations are treated as identical and non interacting harmonic oscillators weakly coupled to a subwavelenght metallic, mid-infrared resonator cavity mode, in complete resonance.

Regarding the second main results, the inclusion of an anharmonic spectrum just for the material dipoles make our model nonlinear, in the sense that the coupled light-matter system shares this property coherently and dynamically, producing a time evolution in the electric field and polarization of the media that can be clearly distinguished from a typical linear response, as we are going to show in the corpus of this section. For this results we consider an inorganic cavity, instead of the PMMA vibrations, made from a Multi-Quantum Well with input parameter values similar to those used in [48]. The advantage of these inorganic semiconductor structures is the possibility to confine a small number N of anharmonic dipoles, counteracting the dilution effects present in organic cavities that *screen* their anharmonic properties due to the size of the usual molecular ensembles used.

We notice that, independent of the fact that the cavity is modeled as a harmonic oscillator, the coupled system presents a nonlinear response, captured from the evanescent electric field of the nanostructure by using near-field probes or *nanotips* [28] [1]. This technology allows to achieve the sub-picosecond time resolution necessary to distinguish the nonlinear and transient time delays imprinted in the free induction decay of a signal, generated with highly enough incoming driving pulses, when compared with the linear frequency-locked electric signal expected

[1] This is actually the technology used in the measurement of the Purcell effect in organic cavities using PMMA, published in [68].

in weak driving conditions for the same setup.

We coined the term of *chirping effect*, as we derive an analytical instantaneous dipole frequency $\omega_0'(t)$ depending on the mean number of the dipoles excitations in time. This dependence generates a red-shift from the resonant fundamental transition, shared by the cavity and the dipoles, that grows with the mean population of the third energy level and is coherently transferred to the cavity field.

5.2 Purcell effect with pulsed mid-IR organic resonators

5.2.1 Light-matter linear model

As is usual in cavity QED, we model the empty cavity system as a single quantum harmonic oscillator of fundamental frequency ω_c.

The free Hamiltonian for the isolated single cavity mode then is (fixing $\hbar = 1$)

$$\hat{H}_c = \omega_c \hat{a}^\dagger \hat{a}. \tag{5.2.1}$$

where $\hat{a}$ is the annihilation operator of the cavity field and we omitted the vacuum energy as we are interested only in energy (or frequency) transitions [2].

For the dipolar oscillators, we model them as a collection of N bosonic quantum oscillators that, in order to describe linear response experiments in a weak driving condition $|F_d|/\kappa$, we approximate their confinement potential to a quadratic form around an nuclear equilibrium position. The Hamiltonian for one vibrational quantum oscillator reads

$$\hat{T}_n + \hat{V}_n(q) \approx \frac{\hat{p}_n^2}{2m} + \frac{1}{2} m\omega_v^2 \hat{q}_n = \hbar\omega_v(\hat{b}_n^\dagger \hat{b}_n + 1/2). \tag{5.2.2}$$

Here, $\hat{T}_n$ and $\hat{V}_n(q)$ are the kinetic and potential energy curve for the n-th dipole, the operator $\hat{b}_n$ is the annihilation operator of the anharmonic dipole n and ω_v is

[2] Although in general we expect a highly structured energy spectrum for a cavity, we can in principle design a particular geometry of a cavity with an appropriate *finesse* to isolate just one mode from the full spectrum and also to tune that mode to be in close or exact resonance with the material oscillators inside the resonator.

the fundamental frequency of the n-th oscillator.

The light-matter system Hamiltonian consists in a collection of N independent harmonic dipoles coupled to a single mode of a cavity QED with a coupling strength per site g_n. The Hamiltonian considering the free and interaction terms for the light-matter system, in the rotating wave approximation [3], is

$$\hat{\mathcal{H}}_N = \omega_c \hat{a}^\dagger \hat{a} + \sum_{n=1}^{N} \omega_n \hat{b}_n^\dagger \hat{b}_n + \sum_{n=1}^{N} g_n (\hat{a}^\dagger \hat{b}_n + \hat{b}_n^\dagger \hat{a}). \tag{5.2.3}$$

The role of relaxation and driving to the system is accounted in a Master Equation in the Lindblad form for the reduced density operator of the hybrid system $\hat{\rho}_S$ which reads

$$\frac{\mathrm{d}}{\mathrm{dt}}\hat{\rho}_S = -i[\hat{\mathcal{H}}_N + \hat{H}_d(t), \hat{\rho}_S] + \frac{\kappa}{2}\hat{\mathcal{L}}_{\hat{a}}[\hat{\rho}_S] + \sum_{n=1}^{N} \frac{\gamma_n}{2}\hat{\mathcal{L}}_{\hat{b}_n}[\hat{\rho}_S]. \tag{5.2.4}$$

Here, the $\hat{\mathcal{L}}$ operators are expressed in the usual Lindblad form:

$$\hat{\mathcal{L}}_{\hat{a}} = 2\hat{a}\hat{\rho}_S\hat{a}^\dagger - \hat{a}^\dagger\hat{a}\hat{\rho}_S - \hat{\rho}_S\hat{a}^\dagger\hat{a}, \tag{5.2.5}$$

$$\hat{\mathcal{L}}_{\hat{b}_n} = 2\hat{b}_n\hat{\rho}_S\hat{b}_n^\dagger - \hat{b}_n^\dagger\hat{b}_n\hat{\rho}_S - \hat{\rho}_S\hat{b}_n^\dagger\hat{b}_n. \tag{5.2.6}$$

For the cavity, the effect of dissipation due to population and coherence losses is accounted by the coupling with the infinite modes of the free electromagnetic field, in a perturbative approach allowing to encode the environment influence with the cavity decay rate parameter κ [4]. For the dipoles instead, the main dissipation channels are non-radiative, related with phonons generated in a disordered media at thermal equilibrium, that in general are local and here we parameterize with the decay rates γ_n.

Also, we introduced the time dependent driving Hamiltonian $\hat{H}_d(t)$, which is simply a classical coherent driving field incoming to the resonator structure. Its

[3] Or RWA, for short. This approximation in general is broken for strong, ultra-strong coupling, or other more complex regimes [51, 18].

Here, however, we are only interested in a weak coupling scenario, justifying our approach.

[4] This parameter is obtained from the spectroscopic signatures of the empty cavity in reflection or transmission experiments by taking the *Full Width and Half Maximum* FWHM of the corresponding resonance peak, which is generally fitted with a Lorentzian function.

explicit form reads

$$\hat{H}_d(t) = F_d(t)(\hat{a}e^{i\omega_d t} + \hat{a}^\dagger e^{-i\omega_\mathrm{d} t}), \tag{5.2.7}$$

where $F_d(t) = F_0\varphi(t)$, $\varphi(t)$ is the envelope of the driving pulse, F_0 is related to the incoming photon flux $\Phi_{\mathrm{flux}} \propto |F_0|^2$, and ω_d is the carrier frequency of the laser.

5.2.2 Homogeneous ansatz

In the ideal case of identical dipole oscillators, equally coupled to the cavity field, the expression of the Hamiltonian is simplified:

$$\hat{\mathcal{H}}_N = \omega_c \hat{a}^\dagger \hat{a} + \omega_0 \sum_{n=1}^{N} \hat{b}_n^\dagger \hat{b}_n + g \sum_{n=1}^{N} (\hat{a}^\dagger \hat{b}_n + \hat{b}_n^\dagger \hat{a}). \tag{5.2.8}$$

By changing to the collective dipolar basis, the Hamiltonian will look like

$$\hat{\mathcal{H}}_N = \omega_c \hat{a}^\dagger \hat{a} + \omega_0 \sum_{\alpha=0}^{N-1} \hat{B}_\alpha^\dagger \hat{B}_\alpha + \sqrt{N} g (\hat{a}^\dagger \hat{B}_0 + \hat{B}_0^\dagger \hat{a}), \tag{5.2.9}$$

$$\cong \omega_c \hat{a}^\dagger \hat{a} + \omega_0 \hat{B}_0^\dagger \hat{B}_0 + \sqrt{N} g (\hat{a}^\dagger \hat{B}_0 + \hat{B}_0^\dagger \hat{a}), \tag{5.2.10}$$

where the last congruence relationship is exactly valid when all the dark states are not initialized $\langle \hat{B}_{\alpha\neq 0} \rangle = 0$, as the EM field only couples with the bright state $\langle \hat{B}_0 \rangle$.

Moreover, the Lindblad term related to dipole losses, when we fix $\gamma_n = \gamma$ for all the N dipoles, can be rewritten as reads

$$\frac{\gamma}{2} \sum_{n=1}^{N} \hat{\mathcal{L}}_{\hat{b}_n}[\hat{\rho}_S] = \frac{\gamma}{2} \sum_{\alpha=0}^{N-1} \left(2\hat{B}_\alpha \hat{\rho}_S \hat{B}_\alpha^\dagger - \hat{B}_\alpha^\dagger \hat{B}_\alpha \hat{\rho}_S - \hat{\rho}_S \hat{B}_\alpha^\dagger \hat{B}_\alpha \right). \tag{5.2.11}$$

From all these equations it is crystal clear that the dark modes $\alpha \neq 0$ are completely decoupled, as for the dipole approximation considered ($g_n = g$ for all dipoles), the cavity field will couple only with the bright mode $\alpha = 0$. Then, it is justified the use of the following reduced version of the Hamiltonian:

$$\hat{\mathcal{H}}_N = \omega_c \hat{a}^\dagger \hat{a} + \omega_0 \hat{B}_0^\dagger \hat{B}_0 + \sqrt{N} g (\hat{a}^\dagger \hat{B}_0 + \hat{B}_0^\dagger \hat{a}). \tag{5.2.12}$$

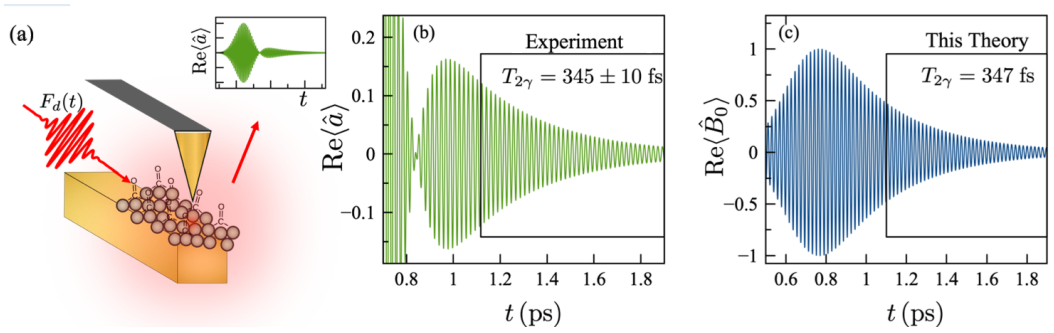

Figure 5.2.1: Vibrational Purcell effect. (a) Field detection scheme for the PMMA-coated nanowire with the nanoscale local probing at the wire terminal, using the following parameters $\{\omega_{\rm v}, \kappa/2\pi, \gamma/2\pi, \sqrt{N}g\} = \{51.9, 15.6, 0.510, 1.24\}$ THz. (b) Pulse-driven resonator field $\mathrm{Re}[\langle\hat{a}(t)\rangle]$ measured in Ref. [50] for a resonant molecular vibration–antenna system ($\omega_{\rm v} = \omega_{\rm c}$). The measured lifetime of the FID signal is $T_{2,\tilde{\gamma}} = 345 \pm 10$ fs (boxed region, inset). (c) Simulated collective molecular coherence $\mathrm{Re}[\langle\hat{B}_0(t)\rangle]$ under equivalent conditions as in experiments with dephasing time $T_{2,\tilde{\gamma}} = 347$ fs for $\sqrt{N}g = 1.24$ THz, where the free space dephasing time is $T_{2,\gamma} = 624$ fs. We predict an enhanced vibrational decay rate of $\tilde{\gamma}/2\pi = 0.917$ THz.

and the following shape of the Master equation

$$\frac{\mathrm{d}}{\mathrm{dt}}\hat{\rho}_S = -i[\hat{\mathcal{H}}_N + \hat{H}_d(t), \hat{\rho}_S] + \frac{\kappa}{2}\hat{\mathcal{L}}_{\hat{a}}[\hat{\rho}_S] + \frac{\gamma}{2}\hat{\mathcal{L}}_{\hat{B}_0}[\hat{\rho}_S], \tag{5.2.13}$$

where $\hat{\mathcal{L}}_{\hat{B}_0}[\hat{\rho}_S] = 2\hat{B}_0\hat{\rho}_S\hat{B}_0^\dagger - \hat{B}_0^\dagger\hat{B}_0\hat{\rho}_S - \hat{\rho}_S\hat{B}_0^\dagger\hat{B}_0$.

5.2.3 Purcell factors

We apply our formalism to reproduce the field detection done in a PMMA-coated nanowire captured with a nanoprobe, as it is shown schematically in Figure (5.2.1-a). The cavity was driven with a Gaussian pulse with carrier frequency $\omega_{\rm d} = 51.9$ THz in resonance with the coupled cavity-vibrational system, and the temporal center and duration where $t_0 = 600$ fs and $T = 155$ fs, respectively. We neglected the tip field influence into the cavity plus vibrations system, as typically these nanodevices are broadband compared with the probed device and their effect can be neglected depending on the lifetime relations between subsystems [5].

The system of equations for the homogeneous light-matter system coherences,

[5] A more detailed theoretical exploration of the inclusion of the tip dynamics is done in [68], showing coherent tip-induced phase-space rotations depending on the horizontal position of the tip, and a crossover from weak to strong coupling by the tuning of the vertical position of the tip, with respect to the antenna layer.

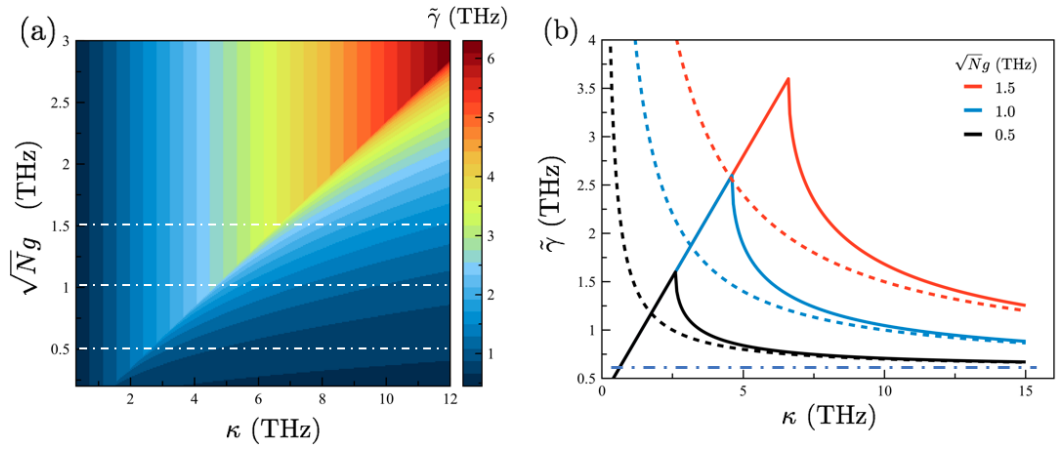

Figure 5.2.2: Purcell-enhanced dipole decay rate $\tilde{\gamma}$ with respect to $\sqrt{N}g$ and κ for fixed free-space dipole decay $\gamma = 0.6$ THz. (a) Color plot showing a diagonal threshold between the strong coupling hybridized light-matter decay rate (upper left) and the weak coupling dipole decay rate (lower right). (b) Comparison between the exact value of $\tilde{\gamma}$ (thick lines) and the adiabatically obtained dipole decay rate (dashed lines) for three different values of the collective coupling $\sqrt{N}g$. These three cases correspond to the three dashed white lines in plot (a). The fixed decay rate γ is represented with a dot-dashed blue line.

consisting in the cavity single mode plus N vibrational excitations, is

$$\frac{\mathrm{d}}{\mathrm{dt}}\langle\hat{a}\rangle = -\left(\frac{\kappa}{2} + i\omega_{\mathrm{c}}\right)\langle\hat{a}\rangle - i\sqrt{N}g\langle\hat{B}_0\rangle - i\tilde{F}_{\mathrm{d}}(t), \tag{5.2.14}$$

$$\frac{\mathrm{d}}{\mathrm{dt}}\langle\hat{B}_0\rangle = -\left(\frac{\gamma}{2} + i\omega_0\right)\langle\hat{B}_0\rangle - i\sqrt{N}g\langle\hat{a}\rangle, \tag{5.2.15}$$

where $\tilde{F}_{\mathrm{d}}(t) = F_0 e^{-i\omega_{\mathrm{d}}t}\varphi(t)$. This is exactly solved by applying the Fourier Transform to the complex coherences of the system:

$$\langle\hat{a}(\omega)\rangle = \frac{1}{\sqrt{2\pi}}\int_{-\infty}^{\infty}\langle\hat{a}(t)\rangle e^{i\omega t}\mathrm{d}t, \quad \langle\hat{B}_0(\omega)\rangle = \frac{1}{\sqrt{2\pi}}\int_{-\infty}^{\infty}\langle\hat{B}_0(t)\rangle e^{i\omega t}\mathrm{d}t,$$

and formulating the corresponding algebraic system from Eqs. (5.2.14-5.2.15). In the resonant condition $\omega_{\mathrm{c}} = \omega_{\mathrm{d}} = \omega_0$, fixing $\kappa > \gamma$ for a bad cavity, and by considering a weak coupling case stated by the relation

$$|\kappa - \gamma|/2 > 2\sqrt{N}g, \tag{5.2.16}$$

we find that the response of the oscillators present the modified decay rates as

reads

$$\tilde{\kappa} = \frac{\kappa+\gamma}{2} + \Gamma_g = \frac{\kappa}{2}\left(1 + \frac{\gamma + 2\Gamma_g}{\kappa}\right), \tag{5.2.17}$$

$$\tilde{\gamma} = \frac{\kappa+\gamma}{2} - \Gamma_g = \frac{\gamma}{2}\left(1 + \frac{\kappa - 2\Gamma_g}{\gamma}\right), \tag{5.2.18}$$

where we define $\Gamma_g = \sqrt{\left(\frac{\kappa-\gamma}{2}\right)^2 - 4Ng^2}$.

Notice that the condition Eq. (5.2.16) delimits a threshold between weak coupling –characterized by a decay renormalization for both oscillators– and strong coupling, showing the hybridization into a common decay rate, equal to the mean value $(\gamma+\kappa)/2$ [6].

Complementary to these results, we find also a good approximation for the renormalization of the material decay rate in the bad cavity regime where $\kappa \gg \gamma$. Let's define the slowly varying coherences, in exact resonance, as $\tilde{a}(t) = \langle \hat{a}(t) \rangle e^{i\omega_0 t}$ and $\tilde{B}_0(t) = \langle \hat{B}_0(t) \rangle e^{i\omega_0 t}$. Now, the system of equation is rewritten as

$$\frac{\mathrm{d}}{\mathrm{dt}}\tilde{a} = -\frac{\kappa}{2}\tilde{a} - i\sqrt{N}g\tilde{B}_0 - iF_0\varphi(t), \tag{5.2.19}$$

$$\frac{\mathrm{d}}{\mathrm{dt}}\tilde{B}_0 = -\frac{\gamma}{2}\tilde{B}_0 - i\sqrt{N}g\tilde{a}, \tag{5.2.20}$$

We make the adiabatic approximation for the free induction decay ($\varphi(t) \approx 0$) by imposing $\mathrm{d}\tilde{a}/\mathrm{dt} = 0$. We obtain a renormalized equation of motion for the dipole coherence by replacing $\tilde{a}_{\mathrm{ss}} = -i(2\sqrt{N}g/\kappa)\tilde{B}_0$ in the equation for $\tilde{B}_0$, that reads

$$\frac{\mathrm{d}}{\mathrm{dt}}\tilde{B}_0 \approx -\frac{\gamma}{2}\left(1 + \frac{4Ng^2}{\kappa\gamma}\right)\tilde{B}_0 = -\frac{\gamma P_{\mathrm{dip}}}{2}\tilde{B}_0 \tag{5.2.21}$$

In this manner we obtain an approximation for the Purcell factor $P_{\mathrm{dip}} = 1 + 4Ng^2/(\kappa\gamma)$ containing the *cooperativity* parameter $4Ng^2/(\kappa\gamma)$ [68]. As the decay offset is high, in principle it is expected that the long lived dipole excitation transfers coherently into the free induction decay of the cavity near field in the form of beatings, from which the enhanced decay rate $\tilde{\gamma}$, and the corresponding shorter dephasing time $T_{2,\tilde{\gamma}} = 2/\tilde{\gamma}$, can be fitted from the envelope of the electric field amplitude. The comparison between the experimental fit and the reproduction

[6] Notice also that if the inequality does not hold, the factor Γ_g becomes an imaginary number. It can be proven that this imaginary number contributes to the frequency splitting in the spectrum of the coupled oscillator, that is the signature of the strong coupling regime.

of this result by using our simulation is showed in Figures (5.2.1a-b), as it was done successfully in [50, 68].

Furthermore, we show in Figure (5.2.2) a color plot of the Purcell-enhanced dipole decay rate $\tilde{\gamma} > \gamma$ for the fixed free-space value $\gamma/2\pi = 0.6$ THz with respect to different choices of the collective light-matter coupling $\sqrt{N}g$ and cavity decay rate κ, and considering values in the range of few THz, for applications in the mid-infrared. Also, in figure (b) we compare the renormalized dipole decay rate Eq. (5.2.18) -plotted with solid lines– with respect to the adiabatic approximation of the Purcell-enhanced decay rate Eq. (5.2.21) –with dashed lines– showing good agreement for sufficiently high cavity decay rates $\kappa \gtrsim 15\gamma$. The peaks present in the right panel, and the subsequent straight lines for lower κ, correspond to the cases where the combination of parameters goes beyond the weak coupling regime, where we expect generation of *polaritons*. These polaritons are hybrid, non-separable excitations, that presents a decay rate equal to the mean value of the free-space decay rates from both cavity and material dipoles, as it can be seen also from the left panel (a), in the upper left part of the diagonal crossover line.

5.3 Nonlinear dynamics for identical dipoles

The previous linear response theory relies in a *weak* driving condition parameterized with $|F_{\mathrm{d}}|/\kappa \ll 1$. This condition conjugates with the chosen time duration $T \sim 150$ fs of the driving pulses, that is much shorter than the characteristic cavity decay time $1/\kappa \ll T$. For a detailed argument about the mean excitation numbers obtained form the theory, please visit Appendix A2. Our case scenario $\kappa/\omega_{\mathrm{c}} \sim 0.3$ is representative of open nanoresonators in the THz as the reported in [50], translating in photon lifetimes of the order of a few femtoseconds. Controlling all these conditions ensures that the vibrational ladder climbing do not going beyond the desired level over a pulse duration. Obviously, for the harmonic approximation, this limit is the first excited state with $\nu = 1$.

If it is also the case that the second or higher excited energy levels are detuned with respect to the fundamental transition, accessing them necessarily will break the harmonic approximation.

The intrinsic anharmonicity of vibrational dipoles typically varies in the range of 0.3–1.2 THz for polyatomic molecules [20, 24], and they manifest as smaller

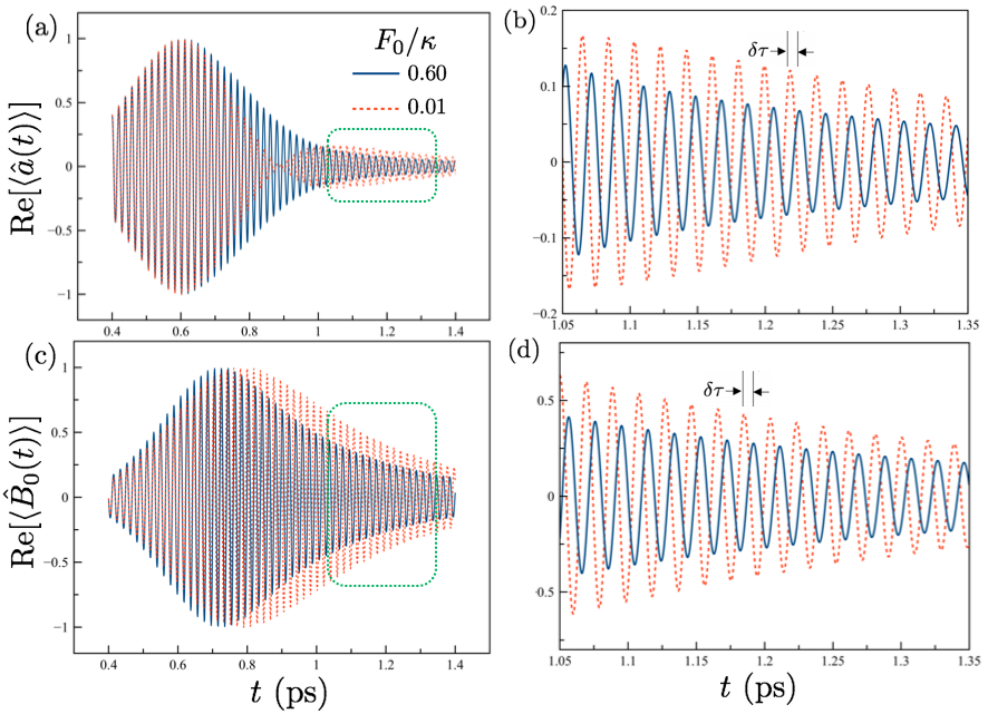

Figure 5.3.1: Evolution of the real part of the system coherences for $N = 2$ anharmonic vibrations ($U = 0.6$ THz) subject to a single 0.155 ps pulse centered at 0.6 ps with driving strength parameters $F_0/\kappa = 0.6$ (blue solid line) and $F_0/\kappa = 0.01$ (orange dashed line). The set of parameters chosen was similar to the used in Figure 5.2.1. The delay $\delta\tau$ between the weak and strong field responses is highlighted. (a) Evolution of the cavity coherence $\mathrm{Re}[\langle\hat{a}\rangle]$. The green dashed box is shown magnified in (b) to appreciate the FID signal after the pulse is over. (b) Evolution of the dipole collective coherence $\mathrm{Re}[\langle\hat{B}_0\rangle]$. The green dashed box is shown magnified in (d) to appreciate the FID signal after the pulse is over.

energy spacing between subsequent energy levels, compared with the fundamental transition.

We will show that our model is able to treat organic cavities as the PMMA/resonator mentioned in the previous chapter, and also inorganic heterostructures as multi-quantum wells in cavities as anharmonic dipoles. These devices are designed to obtain specific spectroscopic features and, where the number and shape of the charge carrier subbands are built for the requirements of the consumer. The advantages with respect to organic cavities is clear when we notice that we can putt a small number N of quantum wells inside a single MQW, and also because they can be manufactured with higher anharmonicities ($U_n \sim$ 3–9 THz) than the previously reported organic molecules [48].

5.3.1 Antenna-Vibrations

The Born-Oppenheimer potential is frequently used to describe the potential energy of chemical bonds fluctuating around an equilibrium bond length q_{e}, that reads

$$V(q-q_{\mathrm{e}})=\sum_{k}\alpha_{k}(q-q_{\mathrm{e}})^{k}. \tag{5.3.1}$$

Minimal models using up to quartic nonlinearities ($k_{\mathrm{max}}=4$) for parity symmetric potentials (for which the $k=3$ term is neglected) have been used to study nonlinear vibrational spectroscopy [56, 69, 59], and in particular in the context of vibration strong coupling in Fabry-Perot resonators [17].

An important feature we want to capture from these nonlinear models is the reduction of the energy spacing between subsequent energy levels. This difference is present in the energy gap Δ_{21} between $\nu=1$ and $\nu=2$ levels, compared with the fundamental transition at frequency $\omega_{\mathrm{v}}>\Delta_{21}/\hbar$.

We use the harmonic oscillator operators to write the vibrational potential in Kerr form

$$\hat{T}_{n}+\hat{V}_{n}\approx\omega_{\mathrm{v}}\hat{b}_{n}^{\dagger}\hat{b}_{n}-U\hat{b}_{n}^{\dagger}\hat{b}_{n}^{\dagger}\hat{b}_{n}\hat{b}_{n}, \tag{5.3.2}$$

where $U=|\Delta_{21}|/2$.

The light-matter dynamics is simulated by solving the quantum master equation in Eq. (5.2.13) together with the minimal anharmonic Hamiltonian in Eq. (5.3.2) for N identical molecules. The mean field equations of motion for the cavity and collective vibrational coherences read as

$$\frac{\mathrm{d}}{\mathrm{dt}}\langle\hat{a}\rangle=-\left(\frac{\kappa}{2}+i\omega_{\mathrm{c}}\right)\langle\hat{a}\rangle-i\sqrt{N}g\langle\hat{B}_{0}\rangle-iF_{0}\varphi(t)e^{-i\omega_{\mathrm{d}}t}, \tag{5.3.3}$$

$$\frac{\mathrm{d}}{\mathrm{dt}}\langle\hat{B}_{0}\rangle=-\left(\frac{\gamma}{2}+i\omega_{\mathrm{v}}'(t)\right)\langle\hat{B}_{0}\rangle-i\sqrt{N}g\langle\hat{a}\rangle \tag{5.3.4}$$

where we have defined the instantaneous frequency

$$\omega_{\mathrm{v}}'(t)=\omega_{\mathrm{v}}-\frac{2U}{N}|\langle\hat{B}_{0}(t)\rangle|^{2}, \tag{5.3.5}$$

and we have chosen the single-molecule Rabi frequency g, the local vibrational relaxation rate γ, and the cavity decay rate κ to be the same as in the linear response theory developed in the previous section.

5.3.1.1 Anharmonic Time Delay Effect for Strong Pulsed Excitation

We can simulate the coupled light-matter dynamics of anharmonic vibrations coupled to an infrared resonator, by solving the system of equations (5.3.3-5.3.4) for a system of N molecules. The single-molecule Rabi frequency g, the local vibrational relaxation rate γ, and the cavity decay rate κ, are set to be the same as in Fig. (5.2.1), and then the system is also in weak coupling. For a driving strength parameter $F_0/\kappa \gtrsim 0.6$, we numerically compute the evolution of the collective coherence $\langle \hat{B}_0(t) \rangle$ by integrating the equations of motion in the mean field approach.

In Fig. 5.3.1 we plot the evolution of $\mathrm{Re}\langle \hat{a}(t) \rangle$ and $\mathrm{Re}\langle \hat{B}_0(t) \rangle$ for $N = 2$ and $F_0/\kappa = 0.6$, obtained as described above (solid line). We also show the response of a coupled system driven by a pulse that has the same normalized temporal profile ($t_0 = 600$ fs, $T = 155$ fs), but is much weaker ($F_0/\kappa = 0.01$, linear response). Resonant coupling and driving is assumed ($\omega_\mathrm{v} = \omega_\mathrm{a} = \omega_\mathrm{d}$) and the single molecule nonlinearity parameter is $U = 0.6$ THz. The strongly driven signal develops a time delay $\delta\tau$ of a fraction of a cycle relative to weak driving (boxed green rectangles in (a) and (c), magnified in (b) and (d)). This delay builds up gradually while the pulse is on and remains relatively stable after the pulse is over. The vibrational decay time ($T_{2,\gamma}$) does not depend on the pulse strength[7].

We plot in Figure 5.3.2 how anharmonic time delays are generated in the FID signal when we compare them with their analogous linear response cases, when the coupled system is driven by a finite Gaussian pulse as the one shown in dotted grey lines, highlighting the part of the pulse profile with higher intensity, around $t_0 - T < t < t_0 + T$. We overlap the time delays calculated numerically for the material coherence ($\delta\tau^{(B_0)}(t)/T_0$, dashed lines) and cavity coherence ($\delta\tau^{(a)}(t)/T_0$, overlapped circles). What our numerical results show is that, even when the initial evolution of these delays are not equal for both oscillators, they coincide for long times after the pulse is over[8].

[7] It is noteworthy to mention that in a linear FID in weak coupling, due to the decay offset present ($\kappa/\gamma \approx 30.6$) we expect *beatings* in the cavity coherence due to the coherent signal transfer from the material dipoles, as we can see from Fig. 5.3.1-(a) for the weak driving condition $F_0/\kappa = 0.01$. However, this behaviour is not present in the nonlinear case ($F_0/\kappa = 0.60$).

[8] This will be of main importance as will allow us to develop the adiabatic elimination procedure, in order to obtain analytical equations for this time delays, and correlated phase shifts that we are going to develop further.

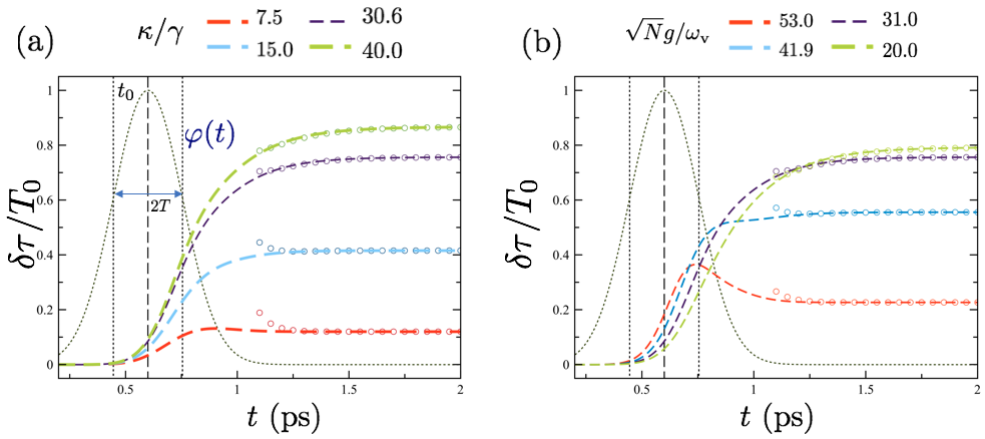

Figure 5.3.2: Adimensional time delays over the fundamental period $T_0 = 2\pi/\omega_v$, with respect to different set of parameters, but fixing $\{\omega_v, \kappa/2\pi\} = \{51.9, 15.6\}$ THz. (a) Time delay ratio calculated as the time difference between peaks and dips of the material collective coherence $(\delta\tau^{(B_0)}(t)/T_0$, dashed lines) and cavity coherence $(\delta\tau^{(a)}(t)/T_0$, empty circles) for different decay ratios κ/γ, keeping $\kappa/2\pi = 15.6$ THz fixed. The grey dotted bell curves correspond to the Gaussian pulse envelope $\varphi(t)$ with temporal width T,when the center of the pulse $t_0 = 0.6$ ps and pulse width $T = 0.155$ ps are marked with vertical dashed lines. The time delays derived from the cavity coherence are plotted from $t = 1.1$ ps as they just stabilize after the appearance of beatings around ≈ 0.85 (ps). (b) Time delay ratio calculated as the time difference between peaks and dips of the material collective coherence (dashed lines) and cavity coherence (empty circles) for different coupling ratio $\sqrt{N}g/\omega_v$, keeping $\sqrt{N}g/2\pi = 1.24$ THz fixed.

Figure 5.3.2-(a) shows the evolution of $\delta\tau$ for four scenarios, fixing the value of $\kappa/2\pi = 15.6$ THz. For long dipole lifetimes compared with the cavity ($\kappa = 40\gamma$), i.e., narrow–band vibrational dipole response, the time delay of the FID signal remains stable after the driving pulse is over, becoming more and more higher for sharper dipole bandwidths. On the contrary, when ($\kappa = 7.5\gamma$) the time delay lowers from a maximum value after the pulse ends. The system thus requires long dipole dephasing times to imprint a stationary time delay in the near field once the driving pulse is turned off.

We also include the case for variations in the collective light-matter coupling $\sqrt{N}g$. Figure 5.3.2-(b) have for four scenarios. For high light matter coupling respect to the fundamental frequency ($\sqrt{N}g/\omega_v = 53$), the time delay of the FID signal has a similar behaviour than the lower decay ratio, this is, after reaching a maximum, it stabilizes in a lower value. On the contrary, when ($\sqrt{N}g/\omega_v = 20$), the time delay shown stabilizes monotonically to a maximum steady value. All these results suggest that in order to achieve higher time delays *efficiently*, it is necessary to be immersed in weak coupling as deep as it could be.

This consideration can be correlated with the results of the Purcell enhancement

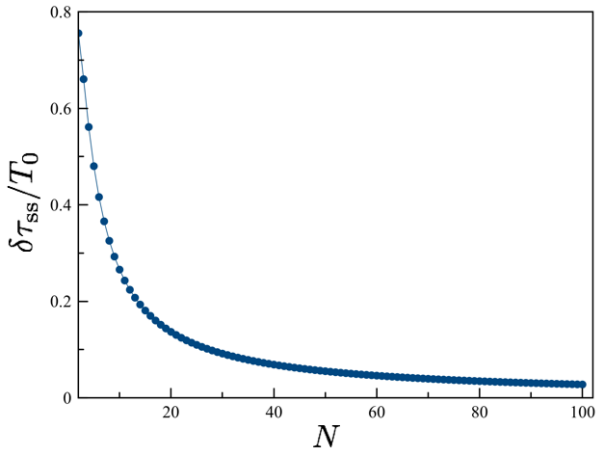

Figure 5.3.3: Stationary time delay, calculated at $t = 2.5$ (ps), with respect to N, and considering the set of semi-empirical parameters $\{\omega_v, \kappa/2\pi, \gamma/2\pi, \sqrt{2}g\} = \{51.9, 15.6, 0.510, 1.24\}$ THz. As is clearly noticed, the dilution effect for larger N makes any nonlinear effect, as this time delay, negligible.

in Figure 5.2.2. The effective vibrational decay rate decreases for lower coupling strengths g and higher cavity decay rate κ. This ratifies that it is required long dipole dephasing times, in this case the enhanced dephasing time, to imprint a stationary time delay in the near field after the pulse is off.

Although we predict appreciable time delays, for feasible optical and material bandwidths, and single coupling strength, the values chosen for N are just a "proof of principle": realistic values for PMMA are reported to be close to $N \sim 10^3$ [50]. In Figure 5.3.3 we capture this dilution effect in the stationary value of $\delta\tau_{ss}/T_0$ for increasing number of dipoles N in the ensemble. For $N \sim 10^2$, this effect is almost negligible for the set the parameters chosen.

More realistic candidates for the set of parameters used are MQW's [74], as these structures can accommodate a smaller number of effective dipoles ($N = 26$ in [48]) and also presents higher anharmonicities, that can be also engineered depending on the experimental requirements, allowing for much more flexibility than organic infrared cavities like the referenced here.

In Figure 5.3.4 we show an schematic picture of a MQW in an open infrared nanocavity, with incoming and outcoming fields interacting directly just with the antenna, on the top layer of the nanodevice. In this way, the driven pulses do not interact with the dipoles inside, but they drive the near field between the top antenna layer and the bottom surface. As the wavelengths we are interested,

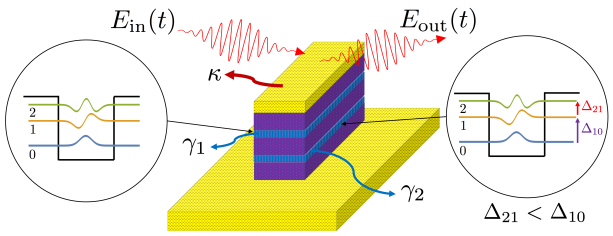

Figure 5.3.4: Schematic picture of a MQW in a driven open infrared nanocavity formed by two quantum wells with fundamental frequency $\omega_0 = \Delta_{10}$. The $0 \to 1$ and $1 \to 2$ transitions are coupled to the near-field of an open nanocavity with frequency ω_c by an incoming laser pulse E_{in}. The photons that leak out the nanocavity on sub-picosecond time scales at rate κ generate the free-induction decay (FID) signal encoded in the outcoming field E_{out}. .

in the order of ~ 1.2 μm are broader than the dimensions of the quantum wells widths (around ~ 15 nm [48]), the dipolar approximation is well justified, allowing for a symmetrical collective coupling with the EM near field.

5.3.2 Antenna-MQW's

As we mentioned before, MQW's in resonator or cavity setups allows for more flexibility in the choose of optical and material parameters, as well as sufficient small N effective dipoles to counteract the dilution effect present in organic cavity QED.

In Figure 5.3.5 we show the effect on different anharmonicity and driving conditions for a open mid-infrared nanoresonator (the "cavity") containing a hypothetical MQW with two identical quantum wells inside ($N = 2$), which is much more feasible on modern nanophotonics implementations [49].

As we mentioned before, the Kerr nonlinearity of our anharmonic model generates an effective dipole *chirping effect*, with instantaneous frequency $\omega_0'(t)$.

This is red shifted from the fundamental resonance by an amount proportional to the bright mode occupation $|\langle \hat{B}_0(t) \rangle|^2$, in our mean field approach. The nonlinearity is proportional to the anharmonicity parameter U and is small for large N [68]. The transient red shift occurs while the system is driven by the laser pulse, which populates $\hat{B}_0(t)$, and is thus proportional to the photon flux parameter F_0.

As we can see from the figures, the time delay $\delta\tau(t)$ generated grows in a nontrivial way with the anharmonicity, parameterized with U/γ, and the driving condition

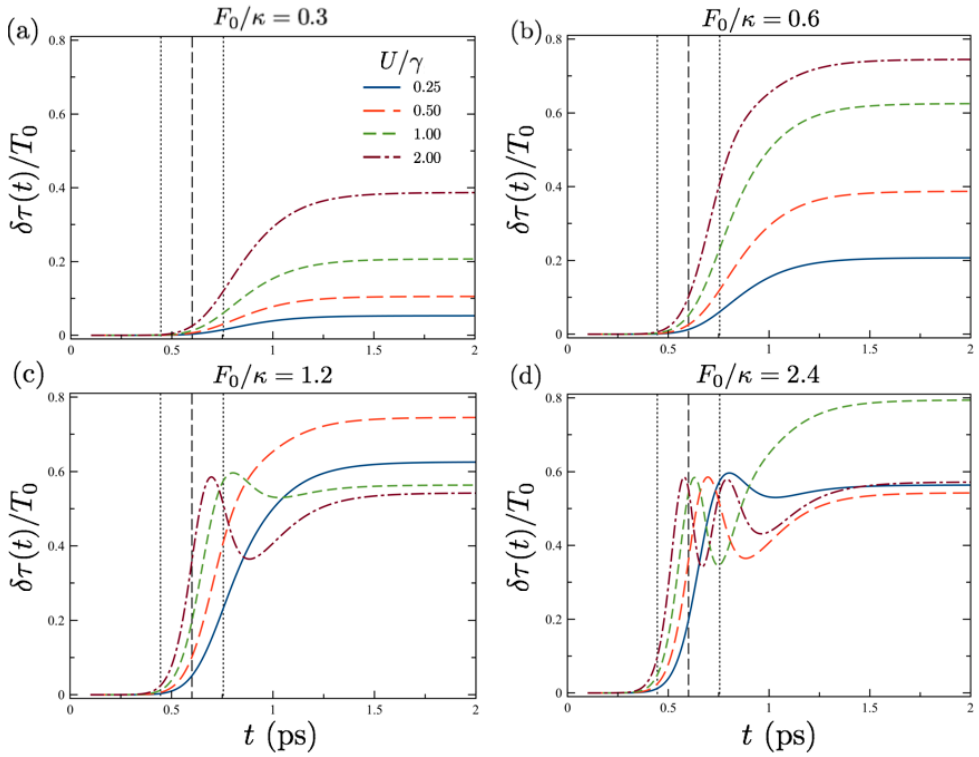

Figure 5.3.5: Adimensional time delay $\delta\tau/T_0$ considering $N = 2$, for four different driving conditions $F_0/\kappa = (0.3, 0.6, 1.2, 2.4)$ and four anharmonicity conditions $U/\gamma = (0.25, 0.50, 1.0, 2.0)$, considering the set of semi-empirical parameters $\{\omega_v, \kappa/2\pi, \gamma/2\pi, \sqrt{N}g\} = \{40.0, 12.0, 0.6, 1.00\}$ THz, intimate relationships with those used in [48]. (a) Curves considering $F_0/\kappa = 0.3$ (b) Curves considering $F_0/\kappa = 0.6$ (c) Curves considering $F_0/\kappa = 1.2$ (d) Curves considering $F_0/\kappa = 2.4$.

F_0/κ. What is clear is that for our choice of parameters, this time delay reaches a stationary value $\delta\tau_{ss}$.

The nontrivial behaviour of our system is evident for higher driving ratios (Figures 5.3.5 (c)–(b)), as a higher anharmonic condition not necessarily will bring a higher stationary time delay. Also, the simulations show a saturation effect, where no matter how much we increase the driving intensity, the time delays obtained will not increase. Instead, they will show a fluctuating behaviour before reaching a possible lower stationary value than the highest peak of the curve.

In Figure 5.3.6 we increase the number of anharmonic dipoles to $N = 16$, using the same set of parameters from Figure 5.3.5, in order to catch the dilution effect onto the anharmonicity (U/N) as well as on the collective light-matter coupling $\Omega = \sqrt{N}g$. As the chirping effect falls with $1/N$, it is not strange that higher driving intensities will be required to reach higher time delays ($\delta\tau/T_0 \sim 0.4$ for

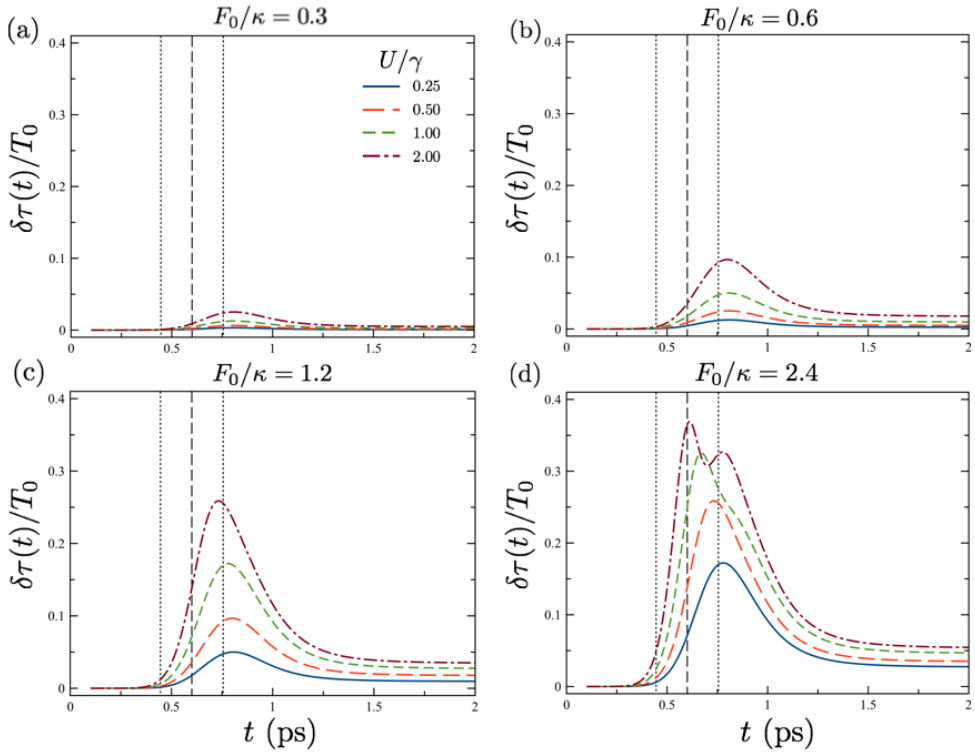

Figure 5.3.6: Simulations for a Multi-quantum well, containing $N = 16$ quantum wells, of the adimensional time delay $\delta\tau/T_0$, for four different driving conditions $F_0/\kappa = (0.3, 0.6, 1.2, 2.4)$ and four anharmonicity conditions $U/\gamma = (0.25, 0.50, 1.0, 2.0)$, considering the set of semi-empirical parameters $\{\omega_v, \kappa/2\pi, \gamma/2\pi, \sqrt{N}g\} = \{40.0, 12.0, 0.6, 1.00\}$ THz. (a) Curves considering $F_0/\kappa = 0.3$ (b) Curves considering $F_0/\kappa = 0.6$ (c) Curves considering $F_0/\kappa = 1.2$ (d) Curves considering $F_0/\kappa = 2.4$.

$F_0/\kappa \geq 2.4$). However, the stationary time delays expected are almost zero, even when its evolution reached transiently a high value close to the width of the driving pulse $t_0 - T < t < t_0 + T$. This can be explained, as we did with the case of organic vibrations in a cavity QED, by the effective bandwidth relationships between cavity and dipoles in weak coupling due to the Purcell effect. The effective dipole decay rate is *augmented* drastically by the increasing of the collective light-matter coupling Ω with higher N, keeping the cavity decay rate κ fixed, as you can check from Equation (5.2.18) and Fig. 5.2.2. This increase of the effective dipole decay rate diminish the offset ratio with respect to the cavity, destroying the stationary time delay obtained for lower N. Then, in order to have a lower dipolar decay rate, and in consequence a sharper material spectrum with respect to the cavity bandwidth for higher number of dipoles, we can decrease the individual light-matter coupling g to compensate the unavoidable collective dilution effect.

In Figure 5.3.7 we show the simulations for a MQW of $N = 16$ anharmonic dipoles

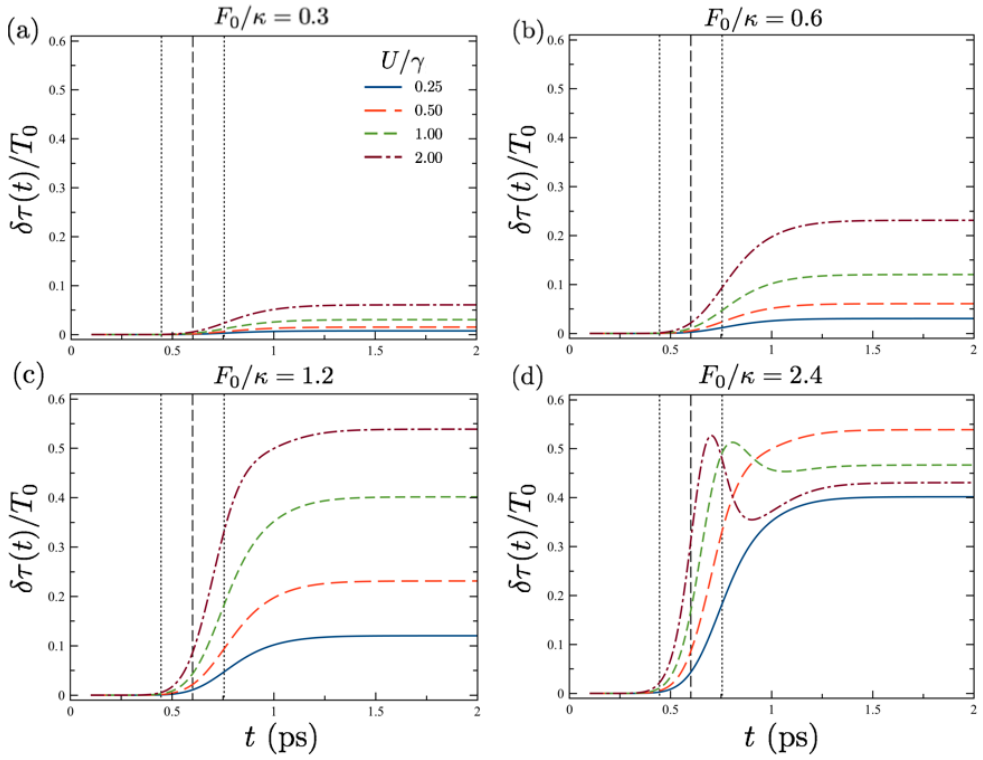

Figure 5.3.7: Simulations for a Multi-quantum well, containing $N = 16$ quantum wells but with half the coupling strength than in Figure 5.3.6, of the dimensionless time delay $\delta\tau/T_0$, for four different driving conditions $F_0/\kappa = (0.3, 0.6, 1.2, 2.4)$ and four anharmonicity conditions $U/\gamma = (0.25, 0.50, 1.0, 2.0)$, considering the set of semi-empirical parameters $\{\omega_v, \kappa/2\pi, \gamma/2\pi, \sqrt{N}g\} = \{40.0, 12.0, 0.6, 0.50\}$ THz. (a) Curves considering $F_0/\kappa = 0.3$ (b) Curves considering $F_0/\kappa = 0.6$ (c) Curves considering $F_0/\kappa = 1.2$ (d) Curves considering $F_0/\kappa = 2.4$.

but now considering half the light-matter g that in the previous simulation. As we expect, a lower enough light matter coupling will make reappear the stationary time delays that vanished for the dilution mechanism. We see that the stationary values for the delay emerge again although they never go higher than $\delta\tau_{ss}/T_0 \approx 0.5$ even for ultra high driving conditions ($F_0/\kappa = 2.4$).

5.3.3 Time delay and nonlinear phase theory

To have a deeper physical intuition about these results, we solve Eqs. (5.3.3) and (5.3.4) analytically, complementing with numerical simulations where it is needed.

In the general case, by solving these system of equations in the harmonic case ($U/\gamma \sim 0$) we analytically obtain that the linear phases for both oscillators, in

temporal domain, are fixed constants:

$$\langle \hat{a}(t)\rangle_{\mathrm{L}} = -i|\langle \hat{a}(t)\rangle_{\mathrm{L}}|e^{-i\omega t} = |\langle \hat{a}(t)\rangle_{\mathrm{L}}|e^{-i(\omega t+\pi/2)}, \tag{5.3.6}$$

$$\langle \hat{B}_0(t)\rangle_{\mathrm{L}} = -|\langle \hat{B}_0(t)\rangle_{\mathrm{L}}|e^{-i\omega t} = |\langle \hat{B}_0(t)\rangle_{\mathrm{L}}|e^{-i(\omega t+\pi)}. \tag{5.3.7}$$

and then $\phi_{\mathrm{L}}^{(a)} = -\pi/2$ and $\phi_{\mathrm{L}}^{(B_0)} = -\pi$.

The time delay is a result of a nonlinear modulation of this fixed phase, in the sense that we expect the coherences change non trivially in a way that can be written as reads:

$$\langle \hat{a}(t)\rangle_{\mathrm{NL}} = |\langle \hat{a}(t)\rangle_{\mathrm{NL}}|e^{-i\omega t+\phi_{a,\mathrm{NL}}(t)}, \tag{5.3.8}$$

$$\langle \hat{B}_0(t)\rangle_{\mathrm{NL}} = |\langle \hat{B}_0(t)\rangle_{\mathrm{NL}}|e^{-i\omega t+\phi_{B_0,\mathrm{NL}}(t)}. \tag{5.3.9}$$

What we calculate as the dimensionless time delay $\delta\tau(t)/T_0$ with respect to the linear response coherence, is nothing more than the temporal phase difference between the nonlinear and linear oscillator waves, as follows

$$\frac{1}{T_0}\delta\tau(t) = (\phi_{\mathrm{NL}}(t) - \phi_{\mathrm{L}})/\pi = \Delta\phi_{\mathrm{NL}}(t)/\pi, \tag{5.3.10}$$

where the precise form of the time delay depends on each oscillator dynamics. To this respect, we lack of a full analytical result for the temporal phase shifts $\Delta\phi_{\mathrm{NL}}(t)$ *for arbitrary driving pulse profiles.* However, the numerical results show that in the steady state, both time delays from the cavity and material coherence coincides, as it is shown in Figure 5.3.2.

Moreover, Eqs. (5.3.3–5.3.4) are solvable in the continuous wave regime (CW, by setting $\varphi(t) = 1$, for $t \geq 0$), when we call to the steady–state conditions $\{\mathrm{d}\langle\hat{a}\rangle/\mathrm{dt}, \mathrm{d}\langle\hat{B}_0\rangle/\mathrm{dt}\} \to 0$. The solutions for both cavity $\langle\tilde{a}^{\mathrm{ss}}\rangle$ and material coherences $\langle\tilde{B}_0^{\mathrm{ss}}\rangle$, expanded in their real and imaginary parts, are

$$\mathrm{Re}[\langle\tilde{a}^{\mathrm{ss}}\rangle] = -\frac{2U}{NF_0}|\langle\tilde{B}_0^{\mathrm{ss}}\rangle|^4, \tag{5.3.11}$$

$$\mathrm{Im}[\langle\tilde{a}^{\mathrm{ss}}\rangle] = \frac{\tilde{\gamma}}{2F_0}|\langle\tilde{B}_0^{\mathrm{ss}}\rangle|^2 - \frac{2F_0}{\kappa}, \tag{5.3.12}$$

$$\mathrm{Re}[\langle\tilde{B}_0^{\mathrm{ss}}\rangle] = -\frac{1}{R_0}|\langle\tilde{B}_0^{\mathrm{ss}}\rangle|^2, \tag{5.3.13}$$

$$\mathrm{Im}[\langle\tilde{B}_0^{\mathrm{ss}}\rangle] = -\frac{4U}{N\tilde{\gamma}R_0}|\langle\tilde{B}_0^{\mathrm{ss}}\rangle|^4, \tag{5.3.14}$$

where $|\langle\tilde{B}_0^{\rm ss}\rangle|^2$ is obtained from the cubic equation

$$|\langle\tilde{B}_0^{\rm ss}\rangle|^6+\left(\frac{N\tilde{\gamma}}{4U}\right)^2|\langle\tilde{B}_0^{\rm ss}\rangle|^2-\left(\frac{N\tilde{\gamma}R_0}{4U}\right)^2=0, \tag{5.3.15}$$

and we use the definitions $R_0=4\sqrt{N}gF_0/(\kappa\tilde{\gamma})$ and $\tilde{\gamma}=\gamma P_{\rm dip}$. These two coherences give raise to two different steady–state nonlinear phase shifts, which read as follows

$$\Delta\phi_{\rm NL,CW}^{(a)}=\arctan\left(\frac{4U|\langle\tilde{B}_0^{\rm ss}\rangle|^4}{N\left(\tilde{\gamma}|\langle\tilde{B}_0^{\rm ss}\rangle|^2-4F_0^2/\kappa\right)}\right), \tag{5.3.16}$$

$$\Delta\phi_{\rm NL,CW}^{(B_0)}=\arctan\left(\frac{4U}{N\tilde{\gamma}}|\langle\tilde{B}_0^{\rm ss}\rangle|^2\right). \tag{5.3.17}$$

The details about the derivation of these equations can be found in A3.

In Figure 5.3.8 we show the comparison between the nonlinear phase shifts $\Delta\phi_{\rm NL}(t)$ obtained from Gaussian pulses centered at $t_0=0.6$ ps and width $T=0.6$ ps with respect to the analytical phase shifts in the CW regime from Eqs. (5.3.16–5.3.17), using the same values for F_0/κ and U/γ and similar material and optical parameters of the previous calculations. We found numerically that for the range of parameters of our interest, the nonlinear phase shift $\Delta\phi_{\rm NL}(t)$ generated with finite pulses relies in the region delimited by the two curves in Fig. 5.3.8-(d), which correspond to the statement $|\Delta\phi_{\rm NL,CW}^{(a)}|\leq\Delta\phi_{\rm NL,ss}\leq\Delta\phi_{\rm NL,CW}^{(B_0)}$. We mention that the curves obey the following exponential scaling obtained from a numerical fitting

$$\frac{F_0}{\kappa}=A\left(\frac{U}{\gamma}\right)^{\varepsilon}, \tag{5.3.18}$$

where, for the parameters chosen, we found that $\varepsilon\approx-0.5$, $A_a\approx0.16339$ and $A_{B_0}\approx0.350919$. Again, the phase shifts derived from the cavity coherences, in both continous or pulsed regimes, present discontinuities due to beatings emerging in the time lapse when the driving pulse is active, and then they are plotted only since $t\geq1$ ps.

Although these shifts obtained in the CW regime are just referential, they provide an analytical tool of interesting physical insight. From Figure 5.3.8–(d) it can be noticed that for higher anharmonicity of the system, the range of validity of

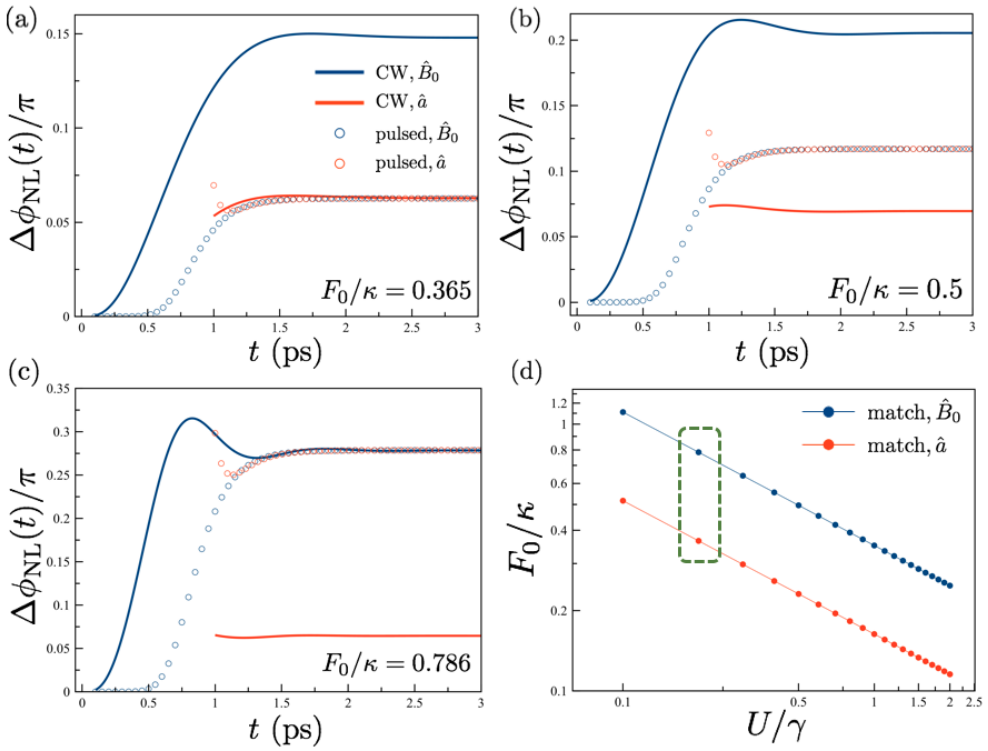

Figure 5.3.8: Comparison of the nonlinear phase shifts $\Delta\phi_{\rm NL}(t)$, for fixed anharmonicity $U/\gamma = 0.2$, obtained from the CW regime (solid lines) and the shifts obtained with finite Gaussian pulses, considering $N = 2$ and the fixed parameters $\{\omega_{\rm v}, \kappa/2\pi, \gamma/2\pi, \sqrt{N}g\} = \{40.0, 12.0, 0.6, 1.0\}$ THz. (a) CW cavity $\Delta\phi_{\rm NL}^{(a)}$ (blue line) and dipolar $\Delta\phi_{\rm NL}^{(B_0)}$ (orange line) phase shifts, compared with the cavity (orange circles) and dipolar (blue circles) phase shifts generated by finite Gaussian pulses with $\{t_0, T\} = \{0.6, 0.155\}$ ps, respectively. (b) The same as previously, fixing $F_0/\kappa = 0.5$. (c) The same as previously, fixing $F_0/\kappa = 0.786$. (d) Log–log plot of the matching conditions between the pulsed–generated phase shifts (equal for both cavity and dipolar coherences) and the cavity (orange lines with circles) and dipolar CW phase shifts (blue lines with circles). The 3 previous figures correspond to the marked region in a green dashed box, specifically, the orange dot ($F_0/\kappa = 0.365$) correlates with figure (a), the blue dot ($F_0/\kappa = 0.786$) correspond to figure (c) and figure (b) relies in the intermediate zone ($F_0/\kappa = 0.5$).

the equations implies lower driving ratios. Beyond this region (upper side of the blue line with circles in 5.3.8–(d)), the dillute regime of low excitations of the anharmonic dipoles break down, and we cannot ensure about the validity of the mean field approach we use in this work. However, by taking the linear value of

$$|\langle \tilde{B}_0^{\rm ss}\rangle_{\rm L}|^2 = \frac{16F_0^2Ng^2}{4Ng^2 + (\kappa\gamma)^2} \sim \mathcal{O}(F_0^2/\kappa^2) \tag{5.3.19}$$

we expect that for the set of parameters we are interested, the scaling of the nonlinear phases with finite pulses goes approximately with the square of the driving ratio F_0^2/κ^2, which in turn is related with the photon flux $\kappa\langle\hat{a}^\dagger\hat{a}\rangle$. A more detailed derivation can be found in A3.

5.3.4 Quadratic ansatz for the nonlinear stationary phase shift

We can also derive an semi-analytical form for the nonlinear phase shift in the case we drive the cavity with finite pulses.

If we assume that the bandwidth of the dipole resonance is much smaller than the antenna bandwidth, i.e., $\kappa \gg \gamma$ (which is our case as we fixed $\kappa/\gamma \approx 20$ for our numerical simulations), we can adiabaticaly eliminate the antenna field from the dynamics. Then, the evolution of the bright mode after the pulse is over is given by

$$\langle \hat{B}_0(t) \rangle = B_{\text{off}} e^{-\frac{\tilde{\gamma}}{2}(t-t_{\text{off}})} e^{i\phi(t)} \tag{5.3.20}$$

where t_{off} is the pulse turn-off time. The phase evolves as

$$\phi(t) = \phi_{\text{off}} + \frac{2UB_{\text{off}}^2}{N\tilde{\gamma}} \left\{ 1 - e^{-\tilde{\gamma}(t-t_{\text{off}})} \right\}, \tag{5.3.21}$$

where $\tilde{\gamma} = \gamma(1 + 4Ng^2/\kappa\gamma)$ is the Purcell-enhanced dipole decay rate, as we found in the linear response sceneario Eq. (5.2.21), $B_{\text{off}} = |\langle \hat{B}_0(t_{\text{off}}) \rangle|$ and ϕ_{off} is the residual nonlinear phase from the time evolution where the pulse is actively driving the cavity. Defining $\tau = t - t_{\text{off}}$, in the long time regime, $\tau\tilde{\gamma} \gg 1$, Eq. (5.3.21) gives the stationary relative phase

$$\Delta\phi_{\text{NL}}^{(\text{ss})} = \frac{2UB_{\text{off}}^2}{N\tilde{\gamma}} + \phi_{\text{off}} - \pi \approx \alpha_{\text{fit}} \frac{2U}{N\tilde{\gamma}} \left(\frac{F_0}{\kappa} \right)^2, \tag{5.3.22}$$

which depends quadratically on the laser strength for low enough driving pulses (see Fig. 5.3.8), through the implicit linear dependence of B_{off} on F_0, that we postulate as an ansatz using a fitting parameter α_{fit} in order to match the postulated proportionality, in the same "spirit" of our previous analysis using the CW formalism and the referential analytical equations. The derivation of Eq. (5.3.21) can be found in Appendix A4. In the limiting cases of harmonic oscillators ($U = 0$), thermodynamic limit ($N \to \infty$), or linear response ($F_0/\kappa \ll 1$), the relative phase is negligible ($\Delta\phi_{\text{NL}}^{(\text{ss})} \approx 0$).

In Figure 5.3.9 we contrast the numerical results for the stationary phase shifts as a function of the driving ratio F_0/κ (with dashed lines), in a log–log plot, with the quadratic scaling with fit parameters α_{fit} (empty circles) to visualize

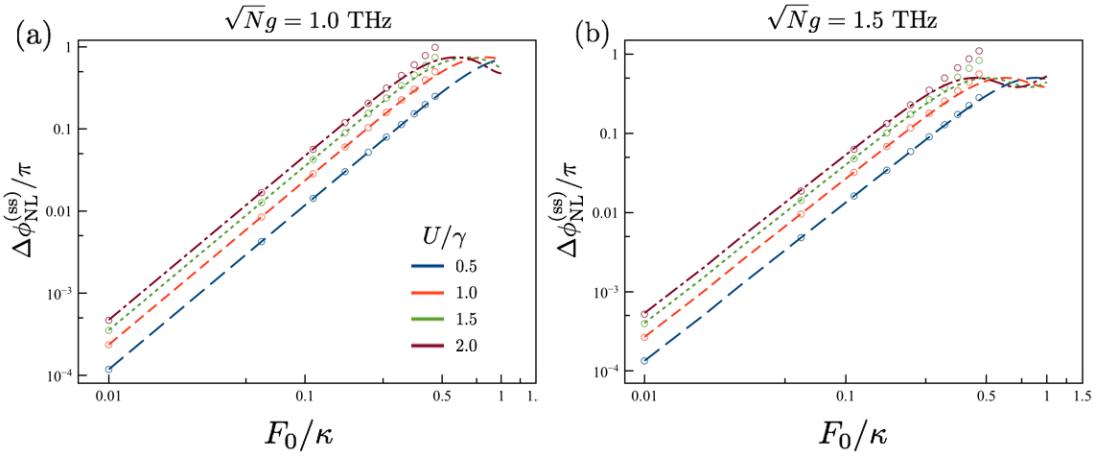

Figure 5.3.9: Log–log plot of the stationary nonlinear phase shifts for two coupling regimes, compared with a quadratic fit (circles), as it is proposed with our ansatz. The fixed parameters chosen are $\{\omega_0, \kappa/2\pi, \gamma/2\pi\} = \{40, 12, 0.6\}$ THz, with $N = 2$. (a) Steady–state nonlinear phase shift as a function of the driving ratio F_0/κ for $\sqrt{N}g = 1.0$ THz, considering 4 different anharmonicity conditions, obtained numerically (dashed lines). The circles mark the best quadratic fittings, up to $F_0/\kappa = 0.2$. The numerical fit parameters are $\alpha_{\mathrm{fit}} = \{2.35612, 2.35093, 2.34238, 2.33057\}$, from the bottom curve to the upper one, respectively. (b) Steady–state nonlinear phase shift as a function of the driving ratio F_0/κ for $\sqrt{N}g = 1.5$ THz. The circles mark the best quadratic that fits, up to $F_0/\kappa = 0.2$. The numerical fit parameters are $\alpha_{\mathrm{fit}} = \{2.68058, 2.66574, 2.6407, 2.60717\}$, from the bottom curve to the upper one, respectively.

easily this power scaling ansatz. It is interesting to notice that, even when the fit approximates succesfully for lower intentities, for $F_0/\kappa \sim 0.5$ the approximation breaks, which it is not strange as in general the nonlinear dynamics of these models allow for this kind of complexity. We include the fit parameters α_{fit} obtained numerically, in the caption of the figure.

We notice that those parameters are quite close between different choices of anharmonicities, however they change strongly with the coupling strenght choice, as it can be seen in the comparison between figures (a) and (b).

Let's remember that molecular ensembles have low anharmonicities, and have been shown to require higher pulse strengths to produce finite relative phases [68] than the ones discussed here. Besides, intersubbands in MQW's allow for higher anharmonicities and lower number of dipoles than molecules, and then present themselves as more optimal nanoplatforms to perform phase modulation [3].

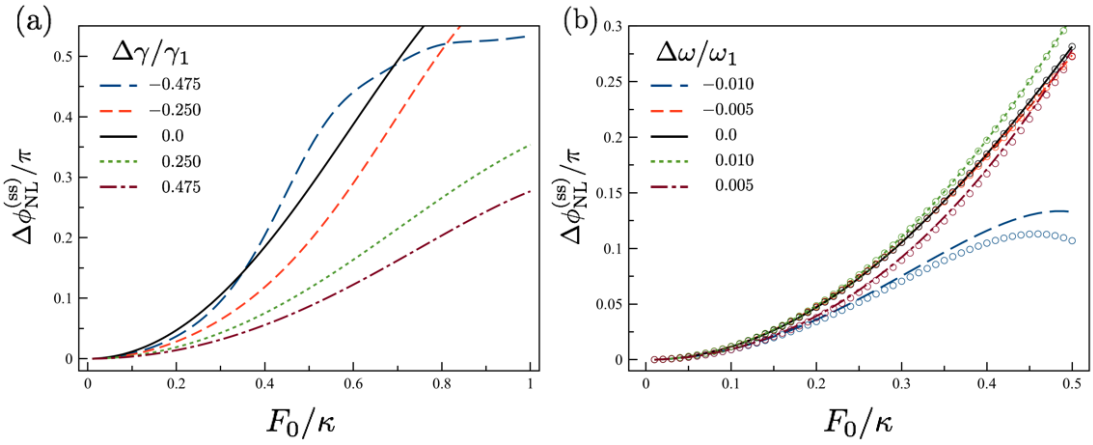

Figure 5.4.1: Numerical nonlinear phase shifts considering as a function of the driving ratio F_0/κ, for different levels of inhomogeinity between the $N = 2$ anharmonic dipoles considered, with anharmonicity ratio $U/\gamma = 0.5$. The fixed parameters chosen are $\{\omega_1, \kappa/2\pi, \gamma_1/2\pi, \sqrt{N}g\} = \{40, 12, 0.6, 1.0\}$ THz (a) Relative nonlinear phase considering changes in the local decay rate γ_2 of the second anharmonic dipole. The homogeneous case is marked with a solid black line ($\Delta\gamma = (\gamma_2 - \gamma_1)/2 = 0$). The explicit values chosen were $\gamma_2/2\pi = \{0.03, 0.3, 0.6, 0.9, 1.17\}$ THz, from the blue dashed line to the brown one, respectively. (b) Relative nonlinear phase considering changes in the local fundamental frequency ω_2 of the second anharmonic dipole. The homogeneous case is marked with a solid black line ($\Delta\omega = (\omega_2 - \omega_1)/2 = 0$). The explicit values chosen were $\omega_2 = \{39.2, 39.6, 40., 40.4, 40.8\}$ THz, from the blue dashed line to the brown one, respectively. Empty circles marks the phase shifts obtained from the simulated dipole collective coherence $\langle \hat{B}_0 \rangle$, as this was the only case when this differs minimally from the phases obtained directly from $\langle \hat{a} \rangle$.

5.4 Dark states contribution to the nonlinear dynamics

Before starting, let's mention that even when mathematically one can modify all the local parameters individually (fundamental frequencies and decay rates ω_n, γ_n, coupling strengths g_n and anharmonicity parameters U_n, respectively), we are interested exclusively in the center and bandwidth associated with the fundamental frequency resonance of the oscillators. We show that this is enough to break the permutation symmetry of the collective system, and for our purposes this gives us a lot of insight about how the nonlinear effects are modified with respect to the case of identical dipoles.

5.4.1 Variations in the local bandwidths and fundamental frequencies

The equation of motion for the n–th local dipole coherence is

$$\frac{\mathrm{d}}{\mathrm{dt}}\langle\hat{b}_n\rangle = -\left(\frac{\gamma_n}{2} + i\omega_n\right)\langle\hat{b}_n\rangle - ig\langle\hat{a}\rangle + i2U|\langle\hat{b}_n\rangle|^2\langle\hat{b}_n\rangle. \tag{5.4.1}$$

In the collective basis we have that

$$\frac{\mathrm{d}}{\mathrm{dt}}\langle\hat{B}_\alpha\rangle = \frac{1}{\sqrt{N}}\sum_{n=1}^{N} e^{\frac{i2\pi}{N}\alpha n}\left(\frac{\mathrm{d}}{\mathrm{dt}}\langle\hat{b}_n\rangle\right).$$

With this at hand, we can express a more general form of the α-th dipole coherence as follows

$$\frac{\mathrm{d}}{\mathrm{dt}}\langle\hat{B}_\alpha\rangle = -\left(\frac{\bar{\gamma}}{2} + i\bar{\omega}'(t)\right)\langle\hat{B}_\alpha\rangle - i\delta_{\alpha,0}\sqrt{N}g\langle\hat{a}\rangle - \sum_{\beta\neq\alpha}\Gamma'_{\alpha,\beta}(t)\langle\hat{B}_\beta\rangle, \tag{5.4.2}$$

where we defined implicitly the mean dipole decay rate $\bar{\gamma} = \sum_n \gamma_n/N$, the instantaneous or *chirping* frequency with mean fundamental frequency $\bar{\omega} = \sum_n \omega_n/N$

$$\bar{\omega}'(t) = \bar{\omega} - \frac{2U}{N}\sum_{\beta=1}^{N-1}|\langle\hat{B}_\beta(t)\rangle|^2, \tag{5.4.3}$$

and

$$\Gamma'_{\alpha,\epsilon}(t) = \Gamma_{\alpha,\epsilon} - i\frac{2U}{N}\sum_{\beta=0}^{N-1}\langle\hat{B}_\beta(t)\rangle^*\langle\hat{B}_{\alpha+\beta-\epsilon(\mathrm{mod}N)}(t)\rangle, \tag{5.4.4}$$

$$\Gamma_{\alpha,\beta} = \frac{1}{N}\sum_{n=1}^{N}\left(\frac{\gamma_n}{2} + i\omega_n\right)e^{\frac{i2\pi}{N}(\alpha-\beta)n}. \tag{5.4.5}$$

In the particular case of $N = 2$, these equations implies that the bright and dark states, $\hat{B}_0$ and $\hat{B}_1$, respectively, couple to each other symmetrically, although the only mode directly connected with the cavity field remains to be only the bright

mode $\hat{B}_0$. Explicitly, we obtain that

$$\frac{\mathrm{d}}{\mathrm{dt}}\langle\hat{a}\rangle = -\left(\frac{\kappa}{2}+i\omega_0\right)\langle\hat{a}\rangle - i\sqrt{N}g\langle\hat{B}_0\rangle - i\tilde{F}_\mathrm{d}(t), \tag{5.4.6}$$

$$\frac{\mathrm{d}}{\mathrm{dt}}\langle\hat{B}_0\rangle = -\left(\frac{\bar{\gamma}}{2}+i\bar{\omega}'(t)\right)\langle\hat{B}_0\rangle - \left(\frac{\Delta\gamma}{2}+i\Delta\omega(t)\right)\langle\hat{B}_1\rangle - i\sqrt{N}g\langle\hat{a}\rangle, \tag{5.4.7}$$

$$\frac{\mathrm{d}}{\mathrm{dt}}\langle\hat{B}_1\rangle = -\left(\frac{\bar{\gamma}}{2}+i\bar{\omega}'(t)\right)\langle\hat{B}_1\rangle - \left(\frac{\Delta\gamma}{2}+i\Delta\omega(t)\right)\langle\hat{B}_0\rangle, \tag{5.4.8}$$

with

$$\bar{\omega}'(t) = \bar{\omega} - U\left(|\langle\hat{B}_0(t)\rangle|^2 + |\langle\hat{B}_1(t)\rangle|^2\right)$$

and

$$\Delta\omega(t) = \Delta\omega - 2U\mathrm{Re}[\langle\hat{B}_0(t)\rangle^*\langle\hat{B}_1(t)\rangle],$$

where $\Delta\gamma = (\gamma_2-\gamma_1)/2$ and $\Delta\omega = (\omega_2-\omega_1)/2$, in th resonant condition $\omega_\mathrm{d} = \omega_\mathrm{c} = \omega_1$

The numerical results from the inhomogeneous system in Eqs. (5.4.6–5.4.8) are plotted in Figure 5.4.1, for a $N = 2$ MQW, fixing the local dipole $\hat{b}_1$ and changing the second local dipole decay rate γ_2 (figure (a)) or the local fundamental frequency ω_2 (figure (b)).

In Figure 5.4.1–(a), the second decay rate is changed, generating important changes with respect to the homogeneous case (solid black line). In particular, it is shown that when $\gamma_2/2\pi = 0.03$ THz, low compared with γ_1, the nonlinear phase shift is enhanced for an specific range of driving parameters $0.4 \lesssim F_0/\kappa \lesssim 0.6$. For all the others parameter choices, when $\gamma_2 > \gamma_1$ (green and brown dashed curves) or even when the second decay rate is just half the first one ($\gamma_2 = 0.5\gamma_1$, orange dashed curve), the inhomogeneous simulations go substantially below the symmetric one.

In the second simulations, plotted in Figure 5.4.1–(b), what is changed is the second fundamental frequency, and again this generates interesting changes with respect to the homogeneous case (solid black line). In particular, when the second fundamental frequency is subtly above ω_1 (green dashed line), we obtain a minimally high nonlinear phase shift.

Moreover, this is the only numerical set of calculations where the phase shifts

obtained from the cavity coherence (dashed lines) and the shifts from the bright state (empty circles), are different, although the changes are quite minimal.

In the opposite case, when $\omega_2 < \omega_1$ (orange and blue dashed lines), the red–detuning destroys the relative nonlinear phase. Besides, the orange curve ($\omega_2 = 39.6$ THz $< \omega_1$) is almost overlapped with respect to the black one.

Summarizing, we obtained that for very specific physical situations, encoded with the set of parameters chosen, it can be obtaind even higher nonlinear phase shifts that the obtained in homogeneous conditions, e.g., with identical QW dipoles inside the MQW structure. Of course, as these calculations were done with an specific choice of material conditions to match with reported experimental values, results may differ substantially. In [3], parameters are similar but lower, and this is enough to get pretty different relative phases.

Finally, all the simulations were carried in the temporal domain. For interesting annalysis in Fourier domain, let's visit references [68, 3]. Frequency observables, as the analyzed in [68], are carried just using the FID signal of the cavity coherence (e.g., when the pulse is almost vanished and the dynamics is free of the source), and then those will not necessarily do a perfect match with our time–dependent nonlinear phase modulations.

Chapter 6

Conclusion

In this thesis, we described a novel dynamical anharmonic mechanism in THz cavity QED that can be used for imprinting power-dependent phase shifts on the electromagnetic response of a coupled cavity-dipole system. We develop analytical quantum mechanical theory to model free-induction decay signals of a pulse-driven cavity system, using parameters that are relevant for quantum well intersubband transitions in mid-infrared resonators [48], as well as for molecular vibrations in the mid-infrared regime. For N quantum wells within the near field of the driven resonator, the theory shows that using only a moderately strong pulse that drives a small fraction of the intersubband level population to the second excitation manifold, a stationary phase shift proportional to the spectral anharmonicity parameter $U/N\gamma$ and the photon flux of the pulse, can be imprinted on the FID response of the near field, which can then be retrieved using time-domain spectroscopic techniques [72]. For experimentally relevant system parameters, nonlinear phase shifts of order of 1 radian are predicted for a small number of dipoles like two molecular vibrations or two quantum wells embedded in a MQW, using single sub-picosecond pulses of few μW power.

The predicted phase nonlinearity can be physically understood as a result of laser-induced dipole effect that dynamically detunes the cavity field with respect to the $1 \rightarrow 2$ dipolar transition, caused by population driven between the first and second excited levels of the anharmonic material spectrum.

Our work demonstrates the feasibility of implementing nonlinear phase operations at THz frequencies using current available nanocavities [48, 50, 72] and contributes

to the development of quantum optics in the high-THz regime [22, 4], which can enable fundamental studies of cavity quantum electrodynamics [14, 71], material and molecular spectroscopy [40, 72, 8], and controlled chemistry in confined electromagnetic environments [53, 1]. Extensions of this work to the analysis of THz and infrared pulses with non-classical field statistics [70, 76] could open further possibilities for developing ultra-fast quantum information processing at room temperature.

Bibliography

[1] Ahn, W., Triana, J. F., Recabal, F., Herrera, F., and Simpkins, B. S. (2023). Modification of ground-state chemical reactivity via light–matter coherence in infrared cavities. *Science*, 380(6650):1165–1168.

[2] Albarelli, F., Ferraro, A., Paternostro, M., and Paris, M. G. (2016). Nonlinearity as a resource for nonclassicality in anharmonic systems. *Physical Review A*, 93(3):032112.

[3] Arias, M., Triana, J. F., Delgado, A., and Herrera, F. (2023). Coherent anharmonicity transfer from matter to light in the thz regime.

[4] Benea-Chelmus, I.-C., Settembrini, F. F., Scalari, G., and Faist, J. (2019). Electric field correlation measurements on the electromagnetic vacuum state. *Nature*, 568(7751):202–206.

[5] Bera, D., Qian, L., Tseng, T.-K., and Holloway, P. H. (2010). Quantum dots and their multimodal applications: A review. *Materials*, 3(4):2260–2345.

[6] Boyd, R. W. (2008). Chapter 7 - processes resulting from the intensity-dependent refractive index. In Boyd, R. W., editor, *Nonlinear Optics*, pages 329–390. Academic Press, Burlington, third edition edition.

[7] Burroughes, J. H., Bradley, D. D. C., Brown, A. R., Marks, R. N., Mackay, K., Friend, R. H., Burns, P. L., and Holmes, A. B. (1990). Light-emitting diodes based on conjugated polymers. *Nature*, 347(6293):539–541.

[8] Bylinkin, A., Schnell, M., Autore, M., Calavalle, F., Li, P., Taboada-Gutièrrez, J., Liu, S., Edgar, J. H., Casanova, F., Hueso, L. E., Alonso-Gonzalez, P., Nikitin, A. Y., and Hillenbrand, R. (2021). Real-space observation of vibrational strong coupling between propagating phonon polaritons and organic molecules. *Nature Photonics*, 15(3):197–202.

[9] Carmichael, H. J. (1987). Spectrum of squeezing and photocurrent shot noise: a normally ordered treatment. *J. Opt. Soc. Am. B*, 4(10):1588–1603.

[10] Carmichael, H. J. (1999a). *Dissipation in Quantum Mechanics: The Master Equation Approach*, pages 1–28. Springer Berlin Heidelberg, Berlin, Heidelberg.

[11] Carmichael, H. J. (1999b). *The Single-Mode Homogeneously Broadened Laser I: Preliminaries*, pages 257–304. Springer Berlin Heidelberg, Berlin, Heidelberg.

[12] Chang, D. E., Vuletić, V., and Lukin, M. D. (2014). Quantum nonlinear optics —photon by photon. *Nature Photonics*, 8(9):685–694.

[13] Dalafi, A. and Naderi, M. (2017). Intrinsic cross-kerr nonlinearity in an optical cavity containing an interacting bose-einstein condensate. *Physical Review A*, 95(4):043601.

[14] De Liberato, S. (2019). Electro-optical sampling of quantum vacuum fluctuations in dispersive dielectrics. *Phys. Rev. A*, 100:031801.

[15] Drummond, P. and Walls, D. (1980a). Quantum theory of optical bistability. i. nonlinear polarisability model. *Journal of Physics A: Mathematical and General*, 13(2):725.

[16] Drummond, P. D. and Walls, D. F. (1980b). Quantum theory of optical bistability. i. nonlinear polarisability model. *Journal of Physics A: Mathematical and General*, 13(2):725.

[17] F. Ribeiro, R., Dunkelberger, A. D., Xiang, B., Xiong, W., Simpkins, B. S., Owrutsky, J. C., and Yuen-Zhou, J. (2018). Theory for nonlinear spectroscopy of vibrational polaritons. *The Journal of Physical Chemistry Letters*, 9(13):3766–3771.

[18] Fleming, C., Cummings, N., Anastopoulos, C., and Hu, B.-L. (2010). The rotating-wave approximation: consistency and applicability from an open quantum system analysis. *Journal of Physics A: Mathematical and Theoretical*, 43(40):405304.

[19] Fox, M. and Ispasoiu, R. (2017). *Quantum Wells, Superlattices, and Band-Gap Engineering*, pages 1–1. Springer International Publishing, Cham.

[20] Fulmer, E. C., Mukherjee, P., Krummel, A. T., and Zanni, M. T. (2004). A pulse sequence for directly measuring the anharmonicities of coupled vibrations: Two-quantum two-dimensional infrared spectroscopy. *The Journal of chemical physics*, 120(17):8067–8078.

[21] Gerry, C. and Knight, P. (2004). *Introductory Quantum Optics*. Cambridge University Press.

[22] Goulain, P., Deimert, C., Jeannin, M., Bousseksou, A., Pasek, W., Wasilewski, Z. R., Colombelli, R., and Manceau, J.-M. (2022). Thz ultra-strong light-matter coupling up to 200k with continuously-graded parabolic quantum wells embedded in microcavities. In *2022 47th International Conference on Infrared, Millimeter and Terahertz Waves (IRMMW-THz)*, pages 1–1.

[23] Goy, P., Raimond, J. M., Gross, M., and Haroche, S. (1983). Observation of cavity-enhanced single-atom spontaneous emission. *Phys. Rev. Lett.*, 50:1903–1906.

[24] Grafton, A. B., Dunkelberger, A. D., Simpkins, B. S., Triana, J. F., Hernández,

F. J., Herrera, F., and Owrutsky, J. C. (2021). Excited-state vibration-polariton transitions and dynamics in nitroprusside. *Nature Communications*, 12(1):214.

[25] Grice, A. W., Tajbakhsh, A., Burn, P. L., and Bradley, D. D. C. (1997). A blue-emitting triazole-based conjugated polymer. *Advanced Materials*, 9(15):1174–1178.

[26] Hao, X., Yang, W.-X., Lü, X., Liu, J., Huang, P., Ding, C., and Yang, X. (2008). Polarization qubit phase gate in a coupled quantum-well nanostructure. *Physics Letters A*, 372(47):7081–7085.

[27] Haroche, S. and Kleppner, D. (1989). Cavity Quantum Electrodynamics. *Physics Today*, 42(1):24–30.

[28] Hermann, R. J. and Gordon, M. J. (2018). Nanoscale optical microscopy and spectroscopy using near-field probes. *Annual Review of Chemical and Biomolecular Engineering*, 9(1):365–387. PMID: 29596000.

[29] Hernández, F. J. and Herrera, F. (2019). Multi-level quantum Rabi model for anharmonic vibrational polaritons. *The Journal of Chemical Physics*, 151(14):144116.

[30] Herrera, F. and Spano, F. C. (2016). Cavity-controlled chemistry in molecular ensembles. *Phys. Rev. Lett.*, 116:238301.

[31] Herrera, F. and Spano, F. C. (2017). Absorption and photoluminescence in organic cavity qed. *Phys. Rev. A*, 95:053867.

[32] Ho, S. T., Soccolich, C. E., Islam, M. N., Hobson, W. S., Levi, A. F. J., and Slusher, R. E. (1991). Large nonlinear phase shifts in lowloss AlxGa1xAs waveguides near halfgap. *Applied Physics Letters*, 59(20):2558–2560.

[33] Hobson, P. A., Barnes, W. L., Lidzey, D. G., Gehring, G. A., Whittaker, D. M., Skolnick, M. S., and Walker, S. (2002). Strong exciton–photon coupling in a low-Q all-metal mirror microcavity. *Applied Physics Letters*, 81(19):3519–3521.

[34] Hulet, R. G., Hilfer, E. S., and Kleppner, D. (1985). Inhibited spontaneous emission by a rydberg atom. *Phys. Rev. Lett.*, 55:2137–2140.

[35] Hutchison, J. A., Schwartz, T., Genet, C., Devaux, E., and Ebbesen, T. W. (2012). Modifying chemical landscapes by coupling to vacuum fields. *Angewandte Chemie International Edition*, 51(7):1592–1596.

[36] Jackson, J. D. (2003). *Electrodynamics, Classical*. John Wiley & Sons, Ltd.

[37] Jaynes, E. and Cummings, F. (1963). Comparison of quantum and semiclassical radiation theories with application to the beam maser. *Proceedings of the IEEE*, 51(1):89–109.

[38] Kerr, J. (1875). Xl. a new relation between electricity and light: Dielectrified media birefringent. *The London, Edinburgh, and Dublin Philosophical Magazine and Journal of Science*, 50(332):337–348.

[39] Kimble, H. J. (1998). Strong interactions of single atoms and photons in cavity qed. *Physica Scripta*, 1998(T76):127.

[40] Kizmann, M., Moskalenko, A. S., Leitenstorfer, A., Burkard, G., and Mukamel, S. (2022). Quantum susceptibilities in time-domain sampling of electric field fluctuations. *Laser & Photonics Reviews*, 16(3):2100423.

[41] Klimov, A. B. and Chumakov, S. M. (2009a). *Appendices*, chapter 11, pages 279–314. John Wiley & Sons, Ltd.

[42] Klimov, A. B. and Chumakov, S. M. (2009b). *Field Dynamics*, chapter 4, pages 71–82. John Wiley & Sons, Ltd.

[43] Koren, U., Koch, T. L., Presting, H., and Miller, B. I. (1987). InGaAs/InP multiple quantum well waveguide phase modulator. *Applied Physics Letters*, 50(7):368–370.

[44] Kulkeratiyut, S., Kulkeratiyut, S., and Blum, F. D. (2006). Bound carbonyls in pmma adsorbed on silica using transmission ftir. *Journal of Polymer Science Part B: Polymer Physics*, 44(15):2071–2078.

[45] Kuzyk, M. G., Singer, K. D., and Stegeman, G. I. (2013). Theory of molecular nonlinear optics. *Advances in Optics and Photonics*, 5(1):4–82.

[46] Lidzey, D. G., Bradley, D. D. C., Skolnick, M. S., Virgili, T., Walker, S., and Whittaker, D. M. (1998). Strong exciton–photon coupling in an organic semiconductor microcavity. *Nature*, 395(6697):53–55.

[47] Lindblad, G. (1976). On the generators of quantum dynamical semigroups. *Communications in Mathematical Physics*, 48(2):119–130.

[48] Mann, S. A., Nookala, N., Johnson, S. C., Cotrufo, M., Mekawy, A., Klem, J. F., Brener, I., Raschke, M. B., Alù, A., and Belkin, M. A. (2021). Ultrafast optical switching and power limiting in intersubband polaritonic metasurfaces. *Optica*, 8:606–613.

[49] Mekawy, A. and Alù, A. (2020). Giant midinfrared nonlinearity based on multiple quantum well polaritonic metasurfaces. *Nanophotonics*, 10(1):667–678.

[50] Metzger, B., Muller, E., Nishida, J., Pollard, B., Hentschel, M., and Raschke, M. B. (2019). Purcell-enhanced spontaneous emission of molecular vibrations. *Phys. Rev. Lett.*, 123:153001.

[51] Milonni, P., Ackerhalt, J., and Galbraith, H. (1983). Chaos in the semiclassical n-atom jaynes-cummings model: Failure of the rotating-wave approximation. *Physical Review Letters*, 50(13):966.

[52] Morse, P. M. (1929). Diatomic molecules according to the wave mechanics. ii. vibrational levels. *Phys. Rev.*, 34:57–64.

[53] Nagarajan, K., Thomas, A., and Ebbesen, T. W. (2021). Chemistry

under vibrational strong coupling. *Journal of the American Chemical Society*, 143(41):16877–16889.

[54] O'Brien, J. L. (2007). Optical quantum computing. *Science*, 318(5856):1567–1570.

[55] Panteley, E., Loria, A., and Ati, A. E. (2015). On the stability and robustness of stuart-landau oscillators. *IFAC-PapersOnLine*, 48(11):645–650. 1st IFAC Conference on Modelling, Identification and Control of Nonlinear Systems MICNON 2015.

[56] Piryatinski, A., Chernyak, V., and Mukamel, S. (2001). Two-dimensional correlation spectroscopies of localized vibrations. *Chemical Physics*, 266:311–322.

[57] Purcell, E. M., Torrey, H. C., and Pound, R. V. (1946). Resonance absorption by nuclear magnetic moments in a solid. *Phys. Rev.*, 69:37–38.

[58] Rempe, G., Walther, H., and Klein, N. (1987). Observation of quantum collapse and revival in a one-atom maser. *Phys. Rev. Lett.*, 58:353–356.

[59] Saurabh, P. and Mukamel, S. (2016). Two-dimensional infrared spectroscopy of vibrational polaritons of molecules in an optical cavity. *J. Chem. Phys.*, 144(12).

[60] Scheel, S. and Buhmann, S. Y. (2009). Macroscopic qed-concepts and applications. *arXiv preprint arXiv:0902.3586*.

[61] Scully, M. O. and Zubairy, M. S. (1997). *Quantum Optics*. Cambridge University Press.

[62] Shan, Y., Tang, J., Wu, L., Lu, S., Dai, X., and Xiang, Y. (2019). Spatial self-phase modulation and all-optical switching of graphene oxide dispersions. *Journal of Alloys and Compounds*, 771:900–904.

[63] Stolz, I. W., Dobson, G. R., and Sheline, R. K. (1962). The infrared spectrum and evidence for the structure of a new metal carbonyl. *Journal of the American Chemical Society*, 84(18):3589–3590.

[64] Stuart, J. T. (1958). On the non-linear mechanics of hydrodynamic stability. *Journal of Fluid Mechanics*, 4(1):1–21.

[65] Sun, H., Niu, Y., Li, R., Jin, S., and Gong, S. (2007). Tunneling-induced large cross-phase modulation in an asymmetric quantum well. *Opt. Lett.*, 32(17):2475–2477.

[66] Sánchez-Barquilla, M., Silva, R. E. F., and Feist, J. (2020). Cumulant expansion for the treatment of light–matter interactions in arbitrary material structures. *The Journal of Chemical Physics*, 152(3):034108.

[67] Taylor, M. A. D., Mandal, A., and Huo, P. (2022). Resolving ambiguities of

the mode truncation in cavity quantum electrodynamics. *Opt. Lett.*, 47(6):1446–1449.

[68] Triana, J. F., Arias, M., Nishida, J., Muller, E. A., Wilcken, R., Johnson, S. C., Delgado, A., Raschke, M. B., and Herrera, F. (2022). Semi-empirical quantum optics for mid-infrared molecular nanophotonics. *The Journal of Chemical Physics*, 156(12):124110.

[69] Venkatramani, R. and Mukamel, S. (2002). Correlated line broadening in multidimensional vibrational spectroscopy. *The Journal of Chemical Physics*, 117(24):11089–11101.

[70] Waks, E., Diamanti, E., Sanders, B. C., Bartlett, S. D., and Yamamoto, Y. (2004). Direct observation of nonclassical photon statistics in parametric down-conversion. *Phys. Rev. Lett.*, 92:113602.

[71] Wang, Y. and De Liberato, S. (2021). Theoretical proposals to measure resonator-induced modifications of the electronic ground state in doped quantum wells. *Phys. Rev. A*, 104:023109.

[72] Wilcken, R., Nishida, J., Triana, J. F., John-Herpin, A., Altug, H., Sharma, S., Herrera, F., and Raschke, M. B. (2023). Antenna-coupled infrared nanospectroscopy of intramolecular vibrational interaction. *Proceedings of the National Academy of Sciences*, 120(20):e2220852120.

[73] Wineland, D. J. and Itano, W. M. (1987). Laser Cooling. *Physics Today*, 40(6):34–40.

[74] Wood, T. H. (1988). Multiple quantum well (mqw) waveguide modulators. *Journal of Lightwave Technology*, 6(6):743–757.

[75] Yıldırım, H. and Tomak, M. (2006). Third-harmonic generation in a quantum well with adjustable asymmetry under an electric field. *physica status solidi (b)*, 243(15):4057–4063.

[76] Zhu, D., Chen, C., Yu, M., Shao, L., Hu, Y., Xin, C. J., Yeh, M., Ghosh, S., He, L., Reimer, C., Sinclair, N., Wong, F. N. C., Zhang, M., and Lončar, M. (2022). Spectral control of nonclassical light pulses using an integrated thin-film lithium niobate modulator. *Light: Science & Applications*, 11(1):327.

Appendix A

A1 Second order cumulant approach

The second order approximation is done by setting

$$\begin{aligned}\langle \hat{b}_n^\dagger \hat{b}_n \hat{b}_n \rangle &= |\langle \hat{b}_n \rangle|^2 \langle \hat{b}_n \rangle + \langle \hat{b}_n \rangle^* \langle \hat{b}_n \hat{b}_n \rangle_{\mathrm{c}} + \langle \hat{b}_n \rangle \langle \hat{b}_n^\dagger \hat{b}_n \rangle_{\mathrm{c}} + \langle \hat{b}_n \rangle \langle \hat{b}_n^\dagger \hat{b}_n \rangle_{\mathrm{c}} + \langle \hat{b}_n^\dagger \hat{b}_n \hat{b}_n \rangle_{\mathrm{c}}, \\ &\approx \left(|\langle \hat{b}_n \rangle|^2 + 2\langle \hat{b}_n^\dagger \hat{b}_n \rangle_{\mathrm{c}} \right) \langle \hat{b}_n \rangle + \langle \hat{b}_n \hat{b}_n \rangle_{\mathrm{c}} \langle \hat{b}_n \rangle^*, \end{aligned} \tag{A1.1}$$

where we approximate $\langle \hat{b}_n^\dagger \hat{b}_n \hat{b}_n \rangle_{\mathrm{c}} \approx 0$. The equations of motion for the quadratic terms are

$$\frac{\mathrm{d}}{\mathrm{dt}} \langle \hat{b}_n^\dagger \hat{b}_n \rangle = -\gamma_n \langle \hat{b}_n^\dagger \hat{b}_n \rangle \quad \Rightarrow \quad \langle \hat{b}_n^\dagger \hat{b}_n(t) \rangle_{\mathrm{c}} = \langle \hat{b}_n^\dagger \hat{b}_n(0) \rangle_{\mathrm{c}} e^{-\gamma_n t} \tag{A1.2}$$

$$\frac{\mathrm{d}}{\mathrm{dt}} \langle \hat{b}_n \hat{b}_n \rangle = -(\gamma_n + i2\omega_n) \langle \hat{b}_n \hat{b}_n \rangle + i2U_n (\langle \hat{b}_n^\dagger \hat{b}_n \hat{b}_n \hat{b}_n \rangle + \langle \hat{b}_n \hat{b}_n^\dagger \hat{b}_n \hat{b}_n \rangle), \tag{A1.3}$$

$$= -(\gamma_n + i2(\omega_n - U_n)) \langle \hat{b}_n \hat{b}_n \rangle + i4U_n \langle \hat{b}_n^\dagger \hat{b}_n \hat{b}_n \hat{b}_n \rangle, \tag{A1.4}$$

where we use the identity $\langle \hat{b}_n \hat{b}_n^\dagger \hat{b}_n \hat{b}_n \rangle = \langle \hat{b}_n^\dagger \hat{b}_n \hat{b}_n \hat{b}_n \rangle + \langle \hat{b}_n \hat{b}_n \rangle$. For the quartic operator in the second equation, we expand it and also neglect quartic and cubic cumulants ($\langle \hat{A}\hat{B}\hat{C}\hat{D} \rangle_{\mathrm{c}} \simeq 0$ and $\langle \hat{A}\hat{B}\hat{C} \rangle_{\mathrm{c}} \simeq 0$) to give

$$\langle \hat{b}_n^\dagger \hat{b}_n \hat{b}_n \hat{b}_n \rangle \approx |\langle \hat{b}_n \rangle|^2 \langle \hat{b}_n \rangle^2 + 3 \left(|\langle \hat{b}_n \rangle|^2 \langle \hat{b}_n \hat{b}_n \rangle_{\mathrm{c}} + \langle \hat{b}_n^\dagger \hat{b}_n \rangle_{\mathrm{c}} \langle \hat{b}_n \rangle^2 + \langle \hat{b}_n^\dagger \hat{b}_n \rangle_{\mathrm{c}} \langle \hat{b}_n \hat{b}_n \rangle_{\mathrm{c}} \right). \tag{A1.5}$$

The closed system of equations obtained is

$$\frac{\mathrm{d}}{\mathrm{dt}}\langle\hat{b}_n\rangle = -\left(\frac{\gamma_n}{2}+i\omega_n\right)\langle\hat{b}_n\rangle + i2U_n\left(\left\{|\langle\hat{b}_n\rangle|^2+2\langle\hat{b}_n^\dagger\hat{b}_n\rangle_\mathrm{c}\right\}\langle\hat{b}_n\rangle+\langle\hat{b}_n\hat{b}_n\rangle_\mathrm{c}\langle\hat{b}_n\rangle^*\right), \tag{A1.6}$$

$$\frac{\mathrm{d}}{\mathrm{dt}}\langle\hat{b}_n\hat{b}_n\rangle_\mathrm{c} = -(\gamma_n+i2(\omega_n-U_n))\langle\hat{b}_n\hat{b}_n\rangle_\mathrm{c} + i4U_n\left(|\langle\hat{b}_n\rangle|^2\langle\hat{b}_n\rangle^2+3\left\{|\langle\hat{b}_n\rangle|^2\langle\hat{b}_n\hat{b}_n\rangle_\mathrm{c}+\langle\hat{b}_n^\dagger\hat{b}_n\rangle_\mathrm{c}\langle\hat{b}_n\rangle^2+\langle\hat{b}_n^\dagger\hat{b}_n\rangle_\mathrm{c}\langle\hat{b}_n\hat{b}_n\rangle_\mathrm{c}\right\}\right). \tag{A1.7}$$

A2 Continuous wave analysis

We want to understand the photon/energy flux incoming to the cavity, in order to calibrate the mean number of excitations present in the empty and filled cavity, both in the linear and nonlinear regime.

A2.1 Mean Photon flux theory

In a work about the detection of squeezed light [9], it is derived a relationship for the mean photon flux output collected over the transverse area A of an specific cavity geometry, although the method is quite general [11].

The setup consist on a ring cavity with two nonzero transmission mirrors. The mean photon flux reads

$$\frac{2\varepsilon_0 cA}{\hbar\omega_\mathrm{c}}\langle\hat{E}_\mathrm{c}^{(-)}(z,t)\hat{E}_\mathrm{c}^{(+)}(z,t)\rangle = 2\gamma_1\langle\hat{a}^\dagger(t-z/c)\hat{a}(t-z/c)\rangle = \Phi(t-z/c), \tag{A2.1}$$

where ω_c is the cavity mode and γ_1 is the photon loss rate through the mirror 1 whose reservoir modes carry the detected field. It is derived from the following master equation

$$\frac{\mathrm{d}}{\mathrm{dt}}\hat{\rho} = \frac{1}{i\hbar}[\hat{H},\hat{\rho}] + \gamma_1(2\hat{a}\hat{\rho}\hat{a}^\dagger - \{\hat{a}^\dagger\hat{a},\hat{\rho}\}) + \mathcal{L}_2\hat{\rho} + \mathcal{L}'\hat{\rho}. \tag{A2.2}$$

$\mathcal{L}_2$ and $\mathcal{L}'$ are Lindblad terms associated with mirror 2 and intra-cavity losses. After the shape comparison, we link our cavity loss ratio parameter with the reference as $\kappa = 2\gamma_1$. This equation is useful as allows the calculation of the detected electric field intensity at the detector arrival time t by using the mean

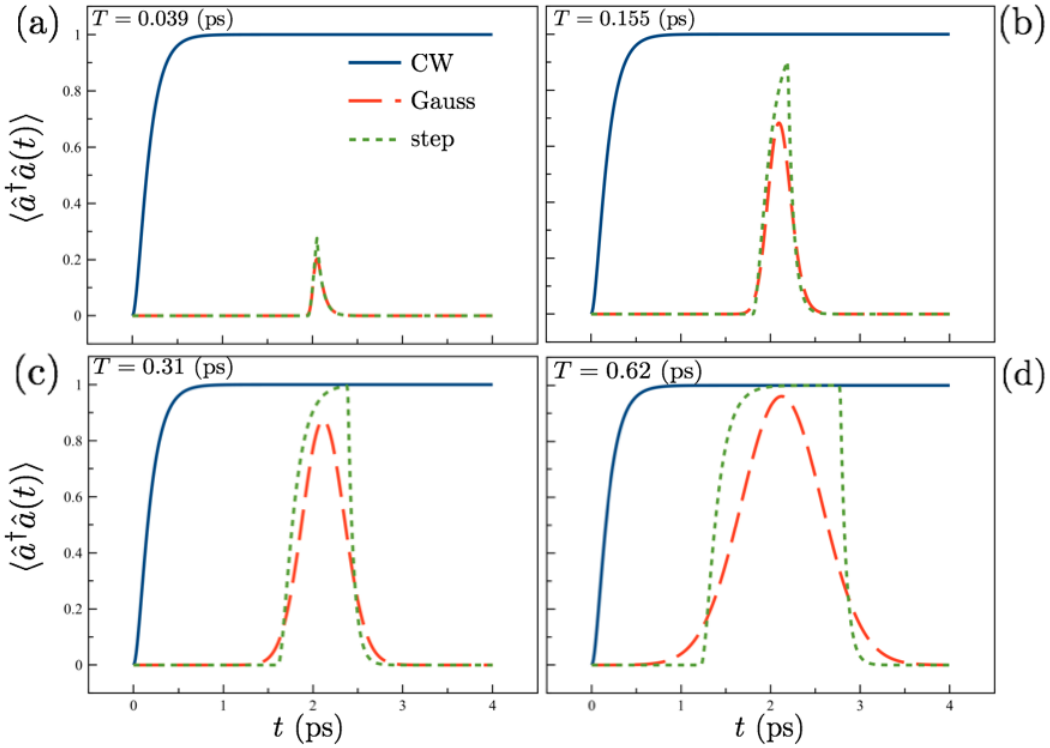

Figure A2.1: Empty cavity mean photon number comparison between a continuous driving (CW, blue lines) and two finite pulses with Gaussian (orange dashed) and an a step function envelope (green dotted) with decay rate $\kappa = 15.6$ THz, $F_0 = 0.5\kappa$ and complete resonance between the cavity mode and the carrier frequency $\omega_d = \omega_c$. The four images represent 4 different time widths T_i of the Gaussian pulses centered at $t_0 = 2.0$ ps: (a) $T = 0.039$ fs, (b) $T = 0.155$ fs, (c) $T = 0.310$ fs and (d) $T = 0.620$ fs. The time duration of the step function is fixed as $T_{\text{step}} = \sqrt{2\pi}T$ in order to have the same normalization of the Gaussian pulse with duration T.

photon number at the time when light passed through mirror 1 as reads

$$\langle \hat{E}_c^{(-)}(z,t)\hat{E}_c^{(+)}(z,t)\rangle = \frac{\hbar\omega_c\kappa}{2\varepsilon_0 cA}\langle \hat{a}^\dagger(t-z/c)\hat{a}(t-z/c)\rangle. \tag{A2.3}$$

A2.2 Steady Photon flux and Power in terms of our model parameters

We want to connect our parameters choice with a photon flux $\Phi = \kappa\langle \hat{a}^\dagger\hat{a}\rangle$ and a value for the power associated with the transmission of the MQW. The exact system of equations for the cavity mean number of excitations and coherence, taking dissipation ruled by the cavity decay rate κ, and a arbitrary but positive driving function $\varphi(t)$ with driving rate F_0 and carrier frequency equal to the cavity

single mode, are

$$\frac{\mathrm{d}}{\mathrm{dt}}\langle\hat{a}^\dagger\hat{a}\rangle - \kappa\langle\hat{a}^\dagger\hat{a}\rangle - 2F_0\varphi(t)\mathrm{Im}[\langle\hat{a}(t)\rangle e^{i\omega_c t}] \tag{A2.4}$$

$$\frac{\mathrm{d}}{\mathrm{dt}}\langle\hat{a}\rangle = -\left(\frac{\kappa}{2} + i\omega_c\right)\langle\hat{a}(t)\rangle - iF_0\varphi(t)e^{-i\omega_c t}. \tag{A2.5}$$

In this linear case, it can be proved that the cavity, apart from the rotating factor $e^{-i\omega_c t}$ coherence is completely imaginary. Moreover, the equation for the photon mean number and for coherence defined as $\tilde{a}(t) = \mathrm{Im}[\langle\hat{a}(t)\rangle e^{i\omega_c t}]$ are the same equation, and then $\langle\hat{a}^\dagger\hat{a}(t)\rangle = (a(t))^2$ [1].

For a resonant continuous wave regime (CW, equal to the condition $\varphi(t) = 1$ for $t > 0$) in our empty cavity model, the equation of motion to solve (setting $\hbar = 1$)

$$\frac{\mathrm{d}}{\mathrm{dt}}\tilde{a} = -\frac{\kappa}{2}\tilde{a} - F_0, \tag{A2.6}$$

The mean photon number changes in time by the following expression derived from this system

$$\langle\hat{a}^\dagger\hat{a}(t)\rangle = \tilde{a}(t)^2 = \frac{4F_0^2}{\kappa^2}\left(1 - e^{-\kappa t/2}\right)^2, \tag{A2.7}$$

and expresses an steady and maximum value for this mean number that reads

$$\langle\hat{a}^\dagger\hat{a}\rangle_{\mathrm{ss}} = \frac{4F_0^2}{\kappa^2}. \tag{A2.8}$$

In Figure A2.1 we show a comparison between the CW regime with $F_0/\kappa = 0.5$ ($\langle\hat{a}^\dagger\hat{a}\rangle_{\mathrm{ss}} = 1$) with calculations done using four different values of the time width of a Gaussian pulse (dashed orange lines) and Step or "square" pulses, centered at $t_0 = 2$ ps, when this widths were chosen to match the same normalization condition for these two pulse envelope shapes. In this thesis we center our attention in infrared light pulses with $T \cong 0.155$ ps, to match with the experimental results obtained in [48]. As it is clear from Figure A2.1-(b), the pulse never reach a mean photon number higher than 1.

Taking this value as reference for the photon leaking trough the open cavity framework, the photon flux associated is

$$\Phi_{\mathrm{ss}} = \kappa\langle\hat{a}^\dagger\hat{a}\rangle_{\mathrm{ss}} = \frac{4F_0^2}{\kappa}. \tag{A2.9}$$

[1] Check the equation of motion for $\tilde{a}^2(t)$ to convince yourself.

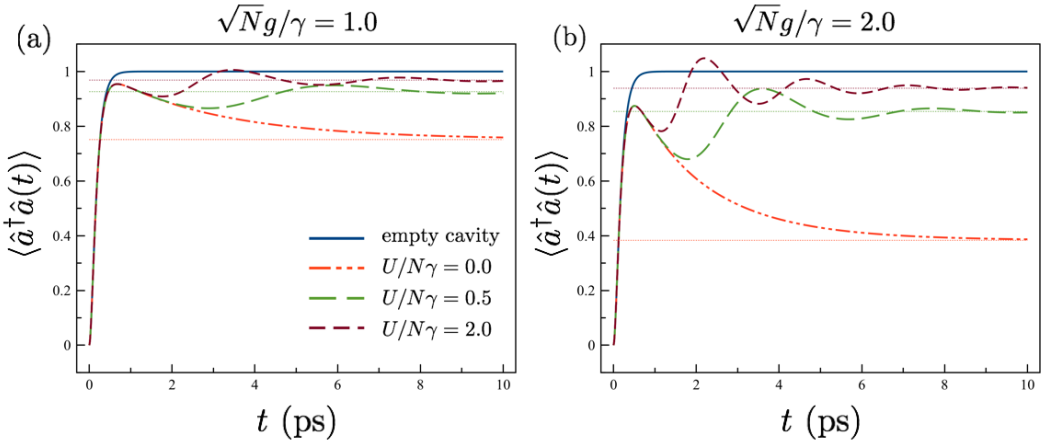

Figure A2.2: Comparison of the mean photon number in the continuous wave regime between the empty cavity (solid blue line) and the cavity filled with harmonic (orange dot–dashed lines) and anharmonic dipoles (dashed green and brown lines), for $F_0 = 0.5\kappa$, and $\{\kappa, \gamma\} = \{15.6, 0.6\}$ THz. The horizontal dashed grid–lines indicate the steady values for all curves. (a) Cavity mean photon number for $\sqrt{N}g = \gamma$ and (b) $\sqrt{N}g = 2\gamma$.

For our simulations we are mainly interested in the regime with the ratio $F_0/\kappa \sim 0.5$. Then

$$\Phi_{\text{ss}} = \frac{4(0.5\kappa)^2}{\kappa} = \kappa, \tag{A2.10}$$

which matches with our choice of the cavity bandwidth.

A2.3 CW mean photon number comparison in a filled cavity

In Figure A2.2 we compare the steady–state mean photon number when the cavity is filled with harmonic ($U/\gamma = 0$) or anharmonic ($U/\gamma > 0$) dipoles, taking as a reference the empty cavity analytical result, for which we have $\langle \hat{a}^\dagger \hat{a} \rangle_{\text{ss}} = 4F_0^2/\kappa^2 = 1$. In both coupling conditions ($\sqrt{N}g = \gamma$ and $\sqrt{N}g = 2\gamma$), it is evident that filling the cavity inevitably will low the mean number of excitations, since these will be distributed between both cavity and material oscillators. We show numerically that by increasing the anharmonic parameter, with respect to the dipole decay rate, we also increase the mean photon number $\langle \hat{a}^\dagger \hat{a} \rangle_{\text{NL}}$, remaining among the linear limits that we state as

$$\frac{4F_0^2\gamma^2}{(4Ng^2 + \kappa\gamma)^2} < \langle \hat{a}^\dagger \hat{a} \rangle_{\text{NL}} < \frac{4F_0^2}{\kappa^2}, \tag{A2.11}$$

where the lower limit is the analytical steady–state value for a driven cavity linearly coupled with a resonant harmonic oscillator with decay rate γ.

A3 Nonlinear phase in the CW regime

The equation of motion for a anharmonic dipolar coherence in the CW driving regime and the rotating frame of the cavity frequency $\omega_c = \omega_0$, after removing adiabatically the cavity equation, and defyning $\langle \tilde{B}_0^{\rm ad}(t)\rangle = \langle \hat{B}_0^{\rm ad}(t)\rangle e^{i\omega_0 t}$, is

$$\frac{\mathrm{d}}{\mathrm{dt}}\langle \tilde{B}_0^{\rm ad}(t)\rangle = -\frac{\tilde{\gamma}}{2}\langle \tilde{B}_0^{\rm ad}(t)\rangle - \frac{2\sqrt{N}g}{\kappa}F_0 + i\frac{2U}{N}|\langle \tilde{B}_0^{\rm ad}(t)\rangle|^2\langle \tilde{B}_0^{\rm ad}(t)\rangle, \tag{A3.1}$$

where $\tilde{\gamma} = \gamma(1 + 4N^2 g/(\kappa\gamma))$. Defining $R_0 = 4\sqrt{N}gF_0/(\kappa\tilde{\gamma})$ (a real and positive parameter), and going to the steady state condition $\mathrm{d}\langle \tilde{B}_0^{\rm ad}(t)\rangle/\mathrm{dt} \to 0$, we can express the steady form of the coherence $\langle \tilde{B}_0^{\rm ss}\rangle$ as reads

$$\langle \tilde{B}_0^{\rm ss}\rangle + R_0 - i\frac{4U}{N\tilde{\gamma}}|\langle \tilde{B}_0^{\rm ss}\rangle|^2\langle \tilde{B}_0^{\rm ss}\rangle = 0, \tag{A3.2}$$

$$\Rightarrow |\langle \tilde{B}_0^{\rm ss}\rangle|^6 + \left(\frac{N\tilde{\gamma}}{4U}\right)^2 |\langle \tilde{B}_0^{\rm ss}\rangle|^2 - \left(\frac{N\tilde{\gamma}R_0}{4U}\right)^2 = 0. \tag{A3.3}$$

The last line correspond to a cubic equation in terms of $|\langle \tilde{B}_0^{\rm ad}\rangle|^2$ with a single real and positive root, which is exactly the squared norm of the nonzero steady state of the dipolar coherence in the complex plane. Their real part, imaginary part and phase, defined implicitly in terms of the norm, are

$$\mathrm{Re}[\langle \tilde{B}_0^{\rm ss}\rangle] = -\frac{1}{R_0}|\langle \tilde{B}_0^{\rm ss}\rangle|^2, \tag{A3.4}$$

$$\mathrm{Im}[\langle \tilde{B}_0^{\rm ss}\rangle] = -\frac{4U}{N\tilde{\gamma}R_0}|\langle \tilde{B}_0^{\rm ss}\rangle|^4, \tag{A3.5}$$

and

$$\phi_{\rm ss,NL}^{(B_0)} = \arctan\left(\frac{4U}{N\tilde{\gamma}}|\langle \tilde{B}_0^{\rm ss}\rangle|^2\right) - \pi. \tag{A3.6}$$

The $-\pi$ in the last line states that this complex value relies in the third quadrant of the phase space.

The derivation of the correspondent nonlinear phase for the cavity $\phi_{\rm ss,NL}^{(a)}$ is

straightforward by setting the steady–state equality that reads

$$-\frac{\kappa}{2}\langle\tilde{a}_{\rm ss}\rangle - i\sqrt{N}g\langle\tilde{B}_0^{\rm ss}\rangle - iF_0 = 0.$$

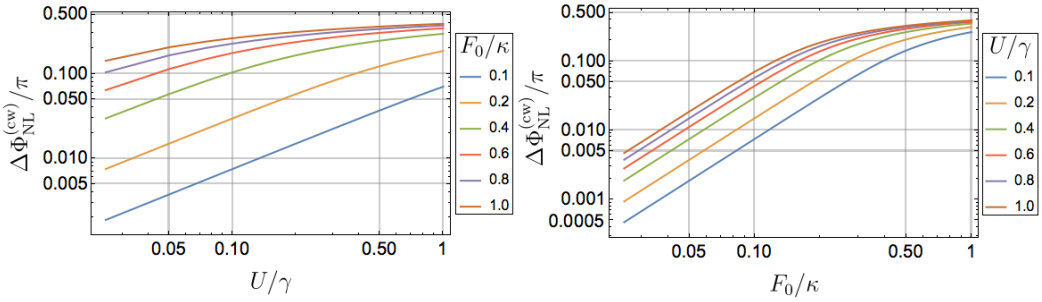

Figure A3.1: Nonlinear phase shift in the continuous wave regime. Analytical calculations for $N = 2$ quantum wells in resonance with the driving field and the cavity mode, in the adiabatic approximation. The set of parameters used are $\{\omega_0, \sqrt{2}g, \kappa, \gamma\} = \{40, 1.0, 12, 0.6\}$ THz.

In Figure A3.1 it is shown the nonlinear phase shifts obtained numerically in the CW regime $\Delta\Phi_{\rm NL}^{\rm (cw)}$, for different driving and anharmonicity conditions, evidencing a scaling crossover when $F_0/\kappa \sim 0.5$.

A4 Adiabatic elimination of the antenna dynamics

Equation A3.1 is obtained in the bad cavity limit, where we adiabatically eliminate the dynamics of the single field mode ($\mathrm{d}\langle\hat{a}(t)\rangle/\mathrm{dt} \to 0$) since $\kappa \gg \gamma$ and $(\kappa-\gamma)/4 > \sqrt{N}g$, to reduce the equations of motion to a single equation for bright collective matter coherence $\hat{B}_0$ which contains the influence of the open cavity mode.

Equation A3.1 with $F_{\rm d}(t) = 0$ is known in non-linear hydrodynamics as the Stuart-Landau oscillator equation [64, 55]. The laser pulse at a given time $t = t_{\rm off}$ turns off and Eq. (A3.1) can be solved analytically by a slow variation of the dipole coherence in polar form as $\langle\tilde{B}_0^{\rm ad}(t)\rangle = |\langle\tilde{B}_0^{\rm ad}(t)\rangle|e^{i\phi(t)}$. Thus, the equations

of motion for the amplitude and phase can be written as

$$\frac{\mathrm{d}}{\mathrm{dt}}|\langle\tilde{B}_0^{\mathrm{ad}}(t)\rangle| = -\frac{\tilde{\gamma}}{2}|\langle\tilde{B}_0^{\mathrm{ad}}(t)\rangle| \tag{A4.1}$$

$$\frac{\mathrm{d}}{\mathrm{dt}}\phi(t) = 2\frac{U}{N}|\langle\tilde{B}_0^{\mathrm{ad}}(t)\rangle|^2. \tag{A4.2}$$

where their corresponding solutions are given by

$$|\langle\tilde{B}_0^{\mathrm{ad}}(t)\rangle| = B_{\mathrm{off}}e^{-\frac{\tilde{\gamma}}{2}(t-t_{\mathrm{off}})} \tag{A4.3}$$

$$\phi(t) = \phi_{\mathrm{off}} + \frac{2UB_{\mathrm{off}}^2}{N\tilde{\gamma}}\left\{1 - e^{-\tilde{\gamma}(t-t_{\mathrm{off}})}\right\}. \tag{A4.4}$$

with $B_{\mathrm{off}} = |\langle\tilde{B}_0^{\mathrm{ad}}(t_{\mathrm{off}})\rangle|$ and $\phi_{\mathrm{off}} = \phi(t_{\mathrm{off}})$. The dipole coherence in the rotating frame of the laser evolves as

$$\langle\hat{B}_0^{\mathrm{ad}}(t)\rangle = \langle\hat{B}_0^{\mathrm{ad}}(t_{\mathrm{off}})\rangle e^{-\frac{\tilde{\gamma}}{2}(t-t_{\mathrm{off}})}e^{-i\omega_0(t-t_{\mathrm{off}})} \times \exp[i\Delta\phi_{\mathrm{ss}}(1-\exp[-\tilde{\gamma}(t-t_{\mathrm{off}})])], \tag{A4.5}$$

where $\Delta\phi_{\mathrm{ss}} = \phi_{\mathrm{ss}} - \phi_{\mathrm{off}}$ and $\langle\hat{B}_0^{\mathrm{ad}}(t_{\mathrm{off}})\rangle = B_{\mathrm{off}}e^{i\phi_{\mathrm{off}}}$. The exponential that depends on the relative phase $\Delta\phi$ in Eq. (A4.5) evidences the nonlinear contributions, instead of the solution with harmonic MQWs or in the weak driving regime. To clarify, the analogous solution of the dipole coherence with $U = 0$ $[\hat{B}_{0,\mathrm{L}}^{\mathrm{ad}}(t)]$ for $t \geq t_{\mathrm{off}}$ is given by

$$\langle\hat{B}_{0,\mathrm{L}}^{\mathrm{ad}}(t)\rangle = -\beta(T)\frac{2\sqrt{N}gF_0}{\kappa}e^{-(\tilde{\gamma}/2+i\omega_0)t} \tag{A4.6}$$

where the factor $\beta(T)$ depends on the envelope functional shape, and the stationary phase $\Delta\phi_{\mathrm{ss}} = 0$ due to the system evolves with a constant phase $\phi_{\mathrm{ss}} = \phi_{\mathrm{off}}$.

In the case of the phase, Eq. (A4.4) describes a stationary phase $\phi(t) = \phi_{\mathrm{ss}}$ in the long time regime ($t \gg t_{\mathrm{off}}$), which is given by

$$\phi_{\mathrm{ss}} = \phi_{\mathrm{off}} + \frac{2UB_{\mathrm{off}}^2}{N\tilde{\gamma}}. \tag{A4.7}$$

Note that the expression is quadratic respect to amplitude B_{off} and constant for harmonic MQWs ($U = 0$).

A4.1 Nonlinear phase shift ansatz for an arbitrary driving pulse

We introduce an ansatz for the relative phase since the amplitude $|B_{\text{off}}|$ cannot be defined for general driving pulses. We define the nonlinear phase shift $\Delta\phi_{\text{NL}}$ at frequency ω_0 as

$$\Delta\phi_{\text{NL}} = \alpha_{\text{fit}} \frac{2U}{N\tilde{\gamma}} \left(\frac{F_0}{\kappa}\right)^2, \tag{A4.8}$$

where α_{fit} is a phenomenological parameter to be explored. The definition in Eq. (A4.8) is possible considering that the squared amplitude of the dipole coherence [Eq. (A4.3)] and the stationary phase [Eq. (A4.7)] grow proportional to the square of the driving strength for the ratio $F_0/\kappa < 1$.